ISSN 2355-3286

ULTIMA Computing

Jurnal Sistem Komputer

Engineering | Vol. 17 | No. 2 | Page 1 - 57 | December 2025 | ISSN 2355-3286

UMN

UNIVERSITAS
MULTIMEDIA
NUSANTARA

ISSN 2355-3286

EDITORIAL BOARD

Editor-in-Chief
Monica Pratiwi, S.ST., M.T.

Managing Editor
M.B.Nugraha, S.T., M.T.
Nabila Husna Shabrina, S.T., M.T.
Hargyo T.N. Ignatius, Ph.D.
Fakhruddin M., S.T., M.T. (Undip)
Silmi Ath Thahirah, S.T., M.T. (UPI)
Imam Taufiqurrahman, S.Pd., M.T. (Unsil)

Designer & Layouter
Dimas Farid Arief Putra

Members
Dista Yoel Tadeus, S.T., M.T. (Undip)
Denny Darlis, S.Si., M.T. (Telkom University)
Ariana Tulus Purnomo, Ph.D. (NTUST)
Nurul Fahmi Arief Hakim, S.Pd., M.T. (UPI)
Dede Furqon N., S.T., M.T. (Unjani)
Iqbal Ahmad Dahlan, S.T., M.T. (Unhan)
Moeljono Widjaja, Ph.D. (UMN)
Dareen Halim, S.T., M.Sc. (UMN)
Ahmad Syahril Muharom, S.Pd., M.T. (UMN)
Samuel Hutagalung, M.T.I (UMN)

EDITORIAL ADDRESS

Universitas Multimedia Nusantara (UMN)
Jl. Scientia Boulevard
Gading Serpong
Tangerang, Banten - 15811
Indonesia
Phone. (021) 5422 0808
Fax. (021) 5422 0800
Email : ultimacomputing@umn.ac.id

Ultima Computing : Jurnal Sistem Komputer is a Journal of Computer Engineering Study Program, Universitas Multimedia Nusantara which presents scientific research articles in the field of Computer Engineering and Electrical Engineering as well as current theoretical and practical issues, including Edge Computing, Internet-of-Things, Embedded Systems, Robotics, Control System, Network and Communication, System Integration, as well as other topics in the field of Computer Engineering and Electrical Engineering. The Ultima Computing : Jurnal Sistem Komputer is published regularly twice a year (June and December) and is jointly managed by the Computer Engineering and Electrical Engineering Study Program at Universitas Multimedia Nusantara.

Call for Papers

International Journal of New Media Technology (IJNMT) is a scholarly open access, peer-reviewed, and interdisciplinary journal focusing on theories, methods and implementations of new media technology. Topics include, but not limited to digital technology for creative industry, infrastructure technology, computing communication and networking, signal and image processing, intelligent system, control and embedded system, mobile and web based system, and robotics. IJNMT is published twice a year by Faculty of Engineering and Informatics of Universitas Multimedia Nusantara in cooperation with UMN Press.

Ultimatics : Jurnal Teknik Informatika is the Journal of the Informatics Study Program at Universitas Multimedia Nusantara which presents scientific research articles in the fields of Analysis and Design of Algorithm, Software Engineering, System and Network security, as well as the latest theoretical and practical issues, including Ubiquitous and Mobile Computing, Artificial Intelligence and Machine Learning, Algorithm Theory, World Wide Web, Cryptography, as well as other topics in the field of Informatics.

Ultima Computing : Jurnal Sistem Komputer is a Journal of Computer Engineering Study Program, Universitas Multimedia Nusantara which presents scientific research articles in the field of Computer Engineering and Electrical Engineering as well as current theoretical and practical issues, including Edge Computing, Internet-of-Things, Embedded Systems, Robotics, Control System, Network and Communication, System Integration, as well as other topics in the field of Computer Engineering and Electrical Engineering.

Ultima InfoSys : Jurnal Ilmu Sistem Informasi is a Journal of Information Systems Study Program at Universitas Multimedia Nusantara which presents scientific research articles in the field of Information Systems, as well as the latest theoretical and practical issues, including database systems, management information systems, system analysis and development, system project management information, programming, mobile information system, and other topics related to Information Systems.

ISSN 2355-3286

FOREWORD

ULTIMA Greetings!

Ultima Computing : Jurnal Sistem Komputer is a Journal of Computer Engineering and Electrical Engineering at Multimedia Nusantara University which presents scientific research articles in the field of Computer Systems as well as the latest theoretical and practical issues, including Edge Computing, Internet-of-Things, Embedded Systems, Robotics, Control Systems, Network and Communication, System Integration, and other topics in the field of Computer Engineering and Electrical Engineering.

In this December 2025 edition, Ultima Computing enters the 2nd Edition of Volume 17. In this edition there are seven scientific papers from researchers, academics and practitioners in the fields of Computer Engineering and Electrical Engineering. Some of the topics raised in this journal are: Unlocking Wellness: Pioneering IoT Wearable Sensor with The Smart Ring for Body Fatigue Monitoring, Six-Axis Force-Torque Analysis of a Flexible-Tube Wrist for Misaligned Ports in Robotic EV Charging, IoT-Based Fire Detection System Using a Flame Detector and Arduino Uno R4 Wi-Fi, Convolutional Neural Network Roasted Coffee Bean Classification Based on Color, Implementation of Trajectory Tracking on Mobile Robot Differential Drive, Development of a Microcontroller-Based Dynamic Lighting System with Automated Dimming and Color Adjustment, and Predictive Control of Speed, Steering, and Braking for An Autonomous Car on Uphill and Downhill Road.

On this occasion we would also like to invite the participation of our dear readers, researchers, academics, and practitioners, in the field of Engineering and Informatics, to submit quality scientific papers to: International Journal of New Media Technology (IJNMT), Ultimatics : Jurnal Teknik Informatics, Ultima Infosys: Journal of Information Systems and Ultima Computing: Journal of Computer Systems. Information regarding writing guidelines and templates, as well as other related information can be obtained through the email address ultimacomputing@umn.ac.id and the web page of our Journal here.

Finally, we would like to thank all contributors to this December 2025 Edition of Ultima Computing. We hope that scientific articles from research in this journal can be useful and contribute to the development of research and science in Indonesia.

December 2025,

Monica Pratiwi, S.ST., M.T.
Editor-in-Chief

ISSN 2355-3286

TABLE OF CONTENT

ISSN 2355-3286

Unlocking Wellness: Pioneering IoT Wearable Sensor with The Smart Ring for Body Fatigue Monitoring

Dewi Indriati Hadi Putri[1], Elysa Nensy Irawan[2], Liptia Venica[3], Hafiyyan Putra Pratama[4]
[1,2,3] Department of Mechatronics and Artificial Intelligence, Universitas Pendidikan Indonesia, Bandung, Indonesia
[1]dewiindri@upi.edu , [2]elysanensy@upi.edu , [3]liptiavenica@upi.edu
[4]Department of Telecommunication System, Universitas Pendidikan Indonesia, Bandung, Indonesia
[4]hafiyyan@upi.edu

Accepted on May 20, 2025
Approved on December 12, 2025

***Abstract*— This study present the development and implementation of an IoT-Based wearable device, namely a Smart Ring, designed to monitor body fatigue levels in real time. Physical fatigue caused by prolonged or intense activities has been reported as a contributing factor to serious health conditions such as cardiovascular disorders, asthma, and stroke. Existing wearable devices, including smartwatches and commercial smart rings, mainly provide raw physiological information without fatigue classification or early warning mechanisms. The proposed Smart Ring integrates a MAX30100 sensor to measure heart rate, blood oxygen saturation (SpO_2), and body temperature. A fuzzy logic algorithm is employed to classify fatigue levels into rest, normal, and risk categories. The system is connected to an Android application via IoT, enabling real-time monitoring, alerts, and GPS-based location reporting. Quantitative validation was conducted by comparing Smart Ring measurements with standard medical devices. The results show average deviations of ±5 bpm for heart rate, ±1.5% for SpO_2, and ±1.3 °C for body temperature, which fall within acceptable limits for non-invasive wearable monitoring. These findings demonstrate that the Smart Ring provides reliable fatigue detection while offering an affordable and practical solution for personal health monitoring in the Society 5.0 era.**

Index Terms*—, *IoT, wearable sensor, smart ring, body fatigue monitoring, fuzzy logic

I. INTRODUCTION

Fatigue can occur in anyone as a result of energy-draining physical activities. Several studies have indicated that fatigue can trigger more serious illnesses such as heart attacks, strokes, arthritis, asthma, and others [1][2][3]. Heart attacks can be induced by stress, intense physical activity, or cold weather, all of which can cause blood vessels to contract or spasm. When blood vessels contract, the amount of blood entering the heart muscle can decrease, leading to a heart attack [4][5][6].

Research conducted by A. C. Perez-Moreno et al. (2014) found that 59% of 540 patients with heart failure experienced severe fatigue before the onset of a heart attack [7]. Based on this information, it is crucial for us, especially those with a history of serious illnesses, to monitor our fatigue levels during activities to minimize the risk of sudden attacks from dangerous conditions. Research on the classification of fatigue levels for both healthy individuals and those with diabetes has been conducted by L. Aljihmani et al. (2020) using wearable sensors and machine learning methods, achieving an accuracy of 96.1% [8]. There is currently various commercial smart ring product such as Oura Ring, GO2SLEEP Ring, and Motiv Ring, which are capable of monitoring heart rate, oxygen saturation, and sleep quality [9][10][11]. However, most of these devices do not integrate parameters such as body temperature and fatigue category analysis in one affordable and easy-to-use platform. In addition, clinical validation of body fatigue data based on physiological parameters is still very limited. Therefore, the development of this smart ring is aimed at addressing these limitations, especially on the aspect of parameter integration and the potential development of an IoT-based tool that can be used for early monitoring of fatigue risks that impact cardiovascular health.

Research on wearable sensor devices has been conducted by Niswar et al. (2019), who designed a system with two biomedical sensors: an airflow thermal sensor and a pulse oximeter sensor to measure patients' vital signs [12]. However, this research is not portable for daily use because one of the measured parameters is respiration, which requires the device to be attached to the nose.

In the era of Society 5.0, the development of the Internet of Things (IoT) is in full swing. One of the most popular IoT products is the smartwatch, which is highly favored by the public due to its minimalist design and advanced features for measuring vital signs such as heart rate, SpO2, and body temperature. However, the features provided by smartwatches only offer information about vital signs and do not help in minimizing the risk of fatigue.

In this research, a Smart Ring is introduced to address the shortcomings of smartwatches. The Smart Ring is capable of providing reminders when the user reaches the fatigue threshold during activities. Unlike existing wearable devices such as smartwatches and commercial smart rings that primarily provide raw physiological data, the proposed Smart Ring integrates multi-parameter sensing (heart rate, SpO_2, and body temperature) with fuzzy logic-based fatigue classification and real-time IoT notification. Furthermore, this study provides initial quantitative validation against medical reference devices, which is still limited in most commercial smart ring implementations. This combination of fatigue inference, affordability, and IoT-based alert functionality constitutes the main novelty of this research.

Additionally, as an IoT implementation, the Smart Ring comes with an Android application called the Smart Ring App. This app is connected to GPS. The Smart Ring is designed to be economical, making it accessible to people from various walks of life. By introducing the Smart Ring as an affordable healthcare device, it is hoped that the well-being of society in the era of Society 5.0 can be achieved, particularly in the field of health. The main problem to be solved in this research is how to design and develop a smart ring-based wearable device capable of monitoring physiological indicators of body fatigue in real-time, as well as how to conduct initial validation of the accuracy of its readings compared to standard medical devices.

II. Materials & Method

A. *Wearable Sensor for Fatigue Monitoring*

Based on their placement, sensors are classified into two types: wearable sensors and implantable sensors [13]. Wearable sensors are one of the rapidly developing technologies due to the significant benefits they offer, such as easy operation, quick response, portability, and small size, which make them highly desirable [14]. Wearable sensors are types of sensors that can be integrated into wearable objects or directly onto the body. They are generally used to help monitor or provide relevant information related to clinical conditions or overall health [15].

There are various types of wearable sensors commonly used to monitor the heart and blood vessels. These sensors can measure a range of physiological parameters, such as heart rate and blood oxygen levels. As shown in Table I, Multivariable (AMON), Photoplethysmography (PPG), and Electrocardiograph (ECG) sensors, when worn on the finger (ring sensor), can measure the most comprehensive set of physiological parameters, including blood pressure, blood oxygen saturation, body temperature, and heart rate rhythm [16], [17].

TABLE I. Types of Wearable Sensor

Location of Use	Types of Sensors	Marker
Wrist	Ultrasound	Blood Pressure
• **Wrist** • **Finger (ring sensor)**	Multivariable (AMON)	Blood Pressure Blood Oxygen Saturation Body Temperature Heart Rate Rhythm
	• Photoplethysmography (PPG) • Electrocardiography (ECG)	
	• Optical	Heart Rate
	• Radio-frequency Identification	Heart Rate and Body Temperature
Arm or Thigh	Microwave Reflectometric Cardiopulmonary	Heart Rate Variability as a Method for Evaluating Stress
Phone adapter	Single-channel ECG	Heart Rate
Seatbelt in a Car	Wire type Strain Gauge	Heart Rate and Respiration Rate

The Advanced Medical Monitor (AMON) is a device used to monitor patients with heart disease and respiratory disorders. It is worn on the patient's wrist and features an accelerometer that continuously measures the user's physical activity. AMON integrates various sensors to measure SpO2, blood pressure, body movement, body temperature, and pulse rate. Fig. 1 illustrates the AMON prototype and its role in physiological monitoring systems. The AMON device integrates multiple sensors, including SpO_2, body temperature, and heart rate, and has been widely referenced as an early model of wearable medical monitoring for high-risk patients [18].

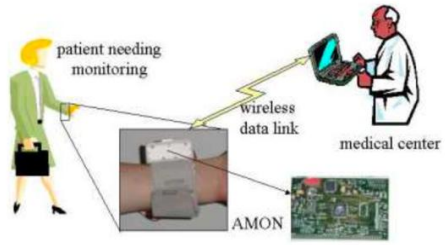

Fig. 1. *AMON* Prototype and Its Role in Monitoring Systems

The development of physiological monitoring systems continues to advance, aiming to produce simpler, more user-friendly, and cost-effective systems. One such development involves leveraging Photoplethysmography (PPG) sensors due to their ease of use and minimal impact on user mobility. PPG sensors are widely used in wearable technology because they can measure changes in blood vessel volume and estimate health metrics such as heart rate, respiration rate, blood pressure, body temperature, and blood oxygen saturation [19]. PPG sensors operate in either transmission or reflectance mode, as illustrated in Fig.2. In transmission mode, LED light is detected by a photodiode or photodetector positioned on the opposite side. In reflectance mode, the photodiode detects light reflected back from tissues, bones, and/or blood vessels

[20]. Transmission mode is commonly used in hospital settings, whereas reflectance mode is prevalent in wearable devices like smartwatches.

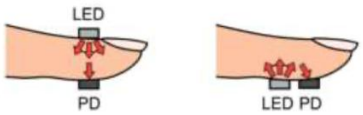

Fig. 2. Placement of LED and Photodetector in PPG Sensors: Transmission and Reflectance Modes[20]

By adapting the AMON prototype and utilizing a PPG sensor, a smart ring prototype has been designed. The PPG sensor used in this study is the MAX30100.

B. Fuzzy Logic for Classification of Fatigue Levels

Fuzzy logic was first introduced in 1965 by Lotfi A. Zadeh from the University of California through his publication titled "Fuzzy Sets." Boolean logic, which consists of binary membership values of 0 or 1, was deemed inadequate to represent human logic or thinking. Fuzzy logic was developed as an alternative to Boolean logic by allowing membership values to range between 0 and 1 [20]. In fuzzy logic, values between true/false, yes/no, high/low, far/near, and other similar dichotomies can be defined. These values can then be processed by computers to apply a form of reasoning in programming that more closely resembles human thought [21]. Generally, fuzzy logic is used to design intelligent systems capable of handling processes of human reasoning [22] [23]. It can also be utilized to determine the relationship between vital signs and physiological indicators, as shown in Table II.

TABLE II. RELATIONSHIP BETWEEN VITAL SIGNS AND PHYSIOLOGICAL INDICATORS. H=HIGH, L=LOW, N/A = NOT APPLICABLE, N=NORMAL[13]

Physiological Conditions	Heart Rate	Blood Pressure	Blood Oxygen Saturation	Body Temperature
Bradycardia	L	N/a	N/a	N/a
Tachycardia	H	N/a	N or l	N/a
Hypotension	N/a	L	N/a	N/a
Hypertension	N/a	H	N/a	N/a
Hypoxemia	N/a	N/a	Often l	N/a
Fever	H or n	N/a	N/a	H
Hypothermia	L	N or l	N/a	L
Normal Range	60-90 bpm	100-140/60-80 mm/hg	94-99%	36.5-37.5^{0}C

In Table II, the notation “N/a” (not applicable) indicates that the corresponding physiological parameter does not have a direct or clinically significant correlation with the specific condition. For example, blood oxygen saturation is not a defining marker for hypertension, hence it is marked as N/a.

The fuzzy logic model can be employed to interpret various physiological parameters by using information from collected vital signs, such as heart rate, blood pressure, blood oxygen saturation, and body temperature. An example of this implementation is illustrated in Table 2, demonstrating how vital signs can be mapped to detect a physiological condition using fuzzy logic [13]. his model can similarly be applied to detect fatigue in individuals based on specific fatigue parameters. Based on these vital signs, the fuzzy rules for this study can be categorized as shown in Table III.

TABLE III. FUZZY RULES

Input	Age (years)	Young	1-30
		Middle	20-60
		Old	50-100
	Body Temperature (^{0}C)	Low	0-36.5
		Normal	35-39
		High	37.5-50
	Heart Rate (bpm)	Slow	0-70
		Normal	60-90
		Fast	80-200
	Oxygen (%)	Low	0-92
		Normal	90-98
		High	96-100
Output	Category	Rest	0-50
		Normal	25-75
		Risk of Fatigue	50-100

Based on the fuzzy rules, the output from the system will help users determine the threshold for bodily fatigue. When this threshold is reached, a reminder will be triggered along with a slight vibration from the ring. In the event of a significant drop in condition or if the user faints, the system will automatically send an alert message to the emergency contact number listed in the Smart Ring App.

C. System Design

The Smart Ring is physically designed to be as minimalistic as possible to avoid interfering with the user during activities and resembles a typical ring worn on the finger. The Smart Ring consists of three main components: the electronic hardware, the software, and the communication system using IoT. The system designed for the Smart Ring prototype is illustrated in Fig.3.

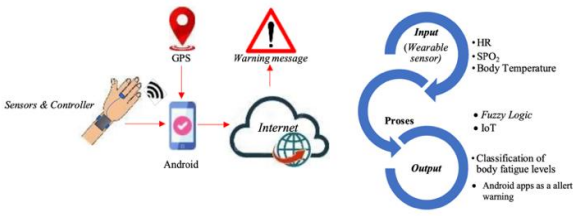

Fig. 3. Architecture Smart Ring

Data can be processed through the IoT-based monitoring system application. As shown in Fig.3, sensor data is collected by the Android software paired with the Smart Ring. The Android device can transmit data and GPS information over the internet to a server with a database [24]. If the data indicates fatigue, as recognized by the fuzzy algorithm, the Android application will trigger an alert to notify the user. Fig. 4 shows the operational flow of the Smart Ring system, starting from data acquisition, fuzzy logic-based

fatigue classification, and ending with alert generation and IoT-based data transmission.

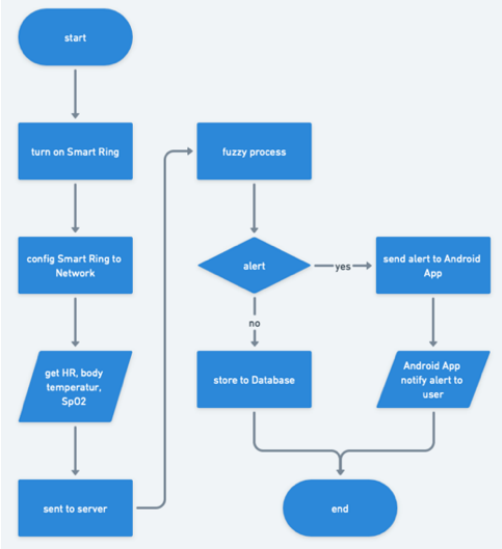

Fig. 4. Flowchart for The Smart Ring System

In this study, the Android application is designed to display fatigue data generated by the MAX30100 sensor, provide user location information to facilitate identification, and issue notifications about fatigue risk conditions. The application is developed using the Blynk server, which is connected to the NodeMCU controller.

III. Result and Analysis

This section will describe the results of the hardware design, including the smart ring box design and wiring diagram, the implementation of fuzzy logic, and the integration of sensor data with the Android application (Blynk).

A. Hardware Implementation

The smart ring prototype has a control box part which consists of several components, namely the Max30100 sensor to obtain heart rate (HR), SPO2 oxygen saturation, body temperature (0C), Oled as a display, NodeMCU as a microcontroller and battery as shown in Fig. 5.

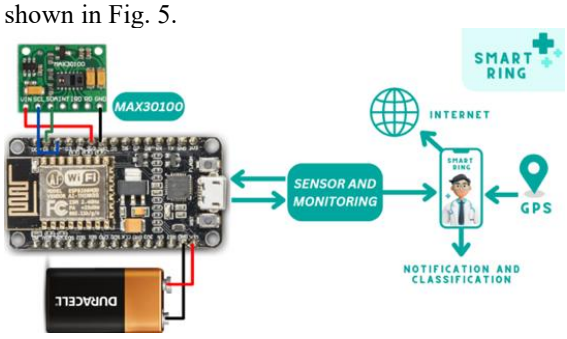

Fig. 5. Wiring Diagram of Smart Ring Prototype

Fig. 6 presents the mechanical design and physical realization of the Smart Ring prototype. Fig. 6(a) shows the three-dimensional CAD model developed using SolidWorks, which was designed to achieve a compact and ergonomic form suitable for finger placement. Fig. 6(b) illustrates the fabricated physical prototype, demonstrating the integration of electronic components within the ring structure.

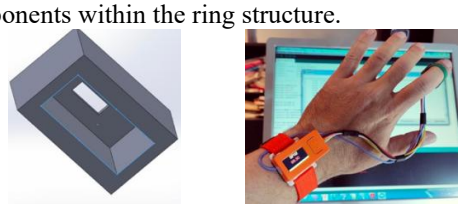

(a) (b)

Fig. 6. Smart Ring Prototype Design (a) 3D CAD Model Using SolidWork, (b) Physical Prototype of the Smart Ring

The choice of the finger as the sensor location, as shown in Figure 6(b), is based on its effectiveness in providing reliable physiological measurements. The capillaries at the fingertip provide a direct pathway for photoplethysmography, a common method used in wearable sensors to detect changes in blood volume. This technique is crucial for accurately determining heart rate (HR) and blood oxygen saturation (SpO2) [24].

B. Fuzzy Logic Implementation

In the process of fuzzification, several aspects need to be considered, such as fuzzy rules and fuzzy sets. Fuzzy rules serve as a reference for classifying the level of bodily fatigue, as outlined in Table III. The results of fuzzification are used as fuzzy inference to apply the final output rules for determining the level of fatigue [25]. The fuzzification process was developed using Python programming, resulting in membership functions for each input, as shown in Fig.7

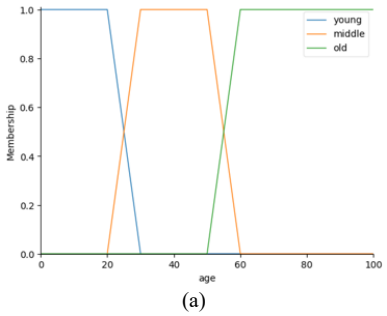

(a)

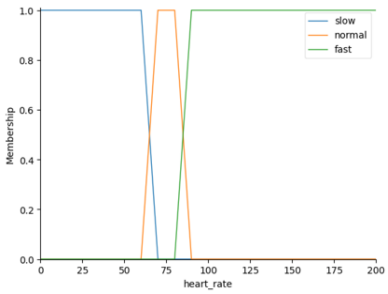

(b)

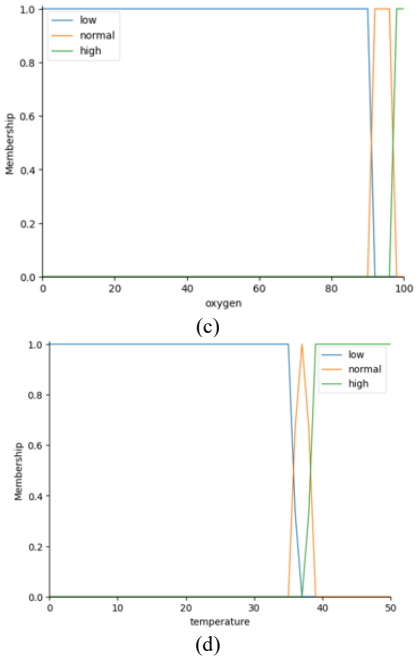

Fig. 7. Input Membership Functions for Fuzzy Logic-Based Fatigue Classification (a) Age, (b) Heart Rate, (c) Blood Oxygen Saturation (SpO_2), and (d) Body Temperature

Fig. 7 illustrates the input membership functions used in the fuzzy logic system for body fatigue classification. Fig. 7(a) represents the age membership function, which categorizes users into young, middle-aged, and old groups. Fig. 7(b) shows the heart rate membership function, dividing heart rate values into slow, normal, and fast categories. Fig. 7(c) depicts the blood oxygen saturation (SpO_2) membership function, classifying oxygen levels into low, normal, and high. Fig. 7(d) presents the body temperature membership function, which separates temperature values into low, normal, and high ranges. Each membership function plays a distinct role in modeling physiological variations related to fatigue. The membership function output consists of three conditions used to classify the level of bodily fatigue, as depicted in Fig.8

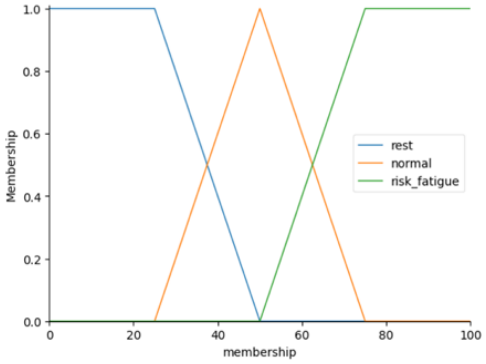

Fig. 8. Output Membership Function for Body Fatigue Classification

Fig. 8 illustrates the output membership function used in the fuzzy logic system to classify body fatigue levels. The output variable represents the overall fatigue condition and is divided into three linguistic categories: rest, normal, and risk. Each category corresponds to a specific range of output values that indicate the user's physical condition based on the combined influence of heart rate, blood oxygen saturation (SpO_2), body temperature, and age. The defuzzification process converts the fuzzy output into a crisp value, which is then used to determine the final fatigue category and trigger alerts when the risk threshold is exceeded.

C. *Smart Ring Application*

In previous research, android-based smart ring applications have been created and developed using the flutter framework with the Dart programming language. In the smart ring application, there is an interface that consists of several variable displays that show information to users such as the latest update time of the monitoring and evaluation process, user location, body fatigue level category, and start & stop buttons that function to manage monitoring and evaluation of data generated by the MAX30100 sensor. When the user starts the body condition monitoring process, there is an option by pressing the start or stop button which means whether they want to monitor and evaluate the results through the smart ring application on the smartphone, otherwise the data generated by the MAX30100 sensor is only stored in the database and not displayed in the application [24].

The smart ring application also displays 3 fatigue indicator data on the widget, namely temperature, SpO2 level, and heart rate. The value is not constant and continues to change along with the process of monitoring the user's body condition while using the smart ring [26]. The user interface of the smart ring application can be seen in Fig. 9.

Fig. 9. User Interface Smart Ring Application[24]

The smart ring application can also generate real-time notifications when the user's status evaluation is in the fatigue risk category and provide summary information of body condition data measurements as shown in Fig. 10.

Fig. 10. Alert Page When A User is at Risk of Fatigue[24]

D. *Quantitative Evaluation and Data Analysis*

In this study, a trial was conducted with a total of two users who belonged to the young age category, namely 25 years and middle age 35 years by wearing a smart ring prototype on their fingers and activating GPS and smart ring applications. Users are asked to use the smart ring before bed rest, during daily activities and are also asked to do sports movements, namely middle-distance running. Based on the test results, it can be seen that fuzzy logic has been successfully applied to classify the category of body fatigue level conditions based on the data obtained by the smart ring prototype. Which then the classification results are sent to the smart ring application.

TABLE IV. BODY FATIGUE CLASSIFICATION RESULT FOR A 25-YEAR-OLD SUBJECT

Age (years)	SpO2 (%)	Heart Rate (bpm)	Temperature (^{0}C)	Fatigue Category
25	96	67.65	36.00	rest
25	96	76.00	36.31	rest
25	96	71.95	37.00	rest
25	96	70.75	36.63	rest
25	96	28.55	35.88	rest
25	96	98.56	36.81	normal
25	97	100.31	37.10	normal
25	97	100.32	37.10	normal
25	97	100.65	37.21	normal
25	97	100.65	37.19	normal
25	95	146.1	37.55	risk
25	95	146.12	37.55	risk

Table IV presents the fatigue classification results obtained from a 25-year-old subject during different activity conditions. The classification shows a clear transition from rest to normal and risk categories as heart rate and body temperature increase, accompanied by a decrease in SpO_2.

TABLE V. BODY FATIGUE CLASSIFICATION RESULT FOR A 35-YEAR-OLD SUBJECT

Age (years)	SpO2 (%)	Heart Rate (bpm)	Temperature (^{0}C)	Category
35	96	70	36.00	rest
35	96	71	36.31	rest
35	96	71	37.00	rest
35	96	70	36.63	rest
35	96	72	35.88	rest
35	96	101	36.81	normal
35	97	98	37.10	normal
35	97	99	37.10	normal
35	97	98	37.21	normal
35	97	100	37.19	normal
35	95	147	37.55	risk
35	95	146	37.55	risk

Table V presents the body fatigue classification results for a 35-year-old subject under various activity conditions. Similar to the younger age group, the results indicate a progressive transition from the rest to normal and risk categories as physiological stress increases. The rest condition is characterized by a stable heart rate of approximately 70 bpm, SpO_2 levels around 96%, and body temperature below 3. These findings suggest that the selected physiological parameters provide consistent fatigue indicators regardless of minor age differences within the adult population.

The study reveals that at both ages 25 and 35, the pattern of body fatigue categories remains relatively consistent. The "risk" condition is characterized by a decrease in blood oxygen saturation (SpO2), a significant increase in heart rate, and a rise in body temperature. Threshold values that indicate the transition from "rest" to "normal" and subsequently to "risk" categories can serve as reliable indicators of physical fatigue. These thresholds are useful for monitoring physical activity and can be applied in occupational health settings to help prevent overexertion and ensure well-being. The interpretation of the three visualization graphs of body fatigue data based on age, body temperature, heart rate, and SpO2 can be seen in Fig.11.

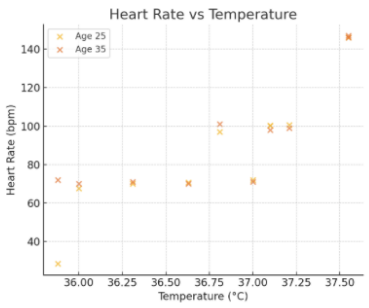

(a)

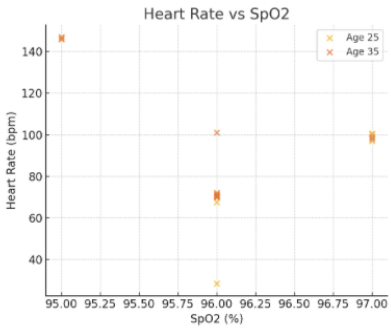

(b)

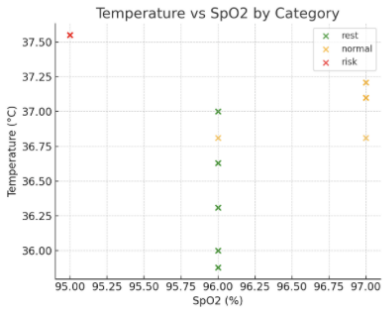

(c)

Fig. 11. Visualization of Body Fatigue Indicators (a) Heart Rate Trend, (b) Blood Oxygen Saturation (SpO_2), (c) Body Temperature Response during Physical Activity

Based on the data visualization and analysis at Fig.11, it is evident that body fatigue can be effectively assessed using three physiological parameters: heart rate, body temperature, and blood oxygen saturation (SpO2). The data shows a consistent pattern where increased body temperature and decreased SpO2 levels correlate with elevated heart rates, which serve as indicators of body stress or fatigue. In particular, when the body temperature rises to around 37.5°C and SpO2 drops to 95%, heart rates exceed 145 bpm—placing the condition into the "risk" category. Meanwhile, individuals in the "rest" category tend to maintain a body temperature below 37°C, SpO2 at 96%, and a heart rate around 70 bpm.

Across both age groups (25 and 35 years old), the trends remain consistent, suggesting that these physiological markers are reliable regardless of minor age differences within adult populations. This supports the idea that fatigue detection models can be generalized for young adults. In summary, heart rate, body temperature, and SpO2 are key indicators that can be used together to monitor physical fatigue, identify health risks, and potentially guide preventive actions or rest recommendations.

As an initial validation, the result of body temperature and heart rate measurements from the smart ring were compared with manual measurements using a digital thermometer and medical pulse oximeter [27]. Results showed an average deviation of ± 1.3^{0}C for temperature and ± 5 bpm for heart rate, which is within the tolerance of non-invasive monitoring.

E. Comparison with Medical Reference Device

To evaluate the accuracy of the proposed Smart Ring, a comparative analysis was conducted using certified medical reference devices. Heart rate and blood oxygen saturation (SpO_2) measurements obtained from the Smart Ring were compared with a fingertip medical pulse oximeter, while body temperature readings were compared with a digital medical thermometer. These reference devices are commonly used in clinical and home healthcare settings and serve as standard non-invasive measurement tools. [28] [29]

TABLE VI. COMPARISON BETWEEN SMART RING AND MEDICAL REFERENCE DEVICE

Parameter	Smart Ring (Mean)	Medical Device (Mean)	Mean Absolute Error
Heart Rate (bpm)	98.4	101.9	± 5.0 bpm
SpO_2 (%)	96.2	97.7	± 1.5 %
Body Temperature (^{0}C)	36.9	38.2	± 1.3 (^{0}C)

Based on Table.VI the comparison results indicate that the Smart Ring demonstrates measurement performance comparable to certified medical reference devices. The observed mean absolute error of ±5 bpm for heart rate and ±1.5% for SpO_2 aligns with acceptable tolerances reported for non-invasive wearable sensors. According to ISO 80601-2-61, pulse oximetry devices are considered acceptable when SpO_2 error remains within ±2%. Similarly, the observed temperature deviation of ±1.3 °C falls within the range reported for wearable temperature monitoring systems. These findings suggest that the Smart Ring provides reliable physiological measurements suitable for fatigue monitoring applications, although it is not intended to replace clinical diagnostic equipment.

IV. CONCLUSION

This study has successfully developed an IoT-based Smart Ring for real-time body fatigue monitoring using heart rate, blood oxygen saturation (SpO_2), and body temperature parameters. Quantitative evaluation results show that the Smart Ring achieves an average measurement deviation of ±5 bpm for heart rate, ±1.5% for SpO_2, and ±1.3 °C for body temperature when compared with standard medical devices. These error values fall within acceptable limits for non-invasive wearable monitoring systems. Experimental results from two adult subjects aged 25 and 35 years demonstrate consistent fatigue classification patterns. The fatigue risk condition is quantitatively characterized by heart rate values exceeding 145 bpm, body temperature above 37.5 °C, and a decrease in SpO_2 to approximately 95%. These

thresholds confirm the effectiveness of the fuzzy logic-based classification model in identifying fatigue levels across different adult age groups. Overall, the proposed Smart Ring provides a reliable and affordable solution for early fatigue detection and real-time health monitoring. Future work will involve larger-scale user testing and clinical validation to further improve measurement accuracy and generalizability. Although the Smart Ring demonstrates comparable accuracy to non-invasive medical reference devices, it is intended for fatigue monitoring and early warning purposes rather than clinical diagnosis.

ACKNOWLEDGMENT

The authors would like to thank the Department of Mechatronics and Artificial Intelligence at Universitas Pendidikan Indonesia for providing facilities and support for this research.

REFERENCES

[1] D. van Hoogmoed *et al.*, "Physical and psychosocial correlates of severe fatigue in rheumatoid arthritis," *Rheumatology*, 2010, doi: 10.1093/rheumatology/keq043.

[2] Brent A. Williams, Brent A. Williams, Brent A. Williams, and Brent A. Williams, "Abstract MP035: The Clinical Epidemiology of Fatigue in Newly Diagnosed Heart Failure," *Circulation*, 2017, doi: 10.1186/s12872-017-0555-9.

[3] Maarten Van Herck *et al.*, "Fatigue is Highly Prevalent in Patients with Asthma and Contributes to the Burden of Disease," *J. Clin. Med.*, 2018, doi: 10.3390/jcm7120471.

[4] E. Sivari and S. Surucu, "Prediction of heart attack risk using linear discriminant analysis methods," 2023, doi: 10.51271/jceees-0002.

[5] I. L. A. G. S. Yadav, S. Wakode, and S. Khasimbi, "The role of stress in the development of cardiovascular diseases," *J. Nurs. Healthc.*, 2023, doi: 10.33140/jnh.08.01.01.

[6] J. Jalaludin, "Editorial: Stress Can Lead to Cardiovascular Disease," 2023, doi: 10.55958/jcvd.v18i4.132.

[7] Ana Cristina Perez Moreno *et al.*, "Fatigue as a predictor of outcome in patients with heart failure: analysis of CORONA (Controlled Rosuvastatin Multinational Trial in Heart Failure).," *Jacc-Heart Fail.*, 2014, doi: 10.1016/j.jchf.2014.01.001.

[8] L. Aljihmani *et al.*, "Classification of Fatigue Phases in Healthy and Diabetic Adults Using Wearable Sensor," *Sensors*, 2020, doi: 10.3390/s20236897.

[9] Oura Health Ltd, "Oura Ring: Smart Ring for Sleep, Readiness & Activity Tracking." Oura Health Ltd, 2022. [Online]. Available: https://ouraring.com

[10] GO2SLEEP, "GO2SLEEP Smart Ring for Sleep Monitoring. Sleepon." 2021. [Online]. Available: https://sleepon.us

[11] Motiv Inc, "Motiv Ring: Fitness, Sleep, and Heart Rate Tracker." 2019. [Online]. Available: https://mymotiv.com

[12] Muhammad Niswar *et al.*, "A Low Cost Wearable Medical Device for Vital Signs Monitoring in Low-Resource Settings," *Int. J. Electr. Comput. Eng.*, 2019, doi: 10.11591/ijece.v9i4.pp2321-2327.

[13] S. Adibi, *Mobile Health: A Technology Road Map*. 2015. doi: 10.1007/978-3-319-12817-7.

[14] "Sensing Materials: 2D Semiconductors for Biosensing," 2023. doi: 10.1016/b978-0-12-822548-6.00049-2.

[15] F. Fang, S. Aabith, S. Homer-Vanniasinkam, S. Homer-Vanniasinkam, and M. K. Tiwari, "High-resolution 3D printing for healthcare underpinned by small-scale fluidics," 2017. doi: 10.1016/B978-0-08-100717-4.00023-5.

[16] "Machine Learning-Based Automatic Cardiovascular Disease Diagnosis Using Two ECG Leads," 2023, doi: 10.48550/arxiv.2305.16055.

[17] N. J. Camm, "Machine Learning Model Predicting the Likelihood of a Patient Developing Cardiovascular Disease Based on Their Medical History and Risk Factors," *Am. J. Biomed. Sci. Res.*, 2023, doi: 10.34297/ajbsr.2023.18.002429.

[18] P. Lukowicz, U. Anliker, J. A. Ward, G. Tröster, E. Hirt, and C. Neufelt, "AMON: a wearable medical computer for high risk patients," 2002, doi: 10.1109/ISWC.2002.1167230.

[19] S. Alharbi *et al.*, "Oxygen saturation measurements from green and orange illuminations of multi-wavelength optoelectronic patch sensors," *Sensors*, 2018, doi: 10.3390/S19010118.

[20] T. Tamura, Y. Maeda, M. Sekine, and M. Yoshida, "Wearable Photoplethysmographic Sensors—Past and Present," *Electronics*, 2014, doi: 10.3390/ELECTRONICS3020282.

[21] D. Castaneda, A. Esparza, M. Ghamari, C. Soltanpur, and H. Nazeran, "A review on wearable photoplethysmography sensors and their potential future applications in health care.," *J. Biosens. Bioelectron.*, 2018, doi: 10.15406/IJBSBE.2018.04.00125.

[22] Y.-X. Zhao, Z.-X. Lu, Y.-Z. Hsieh, S.-S. Lin, and P.-Y. Chiang, "The Wearable Physical Fitness Training Device Based on Fuzzy Theory," *Appl. Sci.*, 2021, doi: 10.3390/APP11219976.

[23] L. Zhang, J. Xie, A. Antonidoss, and M. Anbarasan, "Activity classification and analysis during sports training session using fuzzy model," *J. Intell. Fuzzy Syst.*, 2021, doi: 10.3233/JIFS-219042.

[24] L. Venica, E. N. Irawan, and D. I. H. Putri, "IoT with Firebase: Smart Ring Android App Using MAX30100 for Fatigue Detection," *J. Electr. Electron. Inf. Commun. Technol.*, vol. 6, no. 1, pp. 8–15.

[25] E. P. Nikmatuzaroh, R. Setiawan, and N. F. Hikmah, "Multimodal Instrumentations as Fatigue Detection Using Fuzzy Logic Method," *J. Biomim. Biomater. Biomed. Eng.*, 2022, doi: 10.4028/p-jm1fkf.

[26] R. de la Vega, H. Anabalón, C. Jara, E. Villamil-Cabello, M. Chervellino, and Á. Calvo-Rodríguez, "Effectiveness of Mobile Technology in Managing Fatigue: Balert App.," *Front. Psychol.*, 2021, doi: 10.3389/FPSYG.2021.704955.

[27] "Yuwell. (2020). YX102 Fingertip Pulse Oximeter User Manual. Jiangsu Yuyue Medical Equipment & Supply Co., Ltd."

[28] *ISO 80601-2-61:2017, Medical electrical equipment – Particular requirements for basic safety and essential performance of pulse oximeter equipment.*

[29] J. Allen, "Photoplethysmography and its application in clinical physiological measurement," *Physiol. Meas.*, vol. 28, no. 3, pp. R1–R39, Mar. 2007, doi: 10.1088/0967-3334/28/3/R01.

ISSN 2355-3286

Six-Axis Force–Torque Analysis of a Flexible-Tube Wrist for Misaligned Ports in Robotic EV Charging

Raihan Yusuf Rifansyah[1], Agus Heri Setya Budi[2], Hendri Maja Saputra[3]
[1, 2] Department of Electrical Engineering Education, Indonesia University of Education, Bandung, Indonesia
[1] raihanysf2013@upi.edu, [2] agusheri@upi.edu
[3] Research Center for Smart Mechatronics, National Research and Innovation Agency – BRIN, Bandung, Indonesia
[3] hend037@brin.go.id

Accepted on August 02, 2025
Approved on December 03, 2025

***Abstract* — As electric vehicle (EV) adoption accelerates, the demand for reliable autonomous charging systems in unstructured environments is growing. A critical challenge in these systems is achieving precise plug-port alignment, where vision-based methods often leave residual errors that can damage connectors. While passive compliance using flexible components is a promising solution, the complex contact mechanics of such materials under misalignment remain under-characterized. This paper presents a systematic 6-axis force-torque characterization of a flexible-tube wrist for robotic electric vehicle (EV) charging under various angular misalignments. Robotic plug insertion often relies on simplified models that fail to capture the complex contact dynamics of compliant mechanisms, limiting system robustness. To address this, we developed an experimental platform based on a cartesian robot with a roll–pitch–yaw wrist to measure full force–torque profiles during quasi-static insertions with controlled misalignments ranging from −8° to +8° in pitch and yaw. The results reveal a highly non-linear and asymmetric response, quantitatively demonstrated by a contact onset that shifts from a maximum depth of 45.8 mm at 0° to as early as 31.8 mm at +8° yaw, and peak axial forces reaching -18 N in pitch and -24 N in yaw. This asymmetry has practical implication, where a -5-degree pitch resulted in insertion failure while an equivalent +5-degree was successful. From this dataset, unique and repeatable force signatures were identified for each condition, providing a foundational basis for hybrid control strategies with force sensing to handle the final delicate insertion.**

***Index Terms*— Asymmetric Response; Robotic Charging; Compliant Mechanism; Flexible Tube; Force Measurement.**

I. INTRODUCTION

The growing adoption of electric vehicles (EVs) has driven intensive research on autonomous charging systems, which are essential for scalable, hands-free energy replenishment in future mobility ecosystems [1]. Unlike conventional fueling, EV charging requires precise plug insertion with minimal tolerance, making automation highly sensitive to alignment and contact quality. Characterizing force and torque dynamics is a critical step in designing compliant robotic systems, from industrial automation to wearable exoskeletons [2]. Consequently, various innovative architectures have been developed, including mobile or rail-mounted robotic chargers designed for structured environments such as parking garages [3].

Achieving precise alignment is challenging due to tight mechanical tolerances and the lack of standardized port geometries across vehicle models [1, 4]. Most approaches rely on vision-based systems using methods from deep learning to shape-based matching to detect the port location [4-6]. However, these systems have low robustness to environmental variations such as lighting and reflections [1, 4]. Studies show that even after seemingly successful vision-guided insertion, residual misalignments can persist, causing mechanical strain on the connector and port [4]. This underscores the need for complementary strategies for the final phase of plug insertion.

To address these residual errors, researchers incorporate compliance into the robotic systems, broadly classified into two approaches [7]. The first is active compliance, where force feedback actively modulates robot motion through algorithms such as impedance or admittance control [6, 8]. The second is passive compliance, which uses mechanical elements that deform upon contact to accommodate misalignment. Examples include elastic compensation units [9] or end-effectors with integrated flexible plugs [10]. However, flexible components introduce control challenges, notably complicating manipulator inverse kinematics [11].

Concurrently, other data-driven approaches have explored alternative sensing modalities to infer contact state or developed advanced learning-based control strategies for contact-rich tasks [12]. Research has shown the utility of Inertial Measurement Units (IMUs) to analyze vibration signals for the purpose of collision classification (determining if a contact is safe or unsafe)

[13] or for collision localization (estimating where on the port face contact occurred) [14]. Another novel approach involved developing the flexible tube itself into a sensor, using an embedded magnetic sensor and an LSTM network to predict interaction forces rather than measuring them directly [15].

However, despite numerous proposed control architectures and sensing modalities, the fundamental contact mechanics of a passively compliant plug, such as one made from thermoplastic polyurethane (TPU), under controlled angular misalignment remain uncharacterized. Understanding these force dynamics is essential for ensuring the long-term reliability, as uncontrolled insertion forces can cause mechanical wear, degradation, and eventual failure of the electrical connectors [16, 17]. To address this gap, this paper provides a systematic experimental characterization of the 6-axis forces and torques on a flexible-tube wrist. By directly measuring the force-position-torque response, we reveal nonlinearities and pronounced asymmetries that challenge simplified rigid-body models.

II. Materials and Methods

A. Experimental Platform

The experimental platform comprises three stepper-driven linear axes (X, Y, Z) mounted on a modular aluminum frame and controlled by an Arduino Uno with a CNC Shield. The vehicle-side charging port, a standard IEC 62196-2 receptacle with its electrical pins removed to isolate mechanical forces, is mounted on a fixture with manually adjustable pitch and yaw angles ranging from −8° to +8°. The plug is advanced linearly along the Z-axis to simulate an insertion under constant angular misalignment. For passive compliance, the plug is attached to the moving stage using a 3D-printed hollow tube. This component is the same unit previously validated in [15] and is fabricated from Thermoplastic Polyurethane (TPU) with a 95A Shore Hardness, 0% infill, and 1 mm wall thickness to allow elastic bending while effectively transmitting contact forces to the upstream sensor.

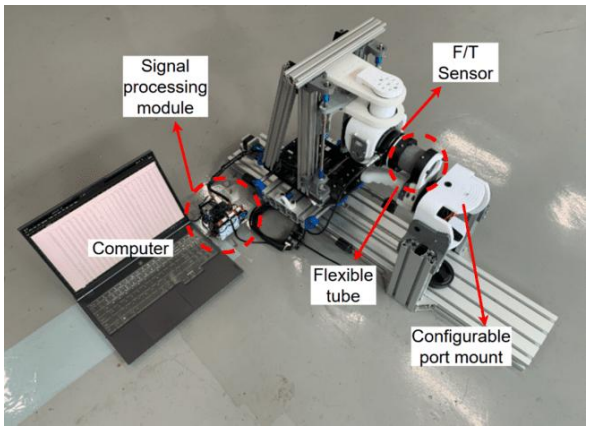

Fig. 1. Experimental Platform for Force–Torque Characterization of the Flexible-Tube Wrist Under Pitch and Yaw Misalignments.

The experimental platform, shown in Fig. 1, was constructed using a modular T-slot aluminum frame that forms the main base, Y-axis carriage, Z-axis column, and the configurable port mount structure. Nema 17 stepper motors drive all the three axes with T8 leadscrews equipped with anti-backlash nuts, while linear guidance is provided by LM13UU bearings. The majority of custom components, including motor mounts, bearing blocks, the port fixture, and the plug assembly, were fabricated from 3D-printed PLA+. The system is controlled by two Arduino Uno microcontrollers; the first uses a CNC Shield for motion control of the three stepper motors, while the second is dedicated to acquiring data from the F/T sensor. The two microcontrollers communicate via I2C to synchronize the force-torque data with the platform's position, which is then sent to a computer for data acquisition.

B. System Properties and Coordinate Frames

A right-hand coordinate frame centered at the base of the flexible tube is used for all analyses, as illustrated in Fig. 2. The X-axis represents the lateral motion (left/right) with pitch as rotation about this axis; the Y-axis represents the vertical motion (up/down) with yaw as rotation about this axis; and the Z-axis represents the insertion motion (forward/backward). Forces (Fx, Fy, Fz) and torques (Tx, Ty, Tz) are reported with respect to this coordinate frame.

The kinematic properties of the experimental platform include an operational workspace of 140 x 170 x 178 mm (X, Y, Z respectively). Platform motion is described by a kinematic model relating the actuator positions (joint space) to the end-effector's position (task space). The joint space vector is $q = [q_x, q_y, q_z]^T$, where each element corresponds to the linear displacement of a stepper-driven axis. The task space position vector is $P = [P_x, P_y, P_z]^T$. For this 3-DOF Cartesian manipulator, forward and inverse kinematics are given by the direct identity transformation $P = q$.

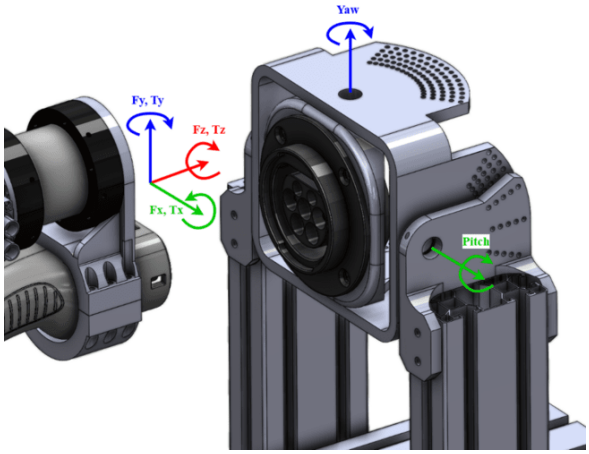

Fig. 2. Coordinate Frame Definitions for The Flexible-Tube Wrist, Indicating Lateral (X), Vertical (Y), and Axial (Z) axes.

C. Force-Torque Sensing and Data Acquisition

A six-axis force–torque sensor (AFT200, Aidin Robotics) is mounted between the moving carriage and the flexible tube. The sensor measures tri-axial force and torque data (Fx, Fy, Fz, Tx, Ty, Tz) with ranges of ±200 N and ±15 Nm and resolutions of 0.15 N and 0.015 Nm, respectively. Data is acquired via a CAN interface and synchronized with the platform position data. Because the flexible tube deforms during contact, the recorded Z-axis position represents the platform displacement and serves as a relative index of motion progression rather than the absolute plug-tip position.

D. Experimental Procedure

specific pitch or yaw angle. The plug was advanced at a constant low velocity along the Z-axis for a total travel distance of 70 mm to capture the entire contact event. The motion was considered quasi-static to minimize inertial effects, so that the measured forces primarily resulted from elastic deformation. This procedure was repeated 10 times for each of the 17 angular offsets (from −8° to +8° in 1° increments) for both pitch and yaw. All data collection was conducted in an open-loop, feedforward manner without active feedback control or external pose tracking.

A total travel distance of 70 mm was selected to ensure that the entire insertion process was fully captured under all misalignment conditions. Preliminary tests indicated that initial contact occurred as late as 45.8 mm for the 0° configuration and as early as 31.8 mm for ±8°; therefore, a shorter travel range would risk failing to reach the final seating or failure region, which typically emerges around 55–60 mm. Extending the travel to 70 mm provides a sufficient margin to observe the complete progression of events from free-space motion, through initial impact and continuous elastic deformation, to the final resting state. This margin ensures that no critical interaction or steady-state behavior is truncated while remaining within the safe bending limits of the flexible tube.

E. Data Processing and Analysis

The analysis focused on the 30–60 mm segment of the insertion path, where the main contact events occurred. Key metrics were extracted from the averaged data of 10 repeated trials for each condition. Contact onset was identified by manual visual inspection of the force-torque profiles, chosen instead of a global automated threshold to better handle variations in initial contact behavior. Onset was defined as the position where the profiles first showed a clear and sustained deviation from the baseline noise.

For the quantitative trend analysis, a critical mechanical event was identified for each trial instead of relying on simple peak values. This event represented the point of maximum mechanical resistance, typically determined by the primary peak in axial force (Fz) or a sharp change in the slope of vertical force (Fy). The 6-axis force-torque vector was extracted at this event position to construct a composite force signature for each misalignment condition. Finally, these signatures were used to analyze trends across all angular conditions, assessing nonlinearity, asymmetry, and cross-axis coupling.

III. Result and Discussion

The experimental data revealed complex, repeatable, and highly asymmetric force-torque profiles that are characteristic of each angular misalignment conditions. These profiles, or force signatures, provide a detailed representation of the mechanical interactions during the insertion process. The following sections present the pitch and yaw signatures, followed by a quantitative analysis of key trends.

The initial analysis examines the three primary force components generated during pitch misalignment. Fig. 3 shows the averaged force profiles for lateral (Fx), vertical(Fy), and axial (Fz) components as a function of insertion position across the full range of negative and positive pitch angles.

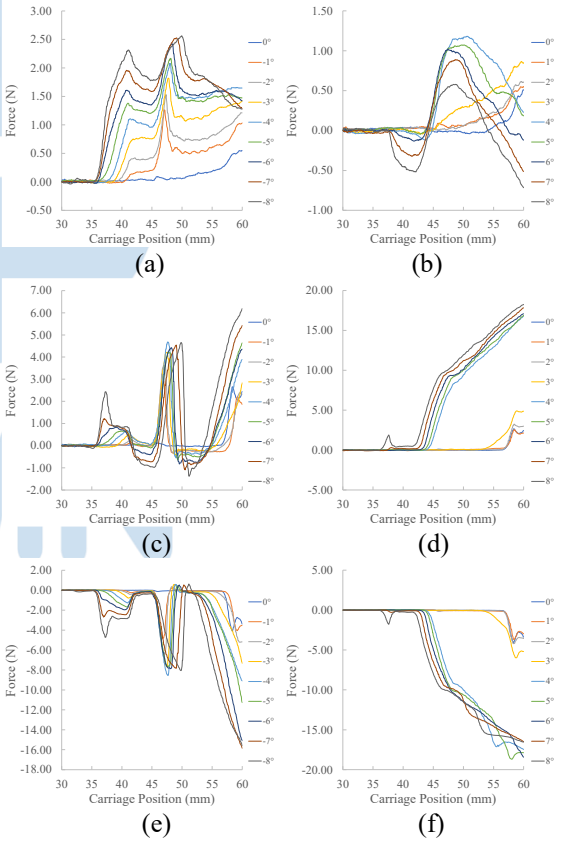

Fig. 3. Force Profiles for Pitch Misalignment Across Insertion Positions: (a) Fx for negative pitch; (b) Fx for positive pitch; (c) Fy for negative pitch; (d) Fy for positive pitch; (e) Fz for negative pitch; and (f) Fz for positive pitch.

The force profiles in Fig. 3 show clear asymmetry between negative and positive pitch. Negative pitch condition (Fig. 3a, 3c, 3e) produces complex, multi-stage contact dynamic with a distinct dual-peak signature in the vertical (Fy) and axial (Fz) forces, indicating stick-slip or jamming. In contrast, the positive pitch condition (Fig. 3b, 3d, 3f) yields

smoother, monotonic force curves but with a higher vertical reaction force (Fy), indicating a more monotonic but high-friction sliding contact.

To complement the force analysis, the torque profiles for pitch misalignment were examined. Fig. 4 displays the three primary torque components, providing insight into the rotational dynamics.

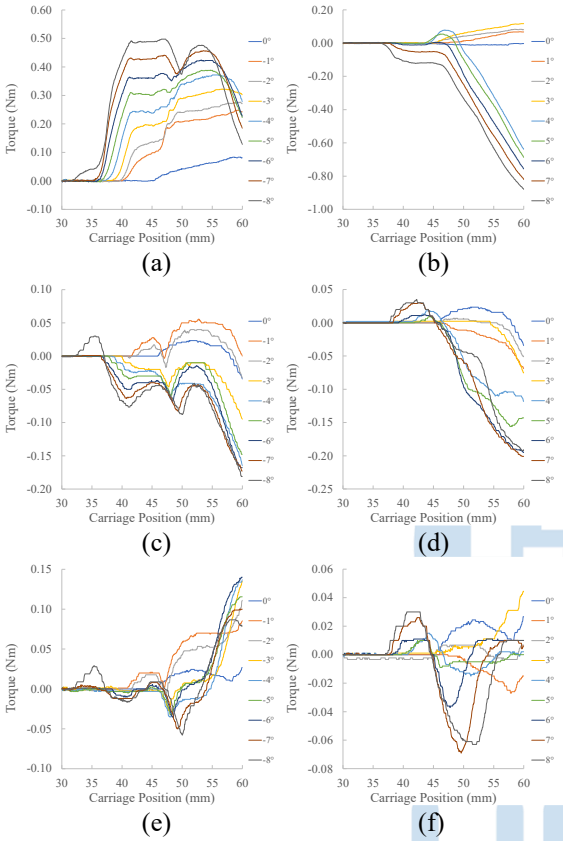

Fig. 4. Torque Profiles for Pitch Misalignment, Highlighting Polarity Reversal and Bending Loads: (a) Tx for negative pitch; (b) Tx for positive pitch; (c) Ty for negative pitch; (d) Ty for positive pitch; (e) Tz for negative pitch; and (f) Tz for positive pitch.

The asymmetry is further detailed in the torque profiles shown in Fig. 4. The primary bending torque (Tx) is a strong directional indicator, showing a complete polarity reversal between negative (Fig. 4a) and positive (Fig. 4b) pitch. Notably, the peak torque magnitude is substantially larger for positive pitch, indicating a greater bending load is imparted on the flexible tube. The secondary and third torques (Ty and Tz) confirm a complex 3D interaction involving both lateral bending and twisting.

The investigation was extended to yaw misalignment. Fig. 5 shows the averaged force profiles for the lateral (Fx), vertical (Fy), and axial (Fz) components under controlled negative and positive yaw deviations, revealing a distinctly different mechanical response compared with pitch.

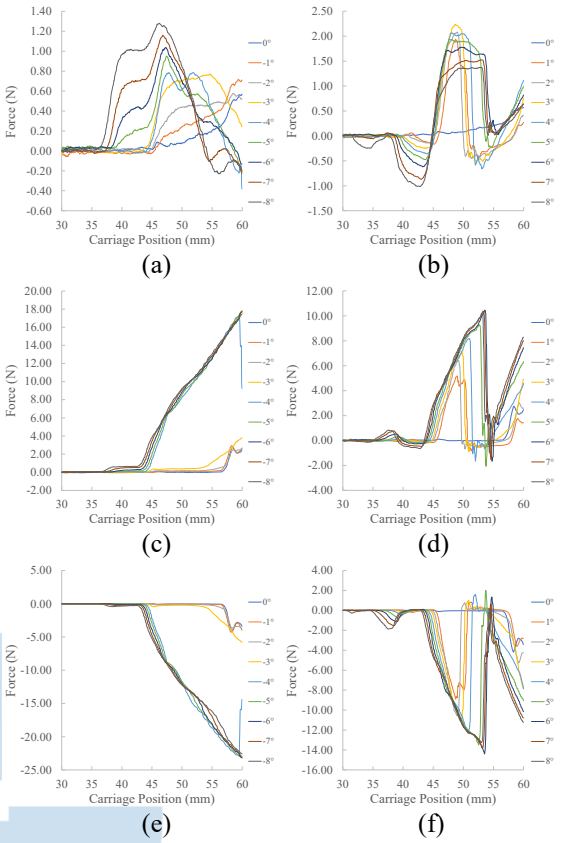

Fig. 5. Force Profiles for Yaw Misalignment Under Positive and Negative Deviations: (a) Fx for negative yaw; (b) Fx for positive yaw; (c) Fy for negative yaw; (d) Fy for positive yaw; (e) Fz for negative yaw; and (f) Fz for positive yaw.

The force profiles in Fig. 5 indicate that the response to positive yaw is significantly more complex and irregular than negative yaw. Under positive yaw, the lateral force (Fx) exhibits a distinct force reversal, beginning with a negative peak as the plug tip makes initial contact with one side of the port flange, followed by a much larger positive peak as it slides and presses against the opposite side. This complex interaction is also reflected in the vertical(Fy) and axial (Fz) forces, which are characterized by sharp transient events and abrupt reversals indicative of a stick-slip dynamic. In contrast, negative yaw (Fig. 5a, 5c, 5e) produces a more predictable and monotonic response, notably in the large coupled vertical (Fy) and axial (Fz) forces, which increase smoothly without the sharp fluctuations observed in the positive yaw condition.

The rotational dynamics under yaw misalignment were analysed by examining the three corresponding torque components. Fig. 6 shows the three primary torque components, providing insight into the rotational dynamics.

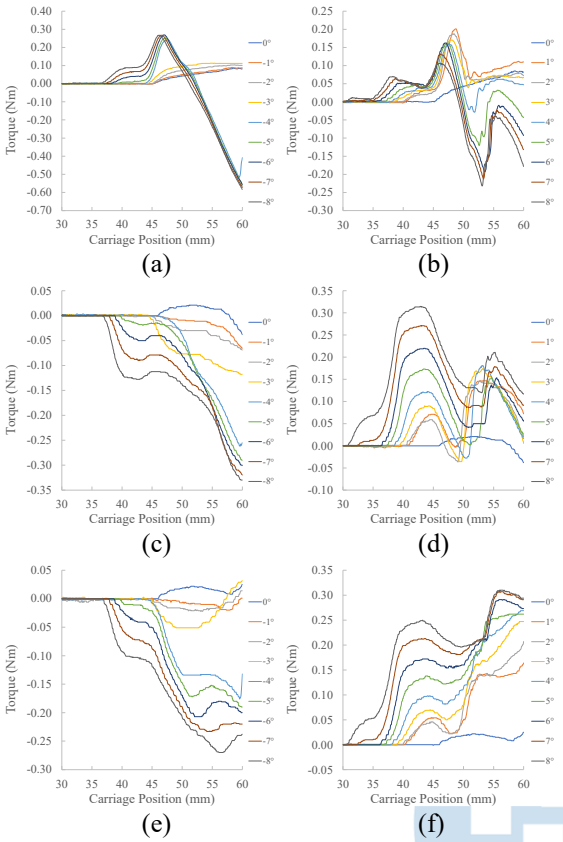

Fig. 6. Torque Profiles for Yaw Misalignment, Showing Strong 3D Coupling Effects: (a) Tx for negative yaw; (b) Tx for positive yaw; (c) Ty for negative yaw; (d) Ty for positive yaw; (e) Tz for negative yaw; and (f) Tz for positive yaw.

The torque profiles in Fig. 6 provide further insight into the rotational dynamics of yaw misalignment. For the primary bending torque (Tx), negative yaw (Fig. 6a) shows two distinct behaviours: for small angles, the torque remains consistently positive, whereas for larger angles, the response transitions to a positive peak followed by a smooth, monotonic reversal into a negative value. In contrast, all positive yaw angles (Fig. 6b) generate a high-gradient, non-monotonic profile, characterized by an initial positive peak that is immediately followed by a sharp reversal to a negative trough, before ending in a fluctuating state. This behaviour suggests a more severe interaction involving phenomena such as snap-through buckling or intermittent slip-stick contact. Lastly, the lateral torque (Ty) and twisting torque (Tz) emerge as highly reliable indicators of yaw direction, exhibiting a clear and systematic polarity reversal between negative and positive angles.

A. Quantitative Analysis of the Contact Onset

To quantify and summarize the observed behaviors, key metrics were extracted from the profiles. Fig. 7 plots the initial contact onset position as a function of the misalignment angle. Both pitch and yaw show a distinct arch-shaped profile, where contact occurs latest near 0° and progressively earlier towards the ±8° extremes. The plot also provides a clear quantitative measure of asymmetry; both profiles are asymmetric, with yaw showing a more pronounced overall difference compared to pitch.

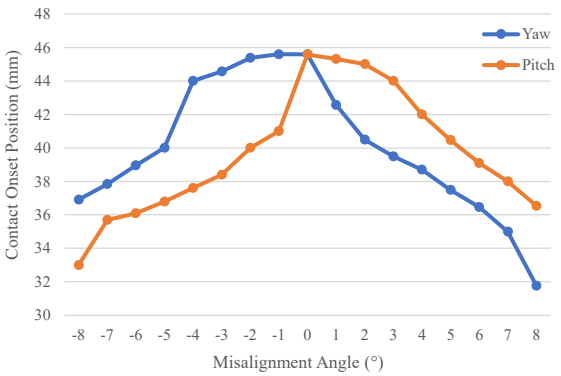

Fig. 7. Contact Onset Position as a Function of Misalignment Angles for Pitch and Yaw.

Fig 7 compares contact onset position versus of the misalignment angle for pitch and yaw. Both exhibit an arch-shaped profile, with contact occurring latest (deepest into the insertion path) near the 0° and progressively earlier as the misalignment increases towards the ±8°. The figure clearly shows that the pitch and yaw profiles differ in both shape and magnitude.

The arch-shaped trend is intuitive because a greater initial tilt causes the plug's leading edge to engage with the port chamfer earlier in its forward travel. More importantly, the plot provides a quantitative measure of asymmetry for both axes. The yaw profile is highly asymmetric, with positive yaw angles producing different onset positions than negative ones. The pitch profile also shows asymmetry, as contact at +8° occurs at a distinctly different position than at -8°. These results indicate that the initial contact dynamics depend on misalignment direction for both pitch and yaw, which is a critical insight for predictive control model development.

B. Quantitative Analysis of the Primary Mechanical Event

Further analysis was conducted by identifying the position of the primary mechanical event, which corresponds to the moment of maximum resistance in each trial. Unlike a simple maximum value search, the position of this event was determined for each angle through manual visual inspection to accurately capture its specific characteristics. This critical event was identified by distinct features in the profiles, such as a transient reversal with the highest magnitude or a significant change in the slope of a primary force component within a specific range of travel. By defining the event based on these physical phenomena rather than a simple peak, a more consistent and meaningful comparison across different misalignment conditions could be achieved. The 6-axis force-torque vector was then extracted at this identified event position for subsequent quantitative analysis.

Fig. 8 illustrates how this event positions shift along the insertion path. The plot reveals at least two distinct mechanical regimes both for pitch and yaw: the event occurs very late for small angles but shifts to a much earlier position for larger angles, indicating a fundamental change in contact mode.

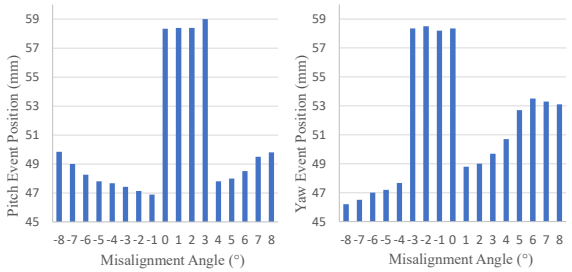

(a) (b)

Fig. 8. Position of the primary mechanical event as a function of pitch and yaw misalignment: (a) Event position for pitch; and (b) Event position for yaw.

The primary mechanical event position shifts along the insertion path as a function of the pitch and yaw misalignment angles as shown in Fig. 8. The data reveal a distinct, non-uniform pattern both for pitch and yaw, where the event occurs late in the path for small angles (0° to +3°) for pitch and (-3° to 0°) for yaw but shifts to a much earlier position for larger angles."

The large shift in the event position suggests the presence of two distinct mechanical regimes. For small misalignments, the system operates in a compliance zone, where no hard jamming occurs and the maximum force results from friction building up near the end of insertion. For larger misalignments, the system enters a hard contact zone, where a distinct earlier mechanical event, likely jamming or high-stress bending, becomes the dominant feature. The yaw response asymmetry further indicates that the regime transition depends on misalignment direction.

To quantify the system asymmetry and sensitivity, the magnitudes of the three primary force components were extracted at each event position. Fig. 9 presents these force values as functions of misalignment angle for both pitch and yaw.

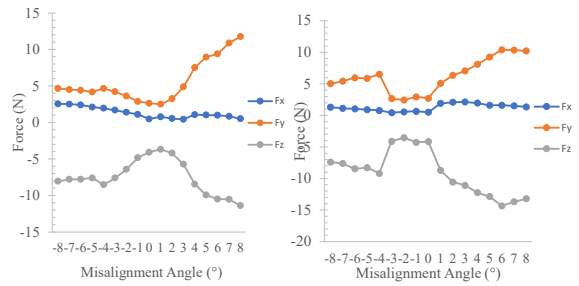

(a) (b)

Fig. 9. Force Event as a Function of Misalignment Angle: (a) Force event for pitch; and (b) Force event for yaw.

Fig. 9 summarizes the event force magnitudes for the Fx, Fy, and Fz, extracted at the primary mechanical event for both pitch and yaw. The plot shows the nonlinear relationship between misalignment angle and the resulting reaction forces.

This plot provides the strongest quantitative evidence of the system force asymmetry. The pitch analysis (Fig. 9a) shows distinct trend in dominant forces (Fy and Fz) for negative and positive angles. The yaw analysis (Fig. 9b) is even more pronounced: negative yaw is dominated by a large coupled vertical force (Fy), while positive yaw is dominated by a much larger primary lateral force (Fx). These results confirm that the nature of mechanical resistance fundamentally differs depending on yaw direction.

Finally, to complete the quantitative analysis, the torque events were extracted at the mechanical event. Fig. 10 presents the corresponding torque magnitudes for the three rotational components (Tx, Ty, Tz) extracted at the primary mechanical event. The plot illustrates the sensitivity and directional nature of the torque response.

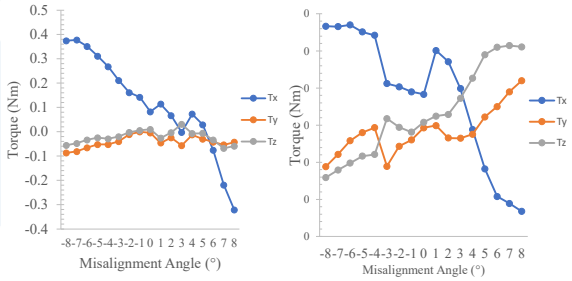

(a) (b)

Fig. 10. Torque Event as a Function of Misalignment Angle: (a) Torque event for pitch; and (b) Torque event for yaw.

The torque event analysis identifies the components that best indicate direction. For pitch misalignment (Fig. 10a), the primary bending torque (Tx) demonstrates a clear and consistent polarity reversal, with positive values for negative pitch and negative values for positive pitch. Similarly, for yaw misalignment (Fig. 10b), the lateral (Ty) and twisting (Tz) torques also show a perfect polarity reversal, making them reliable indicators for sensor-based control. The complex, non-monotonic behaviour of the other torque components further confirms strong and unpredictable 3D coupling effects.

C. Qualitative Validation of Final Plugging States

To provide qualitative validation and link quantitative data with physical outcomes, final plugging states were visually documented for representative misalignment angles. This visual inspection confirms whether insertion was successful or failed under different conditions.

The final plugging states for key pitch misalignment angles are presented first. Fig. 11 shows a side-view comparison for -5°, 0°, and +5° pitch angles to illustrate the system's functional asymmetry

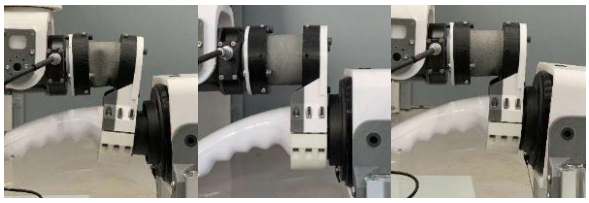

(a) (b) (c)

Fig. 11. Final Plugging State for Pitch Misalignment: (a) -5°; (b) 0°; and (c) +5°.

As shown in Fig. 11, a clear correlation between the force signatures and the insertion is evident. For the 0° condition (Fig. 11b), the plug is perfectly seated, matching the observed low-force profiles. At a +5° pitch misalignment (Fig. 11c), the system's passive compliance accommodates the error, allowing a complete insertion.

A key finding is the functional asymmetry shown in this comparison. While +5° misalignment results in a successful insertion, -5° misalignment causes insertion failure, where the plug is visibly canted and cannot be fully seated (Fig. 11a). This failure directly corresponds to the irregular dual-peak force profile observed for negative pitch, confirming it as a more challenging condition and defining an operational limit for the passive compliance mechanism.

Next, the final plugging states for key yaw misalignment angles were documented. Fig. 12 compares the outcomes for the extreme angles of -8° and +8°, with the 0° condition as a baseline.

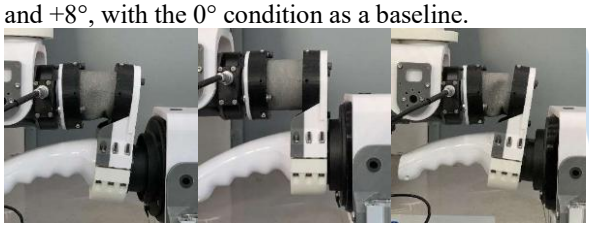

(a) (b) (c)

Fig. 12. Final Plugging State for Yaw Misalignment: (a) -8°; (b) 0°; and (c) +8°.

As shown in Fig. 12, the 0° condition (Fig. 12b) again serves as a baseline for a successful insertion. However, the outcomes at the extreme angles of -8° (Fig. 12a) and +8° (Fig. 12c) both resulted in insertion failure, where the plug became canted and could not be fully seated. This demonstrates that while the system can accommodate moderate yaw deviations, its operational limit is exceeded at these extreme angles.

A closer analysis of the failure modes reveals subtle differences between the two conditions. The final canted state at +8° yaw appears more severe or misaligned compared to the -8° condition. This visual evidence reinforces the quantitative findings that the underlying mechanical stresses and irregular dynamics are significantly greater for positive yaw. This underscores that not only the success of the insertion, but also the nature of the failure can vary significantly depending on the direction of misalignment.

D. Interpretation of Asymmetric Contact Mechanics

The pronounced asymmetry observed in both force and torque responses is a key finding of this study. It results from the complex interaction between the compliant tube's deformation and the plug-port interface geometry. Different contact points on the port's chamfer for positive and negative angles cause the plug to bend and twist in distinct ways. This is quantitatively confirmed in the event force analysis (Fig. 9), where negative yaw is dominated by a large coupled vertical force (Fy), while positive yaw produces a much larger primary lateral force (Fx). This difference in force magnitudes and dynamic stability is visually confirmed by the qualitative validation (Fig. 11), where a -5° pitch results in a insertion failure (canting), while a +5° pitch leads to a successful insertion. Furthermore, the existence of strong cross-axis coupling, such as the significant vertical force (Fy) generated during horizontal yaw misalignment, underscores that the interaction is an inherently 3D phenomenon that cannot be adequately described by simpler, 2D rigid-body models.

E. The Force Signature Concept and Implications for Control

The distinct and repeatable nature of the 6-axis profiles for each misalignment condition gives rise to the concept of a unique force signature. Each signature, defined by the instantaneous 6-axis force-torque vector at the primary mechanical event, acts as a mechanical fingerprint containing rich information about the state of contact, as quantitatively demonstrated by the unique component magnitudes (Fig. 9, Fig. 10) and event timing (Fig. 8) for each angle. This finding has significant implications for a hybrid control strategy; for example, the signature for a -5° pitch, which leads to insertion failure, is fundamentally different from that of a +5° pitch, which results in success. While a vision system can handle the initial coarse alignment, these force signatures are invaluable for the final, delicate insertion phase. By recognizing characteristic features within a signature, a control algorithm could diagnose the direction, approximate magnitude, and even the potential outcome of an insertion error in real-time, providing a strong basis for robust, adaptive force-guided controllers that can react intelligently to specific conditions.

IV. CONCLUSION

This study presents a systematic characterization of six-axis force and torque responses from a flexible-tube wrist under pitch and yaw misalignments ranging from −8° to +8°. The results reveal a non-linear and directionally asymmetric mechanical behavior, which was found to be both quantitative and functional. For

instance, a -5° pitch misalignment resulted in insertion failure, whereas an equivalent +5° was successful. Key quantitative findings include a contact onset that shifts from a maximum depth of 45.8 mm at 0° to as early as 31.8 mm at +8° yaw, and peak final plugging state axial forces (Fy) reaching -18 Newtons in pitch and -24 Newton in yaw. A key contribution is the identification of unique and repeatable force signatures for each misalignment condition. These patterns provide a foundation for developing more robust, adaptive control strategies in autonomous EV charging systems.

Initial attempts to create a validating finite element model were unsuccessful, as the nonlinear analysis in SolidWorks Simulation consistently failed to converge due to the large deformations and geometric nonlinearity of the thin-walled TPU component. A successful quantitative validation is therefore a key direction for future work, requiring a more sophisticated approach with advanced solvers such as arc-length or Riks methods, combined with a calibrated hyperelastic material model. The ultimate goal is to leverage the dataset presented here to train a machine-learning model for a hybrid alignment strategy. This approach would use a vision system for coarse localization of the charging port before transitioning to a force-guided control mode, which would use the identified signatures to correct residual errors during the final, delicate insertion phase, combining the strengths of both sensing modalities for a highly robust system.

REFERENCES

[1] H. M. Saputra, N. S. M. Nor, E. Rijanto, M. Z. Md Zain, I. Z. Mat Darus, and E. Yazid, "A review of robotic charging for electric vehicles," *International Journal of Intelligent Robotics and Applications,* vol. 8, no. 1, pp. 193-229, 2024, doi: 10.1007/s41315-023-00306-x.

[2] D. Rodríguez Jorge, J. Bermejo García, A. Jayakumar, R. Lorente Moreno, R. Agujetas Ortiz, and F. Romero Sánchez, "Force and Torque Characterization in the Actuation of a Walking-Assistance, Cable-Driven Exosuit," *Sensors*, vol. 22, no. 11, doi: 10.3390/s22114309.

[3] A. Hu *et al.*, "SkyvoltRobot: A Novel Rail-Mounted Charging Robot for Electric Vehicles," *Procedia Computer Science,* vol. 250, pp. 274-281, 2024, doi: https://doi.org/10.1016/j.procs.2024.11.036.

[4] J. Miseikis, M. Rüther, B. Walzel, M. Hirz, and H. Brunner, "3D Vision Guided Robotic Charging Station for Electric and Plug-in Hybrid Vehicles," 2017, doi: 10.48550/arXiv.1703.05381.

[5] P. Quan, Y. Lou, H. Lin, Z. Liang, and S. Di, "Research on Fast Identification and Location of Contour Features of Electric Vehicle Charging Port in Complex Scenes," *IEEE Access,* vol. 10, pp. 26702-26714, 2022, doi: 10.1109/ACCESS.2021.3092210.

[6] P. Sun *et al.*, "Research on autonomous positioning and adaptive compliant plugging strategies of intelligent charging robots," *Computers in Industry,* vol. 168, p. 104287, 2025, doi: https://doi.org/10.1016/j.compind.2025.104287.

[7] M. Zhu, D. Gong, Y. Zhao, J. Chen, J. Qi, and S. Song, "Compliant Force Control for Robots: A Survey," *Mathematics*, vol. 13, no. 13, doi: 10.3390/math13132204.

[8] H. Zhang, W. Zhu, and Y. Huang, "A research on the control strategy of automatic charging robot for electric vehicles based on impedance control," *Journal of Physics: Conference Series,* vol. 2303, no. 1, p. 012085, 2022, doi: 10.1088/1742-6596/2303/1/012085.

[9] J. Bucher, J. Knipschild, and B. Künne, "Development and evaluation of an automatic connection device for electric cars with four DOFs and a control scheme based on infrared markers," *International Journal of Mechatronics and Automation,* vol. 8, p. 1, 01/01 2021, doi: 10.1504/IJMA.2021.10043805.

[10] Y. Lou and S. Di, "Design of a Cable-Driven Auto-Charging Robot for Electric Vehicles," *IEEE Access,* vol. 8, pp. 15640-15655, 2020, doi: 10.1109/ACCESS.2020.2966528.

[11] H. M. Saputra, R. Y. Rifansyah, C. H. A. H. B. Baskoro, N. S. M. Nor, E. Rijanto, and A. Pahrurrozi, "Comparative Study of Machine Learning Models for Inverse Kinematic Prediction of a Flexible-Tube Wrist Mechanism in Robotic Charging Stations," in *2024 IEEE International Conference on Smart Mechatronics (ICSMech)*, 19-21 Nov. 2024, pp. 152-158, doi: 10.1109/ICSMech62936.2024.10812340.

[12] Y. Wang, C. C. Beltran-Hernandez, W. Wan, and K. Harada, "An Adaptive Imitation Learning Framework for Robotic Complex Contact-Rich Insertion Tasks," *Frontiers in Robotics and AI,* Original Research vol. 8 - 2021, 2022. [Online]. Available: https://www.frontiersin.org/journals/robotics-and-ai/articles/10.3389/frobt.2021.777363.

[13] H. Lin, P. Quan, Z. Liang, D. Wei, and S. Di, "Enhancing Safety in Automatic Electric Vehicle Charging: A Novel Collision Classification Approach," *Applied Sciences*, vol. 14, no. 4, doi: 10.3390/app14041605.

[14] H. Lin, P. Quan, Z. Liang, Y. n. Lou, D. Wei, and S. Di, "Precision Data-Driven Collision Localization with a Dedicated Matrix Template for Electric Vehicle Automatic Charging," *Electronics*, vol. 13, no. 3, doi: 10.3390/electronics13030638.

[15] H. Saputra *et al.*, "Three-axis flexible tube sensor with LSTM-based force prediction for alignment of electric vehicle charging ports," *Journal of Mechatronics, Electrical Power, and Vehicular Technology,* vol. 15, pp. 208-219, 12/31 2024, doi: 10.55981/j.mev.2024.1104.

[16] Y. Meng and W. Ren, "Investigation on failure mechanism of electrical connectors under repetitive mechanical insertion and withdrawal operations," *IOP Conference Series: Materials Science and Engineering,* vol. 1207, no. 1, p. 012011, 2021, doi: 10.1088/1757-899X/1207/1/012011.

[17] L. Xu, S. Ling, and D. Li, "Insertion force quality consistency investigation of electrical connector," in *2016 IEEE 11th Conference on Industrial Electronics and Applications (ICIEA)*, 5-7 Jun. 2016, pp. 2395-2399, doi: 10.1109/ICIEA.2016.7603994.

ISSN 2355-3286

IoT-Based Fire Detection System Using a Flame Detector and Arduino Uno R4 Wi-Fi

Ratih Kusuma Dewi[1*],Ivan Fadhliansyah[2], Riado Ma'rufi[3], Deddy Setyawan[4], Dwiki Ar-Raiyyan Lubis[5]
[1,2,3,4,5]Department of Teknologi Instrumentasi Industri Petrokimia, Politeknik Industri Petrokimia Banten, Banten, Indonesia
[1*]ratih.kusuma@poltek-petrokimia.ac.id

Accepted on November 03, 2025
Approved on December 12, 2025

***Abstract*— Based on data from the DORS POLRI application, a total of 935 fire incidents were recorded from January to October 7, 2024. The locations with the highest frequency of fires were residential areas, with 704 reported cases. These data indicate the need for a fire detection security system capable of providing early warning as a risk-mitigation measure to prevent casualties during fire incidents.The system designed in this study is based on the Internet of Things (IoT) and is equipped with a notification feature that sends alerts to a Telegram bot when the sensor detects the presence of fire. The results of this study show that even after reducing the sensor sensitivity 33the sensor still performs adequately in detecting fire. It can detect real fire at a distance of 35 cm and can still detect light from a bulb at a distance of approximately 95 cm. However, the sensor is unable to detect paraffin fire at a distance of 10–50 cm because the infrared wavelength emitted by paraffin is outside the detectable range of the sensor. Additionally, the sensor cannot detect virtual fire or light from a mobile phone flashlight because these light sources do not emit infrared radiation that matches the operating characteristics of the sensor.Thus, the system has been proven effective in detecting fire and sending automatic real-time notifications to Telegram, enabling users to respond quickly when there is a potential fire hazard.**

***Index Terms*— Fire, Flame Detector, IoT, Paraffin.**

I. INTRODUCTION

Fire is a major threat to the environment, industry, public facilities, and human life. The losses caused by fire include damage to property and assets, and in severe cases, can lead to casualties [1] According to experts, fire is defined as the presence of unwanted or uncontrolled flames [13]. Fires can occur at any time and are unpredictable [14]; therefore, to prevent major losses, a fire detection security system with early warning capabilities is required to mitigate fire risks [8].

In fire detection systems, flame detectors or flame sensors are often chosen because of their fast detection capability in identifying fire occurrences [5][6] and their adjustable sensitivity. These sensors typically detect light emissions within the infrared (IR) or ultraviolet (UV) spectrum and immediately send a signal when a flame is detected.

According to data from the DORS POLRI application, there were 935 fire incidents recorded from January to October 7, 2024. The locations most frequently affected were residential areas (704 incidents), shops (63), offices (29), schools (17), warehouses (16), and others (106) [2]. This data shows that the risk of fire remains relatively high, necessitating a reliable early detection system to minimize material losses and casualties.

Previous research by Denny and Budy (2022), titled "Prototype of a Fire Detection Device Using a Flame Sensor and MQ-2 Based on Arduino Uno," explains that the flame detector was able to detect fire at a distance of 5–25 cm, triggering an alarm and activating an LED indicator [3]. Furthermore, in the study conducted by Dian et al., titled "Arduino-Based Fire Detection System Using a Flame Detector and MQ-2 Sensor," the test results showed that the flame detector could detect fire at distances ranging from 5 cm to 40 cm. At a distance of 5 cm, the average detection time was approximately 0.57143 seconds; at 10 cm it was 1.5714 seconds; at 20 cm it was 8 seconds; at 30 cm it was 13 seconds; and at 40 cm it was 9 seconds [4]. Another study conducted by Rima et al. demonstrated that the flame detector was capable of detecting the presence of fire at distances from 20 cm up to 250 cm [12]. In the study conducted by Ruibing and Dhirtiman, a fire detection method using CNN is presented, making the fire detection system more efficient and effective [16].

The system is designed based on the Internet of Things (IoT) and is equipped with real-time notification delivery to a Telegram bot when the flame detector sensor detects the presence of fire. In addition, the system sends information regarding water availability in the storage tank using an ultrasonic sensor. With the integration of Telegram notifications, users can easily receive status updates [9][10] and monitor environmental conditions in real time without being physically present at the location. The system is also equipped with a water pump that activates automatically when fire is detected and stops operating once the fire is no longer detected.

II. METHODOLOGY

The methodology used in this study is the prototype development method, followed by direct testing of the system. The testing phase was conducted 3–5 times for each test component. The test components consisted of a yellow bulb, phone flashlight, virtual fire, real fire, and paraffin. The testing distance for each component ranged from 5 cm to ±95 cm. During testing, the flame detector was brought close to each test component at predetermined distances to observe the sensor's response.

The research stages began with the creation of a system block diagram aimed at identifying the main components used and the interconnections between them. This block diagram provides an overview of the system's workflow, from the input to the output stage.

Next, a system flowchart was created to illustrate the detailed logic flow of the system, describing how the system operates—from the fire detection process and water availability check to the activation of the pump and alarm. The subsequent stage involved hardware design, which included assembling key components such as the Arduino Uno R4 WiFi, flame sensor, ultrasonic sensor, LCD, water pump, indicator LEDs, and buzzer. All components were connected according to the previously designed block diagram.

Following this, the software design stage was carried out by writing a program for the Arduino to control the entire system operation—from reading sensor data to managing outputs and displaying information on the LCD. Once the hardware and software were integrated, direct testing of the system was conducted to ensure that all components functioned as intended. The testing involved simulating the presence of fire and observing the system's response to this condition.

The results of these tests were then used to evaluate the performance and effectiveness of the developed automatic fire detection system prototype.

A. Block Diagram

The first stage of this research is the development of a block diagram, which is a diagram that illustrates the workflow and the main components of a system [15]. This block diagram is used to show the components that will be used and how they are interconnected within the system. The system is designed based on the components shown in Block Diagram 1.1. The main components used include the Arduino Uno R4 WiFi, flame detector, ultrasonic sensor, red LED, blue LED, pump, buzzer, and LCD.

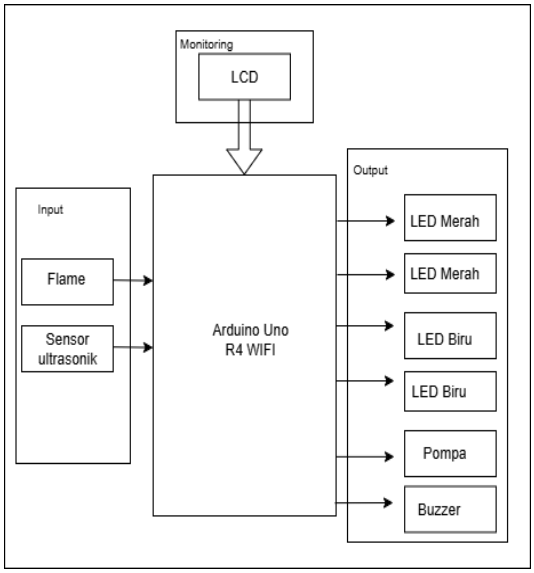

Fig. 1. Block Diagram System

The system detects the presence of fire. When a fire is detected, the water nozzle automatically opens and sprays water. In addition, the system is equipped with an ultrasonic sensor to detect the water level in the tank, and the monitoring results are displayed on the LCD, making supervision easier.

The following is an explanation of the block diagram for the design of the fire detection system:

1. Power Supply – Functions as the main power source that provides voltage and electric current to operate all system components.
2. Arduino Uno WiFi – Serves as the central controller (microcontroller) that processes data from the sensors and controls the output responses such as LEDs, buzzer, and pump, as well as sends information to Telegram in real time.
3. I2C Module – Used as a communication interface between the Arduino and the LCD to make pin usage more efficient and simplify data transmission to the display.
4. LCD – Displays system information such as fire detection status, object distance from the ultrasonic sensor, and pump condition.
5. Flame Detector – Detects the presence of fire based on the intensity of infrared light emitted by the flame.
6. Ultrasonic Sensor – Measures the water level in the storage tank.
7. Red LED – Acts as an indicator when fire is detected or when the water level is low.

Blue LED – Serves as an indicator that no fire is detected or that the condition is safe.

8. Pump (Actuator) – Functions to spray water when the system detects fire.
9. Buzzer – Serves as an audible alarm to provide a warning when fire is detected.
10. Telegram – Used to receive notifications or information sent by the Arduino.

As can be seen in Fig. 1 there is information about 3 parts that communicate with each other. The first part is the remote control block. There is Blynk IoT which functions as a controller and monitor carried out by the greenhouse owner and there is also Gmail which functions to receive sensor reading reports by the greenhouse owner and also functions to send messages that the system is in error to the greenhouse technician. The second part is the software block. There is Arduino IDE which functions to enter code into ESP32 and there is also Blynk Cloud which functions as a virtual communication intermediary between ESP32 and Blynk IoT and Gmail. The third part is the hardware block. There is ESP32 as the control center and main control system, there is a BH1750 sensor, DHT22 sensor, and soil moisture sensor, there is also a stepper motor actuator, lights, foggers, and water pumps.

B. Design System

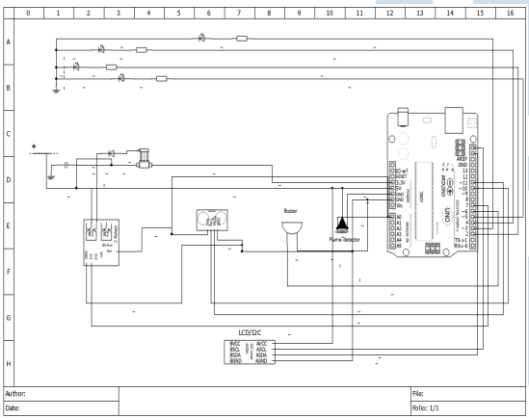

Fig. 2. Design System

The system design illustrates how the components are configured in the automatic fire detection system. This system uses an Arduino Uno as central control. The Arduino will control and process data from the sensors, then control the pump that will discharge water and display information in real time on the display. The system operation is as follows:

1. When the circuit is powered on, this is indicated by LED 1 (blue) and the display will show “Fire: Safe”.
2. When the fire sensor (KY-026) detects a flame, LED 2 (red) and the buzzer will activate, and the display will show “Fire: Danger”.
3. Then the 5 V DC pump is activated and pumps water from the tank to the predetermined fire point.
4. When the fire is extinguished, LED 2 (red) becomes inactive and the 5 V DC pump stops until it is activated again if another fire danger is detected.
5. LED 1 (blue) turns on again and the display returns to the indication “Fire: Safe”.
6. The ultrasonic sensor (HC-SR04) on the water tank functions as the water level reader.
7. The display shows two indications:
   a. Water tank: High / Normal / Low / Empty
   b. Water level: 0–100%

   Notes:
   • High: water > 80% – 100%
   • Normal: water > 40% – < 80%
   • Low: water < 40%
   • Empty: no water
8. If the tank level shows “Low” on the display, the pump will not activate and LED 2 (red) will light.

To build this design, several components are required, as listed in the following table.

TABLE I. LIST COMPONENT OF PROTOTYPING

No	Component	Quantity
1	Arduino Uno R4 WiFi	1
2	LCD + I2C Module	1
3	Flame Detector	1
4	UltrasoniC Sensor	1
5	Pump	1
6	Jumper Wires	± 30
7	Buzzer	1
8	Red LED	2
9	Blue LED	2

C. Flowchart

The following is an illustration of the system’s operation. In the flowchart above, there are two conditions. The first condition occurs when the sensor detects fire. In this case, the sensor sends a signal to the Arduino to activate the buzzer as an early warning of fire. The Arduino then turns on the pump, which draws water from the reservoir to extinguish the fire. At the same time, the red LED lights up to indicate that fire is still detected, while the blue LED turns off. Fire information is also displayed on the LCD. The second condition occurs when no fire is detected. In this situation, the buzzer is turned off, the red LED goes off, and the blue LED turns back on. The LCD then displays information indicating that no fire is detected.

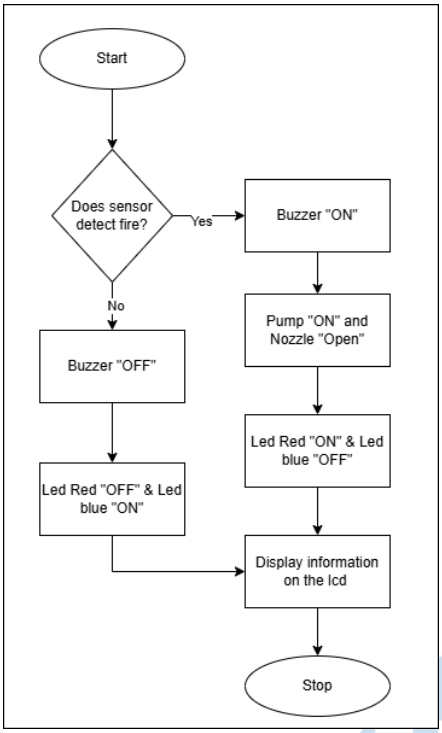

Fig. 3. Design System

III. Result and Analysis

In the system circuit, all components are shown working together to detect the presence of fire and automatically spray water as an initial fire suppression step.

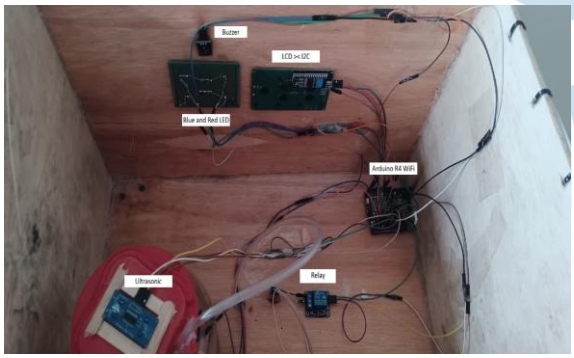

Fig. 4. Component System

Figure 4 shows the overall layout of the system inside the control box. Several main components can be seen, including the Arduino Uno R4 WiFi, flame sensor module, ultrasonic sensor, LCD, water pump, and the connecting cables between components.

The ultrasonic sensor is installed on the lid of the water tank to detect the water level or availability. The water pump is connected to the tank and functions to automatically draw and spray water when the system detects the presence of fire.

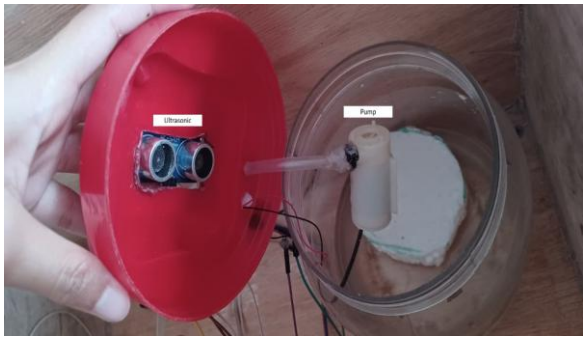

Fig. 5. Ultrasonic Sensor and Pump

From Figure 5 the ultrasonic sensor is installed at the top of the water container (tank). This sensor works by emitting ultrasonic waves and receiving their reflections from the water surface, allowing the Arduino to determine whether the water is still available or has run out. The system also includes a pump that functions to draw water automatically when a fire is detected.

Fig. 6. Flame Detector and Hose

At the bottom section, there is a hose and a flame detector. This part shows the hose end and the nozzle where water from the pump is discharged. It becomes active when the flame detector detects fire, allowing water to be sprayed directly onto the heat source area.

Fig. 7. LCD, LED, and Buzzer

It shows the front view of the system box, which includes an LCD screen, several LED indicators, and a buzzer.

Fig. 8. Display Telegram Bot

The following is the display of the Telegram bot, which shows information about water availability, pump status, and fire conditions in the automatic fire detection system. This bot sends notifications whenever there is a change in the system's state, such as the pump being activated or deactivated, fire being detected or not, and the water level in the storage tank.

TABLE II. FLAME DETECTOR TESTING

No	Test Experiment	Distance	Result	
			Yes	No
1	Yellow Bulb	± 95 cm	√	
		80 cm	√	
		70 cm	√	
		60 cm	√	
2	Phone Flashlight	15 cm		√
		10 cm		√
		5 cm		√
3	Virtual Fire	15 cm		√
		10 cm		√
		5 cm		√
4	Real Fire	35 cm	√	
		25 cm	√	
		20 cm	√	
5	Paraffin	50 cm		√
		40 cm		√
		30 cm		√
		25 cm		√
		10 cm		√

In the experimental results shown in Table 2, with the sensor sensitivity set to 33, it was found that the flame detector sensor exhibits different sensitivity levels to various light sources. In the first experiment using a yellow bulb, the sensor was able to detect light at a distance of up to approximately 95 cm and continued to detect it at closer distances (80 cm, 70 cm, and 60 cm). This indicates that the sensor is quite sensitive to yellow light because the intensity and spectrum of the bulb's light fall within the detectable range of the sensor.

In the second and third experiments, using a phone flashlight and virtual flame, the sensor failed to detect any light sources even at very close distances (5–15 cm). This occurs because the light emitted by a phone flashlight and a virtual flame (on a screen) does not contain the infrared components characteristic of real fire, resulting in no response from the sensor.

In the fourth experiment, using a real flame source, the sensor successfully detected fire up to a distance of 35 cm, indicating that the sensor effectively detects the infrared radiation emitted by actual flames. However, in the fifth experiment, the paraffin flame could not be detected even at a distance of 10 cm. This is because the infrared (IR) wavelength range that the flame sensor can detect is between 760 nm and 1,100 nm [5], while the infrared wavelength range of paraffin flame is between 2,500 nm and 25,000 nm [7][11].

IV. CONCLUSION

Based on the results of the design and testing, the automatic fire detection system using a flame detector based on Arduino Uno R4 WiFi was able to function properly as expected. The system can detect fire using the flame detector, and the water pump is automatically activated to extinguish the fire. Once the fire is extinguished, the water pump stops operating automatically. In addition to the flame sensor, the system is also equipped with an ultrasonic sensor installed on the water tank, which measures the water level and displays it in real time on the LCD, while also sending information to a Telegram bot, allowing users to monitor the system remotely.

The test results also show that the flame detector has high sensitivity to real fire and light bulb sources, even when the sensitivity level is reduced to 33. However, the flame detector is less responsive to virtual fire, phone flashlight, and paraffin flame, because the infrared wavelength of paraffin fire lies outside the IR wavelength range that can be detected by the flame detector.

Thus, this system has proven to be effective in detecting fire and providing automatic real-time notifications via Telegram, enabling users to respond quickly when there is a potential fire hazard.

REFERENCES

[1] G. A. Rimbawan and M. A. Nur, "Nilai Kerugian Ekonomi Lingkungan Akibat Kebakaran Hutan dan Lahan Gambut di Kota Banjarbaru," *JIEP: Jurnal Ilmu Ekonomi dan Pembangunan,* vol. 4, pp. 25-39, 2021. DOI: 10.20527/jiep.v4i1.3540

[2] PUSIKNAS (Pusat Informasi Kriminal Nasional)," 18 Oktober 2024. [Online]. Available: https://pusiknas.polri.go.id/detail_artikel/kebakaran_paling_banyak_terjadi_di_perumahan. [Accessed 15 Oktober 2025].

[3] D. A. Nugraha and B. Satria, "Prototype Alat Pendeteksi kebakaran Menggunakan Sensor Flame dan MQ-2 Berbasis Arduino Uno," *IJCS: Indonesian Journal of Computer Science,* vol. 11, pp. 936-944, 2022. DOI: https://doi.org/10.33022/ijcs.v11i3.3102

[4] D. Indriani, M. Subhan and E. Rahmawati, "Sistem Alarm Kebakaran Berbasis Arduino Menggunakan Flame Detector Dan Sensor MQ-2," *Jurnal Pedagogos : Jurnal Pendidikan STKIP Bima,* vol. 3, pp. 16-23, 2021. DOI: https://doi.org/10.33627/gg.v3i2.509

[5] Zulkifli, M. Muhallim, Hasnahwati, "Pengembangan Sistem Alarm dan Pemadaman Kebakaran Otomatis Menggunakan Internet of Things," JITET (Jurnal Informatika dan Teknik Elektro Terapan), vol. 13, no. 3, pp. 2444-2460, 2024. DOI: http://dx.doi.org/10.23960/jitet.v12i3.4774.

[6] J. Ryu and D. Kwak, "Flame Detection Using Appearance-Based Pre-Processing and Convolutional Neural Network," *MDPI,* no. Computing and Artificial Intellegence, pp. 1-14, 2021. DOI: https://doi.org/10.3390/app11115138

[7] "Pharmacopeial Forum," [Online]. Available: https://www.drugfuture.com/Pharmacopoeia/usp38/data/v38332/usp38nf33s2_c854.html. [Accessed 16 October 2025].

[8] S. F. Razi, A. Mardiyanto and S. Y. Widianti, "Implementasi Sistem Peringatan Dini Kebakaran Berbasis IoT (Internet of Things) Pada Gedung Sekolah Muhammadiyah Lhokseumawe," *Proceeding Seminar Nasional Politeknik Negeri Lhokseumawe,* vol. 8, pp. 110-115, 2025. URL: https://e-jurnal.pnl.ac.id/semnaspnl/article/view/6897/4765

[9] D. R. Juliandi, J. Karman and R. , "Perancangan Sistem Bot Alert Telegram Sebagai Notifikasi Deteksi Serangan Ping of Death Berbasis Snort," *RESOLUSI : Rekayasa Teknik Informatika dan Informasi,* vol. 5, pp. 49-57, 2024. DOI: 10.30865/resolusi.v5i1.2168

[10] M. H. Azhari, R. and B. A. Prakosa, "Rancang Bangun Dan Pemanfaatan Notifikasi Telegram Pada Alat Penyewaan Power Bank," *Jurnal Pendidikan dan Teknologi Indonesia (JPTI),* vol. 4, pp. 313-324, 2024. DOI: https://doi.org/10.52436/1.jpti.450

[11] A. Y. Ramadhan, "Rancang Bangun Simulasi Otomatisasi Pembersih Sightglass Untuk Meningkatkan Akurasi Flame Detector Pada Burner Heater", Politeknik Industri Petrokimia Banten, 2025.

[12] R. T. Aldisa, F. N. Karel and M. Aldinugroho, "Sistem Peringatan Dini Kebakaran Dengan Flame Sensor dan Arduino Uno R3," *JURNAL MEDIA INFORMATIKA BUDIDARMA,* vol. 6, no. 1, pp. 453-458, 2022. DOI: 10.30865/mib.v6i1.3499

[13] V. Haristianti, M. . A. W. Linggasani, S. N. Sabatini and D. Hartabela, "PROTEKSI RISIKO KEBAKARAN DI PERUMAHAN STUDI KASUS: PERUMAHAN BARU DI KELURAHAN CIGADUNG, BANDUNG," *Jurnal Arsitektur Zonasi,* vol. 2, no. 1, pp. 1-11, 2019. DOI: http://10.17509/jaz.v2i1.15061

[14] A. Cahyadi, F. Lestari and A. Kadir, "ANALISIS TINGKAT RISIKO BENCANA KEBAKARAN WILAYAH JAKARTA BARAT, PROVINSI DKI JAKARTA," *PREPOTIF Jurnal Kesehatan Masyarakat,* vol. 6, no. 1, pp. 467-477, 2022. DOI: https://doi.org/10.31004/prepotif.v6i1.3651

[15] F. Maulana, M. Orisa and H. Z. Zahro, "KLASIFIKASI DATA PRODUK MEBEL ANEKA JAYA MENGGUNAKAN METODE K-NEAREST NEIGHBOR BERBASIS WEB," *JATI (Jurnal Mahasiswa Teknik Informatika),* vol. 5, no. 2, pp. 460-466, 2021. DOI: https://doi.org/10.36040/jati.v5i2.3782

[16] R. Shi and D. Vaikuntan, "Recent Advances in Flame Detection Using Convolutional Neural Networks: A Review," *Journal of Computer Technology and Software,* vol. 4, no. 1, 2025. DOI: https://doi.org/10.5281/zenodo.14785303.

ISSN 2355-3286

Convolutional Neural Network Roasted Coffee Bean Classification Based on Color

Natanael Michael Hanes[1], Endah Setyaningsih[2], Meirista Wulandari[3]
[1,2,3] Department of Electrical Engineering, Universitas Tarumanagara, Jakarta Barat, Indonesia
natanael.525210018@stu.untar.ac.id[1], endahs@ft.untar.ac.id[2], meiristaw@ft.untar.ac.id[3]

Accepted on August 04, 2025
Approved on November 18, 2025

***Abstract*— Coffee quality is significantly influenced by the roasting level, which is typically determined by observing the color of the beans. This color-based classification has traditionally been performed through manual sorting and human judgment. However, such methods are labor-intensive, time-consuming, subjective, and prone to inconsistencies or human error. These challenges highlight the need for a more reliable and automated solution to improve the accuracy and efficiency of coffee bean classification. In response, this project introduces an automated classification system based on deep learning, specifically utilizing Convolutional Neural Networks (CNNs). CNNs are particularly well-suited for image classification tasks, as they can automatically learn and extract relevant visual features such as color, texture, and shape. This allows the system to classify coffee beans into different roast levels with minimal human intervention. The proposed system is evaluated using several performance metrics, including accuracy, precision, recall, and F1 score. Experiments are conducted using various input image resolutions, and the results show that the CNN model achieves its best performance with 64×64 pixel images, obtaining an accuracy of 99%, which surpasses other tested resolutions such as 32×32 with an accuracy of 98%) and 128×128 with an accuracy of 98.6%). When compared to deeper architectures like ResNet50, which achieved 96.49% accuracy at 224×224 pixels. This demonstrates not only the model's effectiveness in correctly identifying roast levels but also its efficiency in working with lower-resolution images, making it practical for real-time applications or deployment in resource-constrained environments.**

***Index Terms*—Coffee Bean Classification; Convolutional Neural Network; LCD**

I. INTRODUCTION

Among the most popular beverages in the world, coffee's flavor and quality are significantly impacted by the caliber of the coffee beans used. Coffee's flavor is its most crucial component, and roasting has the biggest effect on it [1]. The most popular method of determining the roasting level is to look at the color of the coffee beans. Light color denotes a high acidity and low roasting level, medium color denotes a medium roasting level and balanced acidity, and dark color denotes a high roasting level and bitter flavor [2]. This process is laborious, capricious, and prone to human mistake because it always depends on human judgment and manual sorting [3]. The advent of modern technology, particularly computer vision and deep learning techniques [4], has raised interest in automating and increasing the accuracy of coffee bean classification. One area of machine learning called deep learning has demonstrated remarkable results in tasks involving picture recognition and classification.

Recent studies on classification tasks in food and agriculture have demonstrated advances with deep learning models. Convolutional Neural Networks (CNN) are a well-liked deep learning technique for classification jobs. A variety of fruits, cereals, and plants have been successfully categorized using CNN algorithms based on visual attributes[5]. The classification of coffee bean variations, which vary in size, shape, color, and texture, greatly benefits from these models' capacity to extract intricate patterns from photos. Large annotated datasets of coffee bean photos can be used to train deep learning models to accurately identify and categorize coffee beans. This lessens the need for manual effort and increases consistency in quality evaluation. CNN has an accuracy of more than 90% in classifying coffee beans according to their quality and place of origin [6].

The application of deep learning to the classification of coffee beans is consistent with the larger movement in the food and beverage sector to incorporate Artificial Intelligence (AI). AI-powered solutions are being utilized more and more to enhance supply chains, meet consumer needs for sustainability and transparency, and increase product quality. A coffee bean classification system that is automated and based on color may support importers and producers maintain a uniform product look, which is frequently linked to customer preference and quality. Coffee bean maturity, roasting levels, and processing methods are some of the elements that might create variations in coffee bean color profiles, which can be identified by deep learning models [7].

The application of deep learning for classifying coffee beans presents challenges. The requirement for large and high-quality datasets to properly train models is one of the main obstacles. Many resources are needed to collect and annotate such datasets, especially for small-scale coffee farmers. In addition, the classification procedure may become more difficult due to variations in coffee bean appearance caused by factors such as roasting levels and regional differences. Recent developments in transfer learning and data

augmentation techniques have shown promising results in addressing these issues [8].

Multiple steps are involved in developing a deep learning model to categorize coffee beans according to color, where processing methods, bean origin, and roasting level all affect color variance [9],[10]. Four different roasting levels were used for the coffee beans used in this study at JJ Mall Jatujak's "Bona Coffee." The Laos Typica Bolaven (Coffea arabica) beans were first green or unroasted before being roasted at the light roast level, followed by Doi Chaang (Coffea arabica) at the medium roast level, and Brazil Cerrado (Coffea arabica) at the dark roast level [11]. When CNN processing techniques are used properly, they significantly improve coffee bean categorization accuracy and allow for a more automated and reliable procedure.

The objective of this design is to develop an image classification system for coffee beans using a (CNN) model as the main processing module. In order to recognize and categorize coffee beans into groups such as green, light, medium, and dark, the CNN processes the input photos to the system. CNN is capable of automatically and reliably classify coffee beans according to their roast levels when processing them using the right methods.

II. Literature Review

The effectiveness of the different approaches has been compared by reviewing a few papers on the use of deep learning in coffee bean classification. “Classification Model of 'Toraja' Arabica Coffee Fruit Ripeness Levels Using Convolution Neural Network Approach” is one paper on coffee bean classification [12]. Coffee beans in this paper are categorized as raw, overripe, fully ripe, and half-ripe. The CNN architecture for image analysis and a computer as the primary processor were used in its development. To increase system accuracy in differentiating each ripeness categorization, a dataset of coffee bean photos taken from different perspectives and lighting conditions was used to train the CNN model. Pre-processing steps such as colour normalization, contrast enhancement, and data augmentation are used to increase the diversity of training samples before the classification process starts. Once the photos of coffee beans have gone through a number of convolutional and pooling layers, CNN extracts important information and classifies the beans' maturity based on the visual patterns it has identified.

Coffee beans are categorized based on shape in according to their morphologies: premium, peaberry, long berry, and deformed shapes [13]. It was created with CNN for image analysis and a computer as the primary processor. To make sure the CNN model could accurately identify shape changes, it was trained on a dataset of coffee bean photos from multiple sources. The process begins with image pre-processing, such as normalization, contrast enhancement, and data augmentation to improve model generalization. The CNN model classified the coffee bean images into four predefined shape categories after extracting the key characteristics from the images after going through multiple convolutional and pooling layers. The classification results are displayed in the form of accuracy values, which serve as indicators of the system’s reliability in recognizing coffee bean shapes automatically.

Indonesian coffee beans have been classified originating from Gayo Aceh, Kintamani Bali, and Toraja Tongkonan [14]. It was developed utilizing a computer as the main processor and implemented a CNN architecture based on AlexNet for image classification. The CNN model was trained using a dataset of coffee bean images from the three regions, covering various lighting variations and perspectives to improve model performance. The image pre-processing stage was performed before classification, including color normalization, contrast enhancement, and data augmentation to optimize input quality. After going through several convolutional and pooling layers, the AlexNet model automatically extracted unique visual features from the coffee beans and classified them into one of the three available categories. The final result was a classification accuracy value, which serves as the primary indicator for evaluating the model’s reliability in identifying the origin of coffee beans with high precision.

III. Research Method

In order to identify coffee beans according to four roasting levels (light, medium, medium-dark, and dark), a CNN model that assesses various input image sizes was examined for this paper. The CNN model is developed, and the classification operation is obtained by simulation in Python programming language. An Intel(R) Core (TM) i7-8700 CPU running at 3.20 GHz was used for the simulations in order to execute programs and process images. This paper simulates varying input image sizes to determine the optimal configuration for achieving high accuracy in coffee bean categorization.

In order to create the CNN model, four distinct input image sizes consist of 32 × 32 pixels, 64 × 64 pixels, 128 × 128 pixels, and 224 × 224 pixels. The accuracy and loss metrics of the two models will be compared. The CNN model that has the highest accuracy and the lowest loss is selected for further evaluation. The block diagram of this research method is shown at Fig 1.

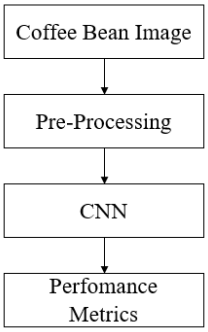

Fig. 1. Block Diagram

A. *Coffee Bean Image*

Four different roasting levels of coffee beans were used at "Bona Coffee," located in JJ Mall Jatujak. The coffee beans are Laos Typica Bolaven (Coffea arabica), which are mildly roasted and are known as green or unroasted coffee[11]. Brazil Cerrado (Coffea arabica) is dark roasted, and Doi Chaang (Coffea arabica) is medium roasted. The coffee bean images were taken using an iPhone 12 Mini with a 12-megapixel rear camera that has both Ultra-wide and WideCamera settings. During image collection, the camera was oriented parallel to the plane of the object. Images of roasted coffee beans were captured in a variety of settings to guarantee a range of image inputs. Each coffee bean variety was placed in a container to improve image noise, and the dataset was gathered using both natural light and LED light from a light box. Images were automatically taken and stored in PNG format. The coffee bean images were carefully labelled by professionals who were knowledgeable about coffee roasting stages. Light, green, medium, and dark were the four roast levels into which each photograph was assigned based on the beans' surface properties and visual hue. The size of each coffee bean image is 3024 × 3032 pixels. Each of the four roasting stages is represented by 1200 of the dataset's 4800 total images. The images used in this paper has been resized from 3024 × 3032 pixels into four different image sizes, such as, 32 × 32 pixels, 64 × 64 pixels, 128 × 128 pixels, and 224 × 224 pixels.

Fig 2 presents an unaltered coffee bean image from the Dark label in the dataset with a resolution of 3024 × 3032, alongside its resized version at 224 × 224 pixels.This transformation demonstrates how high-resolution images were standardized for model input while maintaining key visual features such as texture and color, which are essential for roast-level classification. Fig 3 shows an unaltered and resized coffee bean image from the Green label. The resizing process ensures consistency across all samples, allowing the model to effectively learn relevant color and surface characteristics without excessive computational cost. Fig 4 depicts an unaltered and resized coffee bean image from the Light label in the dataset. The comparison highlights that even after resizing, the key differences in hue and surface brightness, important indicators of roast intensity, remain visually distinguishable. Fig 5 displays an unaltered and resized coffee bean image from the Medium label. This figure illustrates that the preprocessing step successfully preserves visual cues necessary for accurate CNN-based classification, despite the significant reduction in image resolution.

Fig. 2. Unaltered Coffee Bean Image from the Dark Label in the Dataset in 3024x3032 and Resized Coffee Bean Image from the Dark Label in the Dataset in 224x224

Fig. 3. Unaltered Coffee Bean Image from the Green Label in the Dataset in 3024x3032 and Resized Coffee Bean Image from the Green Label in the Dataset in 224x224

Fig. 4. Unaltered Coffee Bean Image from the Light Label in the Dataset in 3024x3032 and Resized Coffee Bean Image from the Light Label in the Dataset in 224x224

Fig. 5. Unaltered Coffee Bean Image from the Medium Label in the Dataset in 3024x3032 and Resized Coffee Bean Image from the Medium Label in the Dataset in 224x224

B. *Convlutional Neural Network (CNN)*

CNN is a deep learning neural network that can resolve challenging visual issues. Numerous applications, including object detection, video processing, and picture classification, make extensive use of this technique [15]. A sequential architectural model with multiple convolutional, pooling, and fully connected layers is used.

The first layer is Conv2D, which generates an output of size (222, 222, 32) with 896 parameters and 32 3x3 filters with default padding set to "valid." After that, the output is down sampled to (111, 111, 32) using a MaxPooling2D layer with a 2×2 kernel size. With 64 filters, the second layer is another Conv2D, producing an output of (109, 109, 64) and 18,496 parameters. A second MaxPooling2D layer then decreases the dimensions to (54, 54, 64). Following the output of the third convolutional layer, which has 128 filters and 73,856 parameters, the feature map is reduced to (26, 26, 128) using MaxPooling2D. The CNN Architecture can be seen in Fig 6.

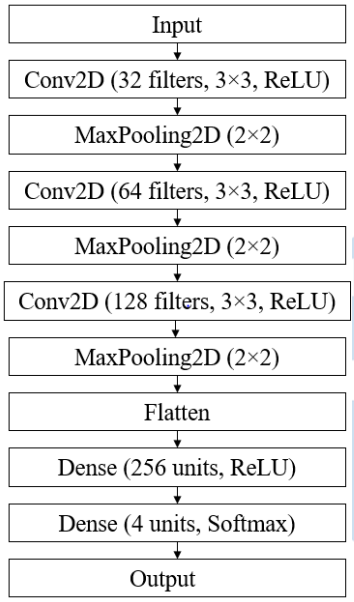

Fig. 6. Proposed CNN Architecture

C. *Performance Metrics*

The parameters used to evaluate a deep learning algorithm's performance are called performance metrics. These measurements include precision, recall, and F1 score. The ratio of correctly predicted positive observations to all expected positive observations is known as precision. The ratio of correctly predicted positive observations to all actual positive observations is known as recall [16]. The F1 score, defined as a calculated average of precision and recall, is a balanced measure of a model's accuracy, especially when dealing with unbalanced datasets.

A contingency table called a confusion matrix is used to show how well a classification model performs in both binary and multi-class scenarios. The true positives (TP), true negatives (TN), false negatives (FN), and false positives (FP) for each class are displayed in this matrix by comparing the actual labels (rows) with the predicted labels (columns). Researchers can compute other evaluation metrics like accuracy, precision, recall, and F1-score using this visual representation, in addition to directly observing which classes the model frequently misclassifies [17].

IV. RESULTS

Analysis of the proposed CNN performance compared to ResNet 50 architecture showing the CNN accuracy value can be seen in TABLE I, confusion matrix results of input size 224×224 can be seen at Fig 8; confusion matrix results of input size 128×124 can be seen at Fig 9; confusion matrix results of input size 64×64 can be seen at Fig 10; and confusion matrix results of input size 32×32 can be seen at Fig 11; The suggested CNN model and the ResNet-50 architecture perform noticeably differently in terms of classification accuracy when compared across a range of input image sizes.

The suggested CNN outperformed ResNet-50 with an accuracy of 98.87% at the standard input size of 224×224 pixels, surpassing its 96.49% accuracy. The accuracy of the suggested model remained high at 98.62% when the input size was decreased to 128×128 pixels, whereas ResNet-50's accuracy decreased to 94.12%. Interestingly, ResNet-50 scored 92.87%, whereas the proposed CNN's best accuracy of 99% was observed at 64×64 pixels, demonstrating its resilience to lower-resolution inputs. ResNet-50's accuracy dropped significantly to 78.62% at the smallest input size of 32×32 pixels, but the suggested CNN exhibited a modest decline to 98%. The accuracy graph as ashown in Fig 7 makes it evident that the proposed CNN model does not overfit. By the tenth epoch, the training accuracy (blue line) and validation accuracy (orange line) have both converged close to 1.0 (99–100%) after increasing gradually throughout the first few epochs. The training procedure shows no discernible difference between the two curves, which follow a similar trajectory. This close alignment suggests that the model has acquired generalizable characteristics rather than simply memorizing the training data, as it shows consistent performance on both training and validation datasets. Further supporting the lack of overfitting is the validation accuracy, which shows no signs of declining after peaking.

TABLE I. ACCURACY RESULTS

Input Size	***ResNet 50[18]***	***Proposed CNN***
224×224	96,49%	98,87%
128×128	94,12%	98,62%
64×64	92,87%	99%
32×32	78,62%	98%

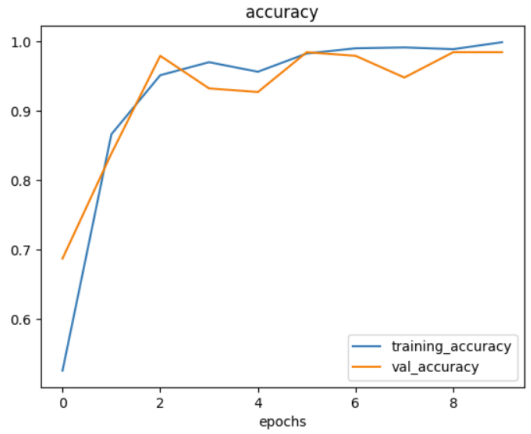

Fig. 7. Training and Validation Accuracy of the Proposed Model

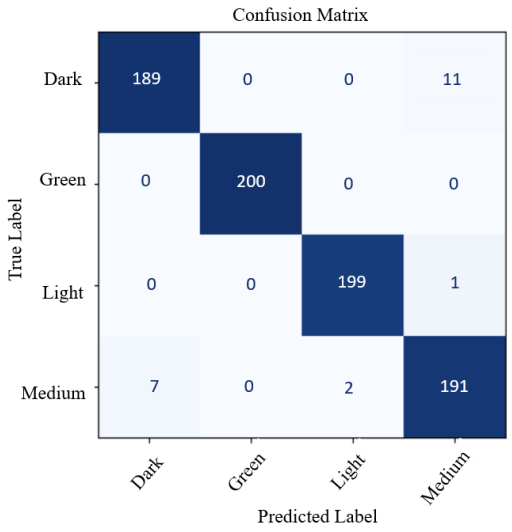

Fig. 8. Confusion Matrix Results of Proposed CNN using 224x224 input

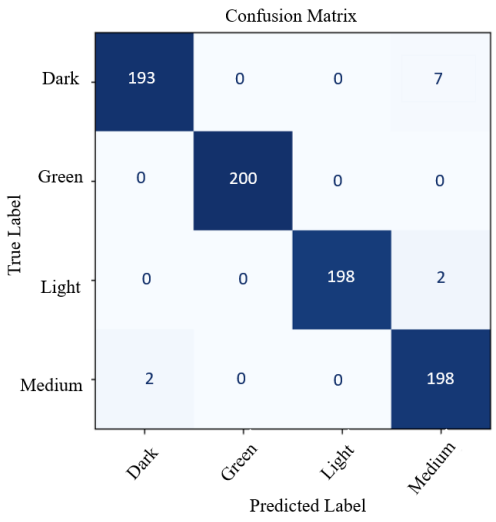

Fig. 9. Confusion Matrix Results of Proposed CNN using 128x128 input

As shown in Fig 8, the model performs accurately but shows some misclassification, particularly between dark and medium roasts (11 instances), indicating that increased resolution does not always improve class separation. In contrast, the model achieves better results with 128×128 input as shown with Fig 9, where misclassifications decrease as dark vs. medium errors drop to 7, and other classes remain highly accurate.

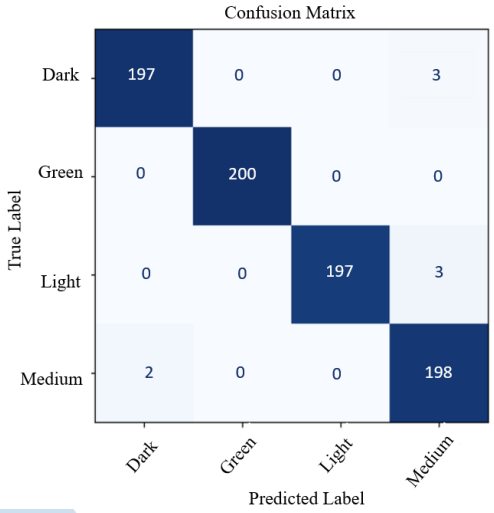

Fig. 10. Confusion Matrix Results of Proposed CNN using 64x64 input

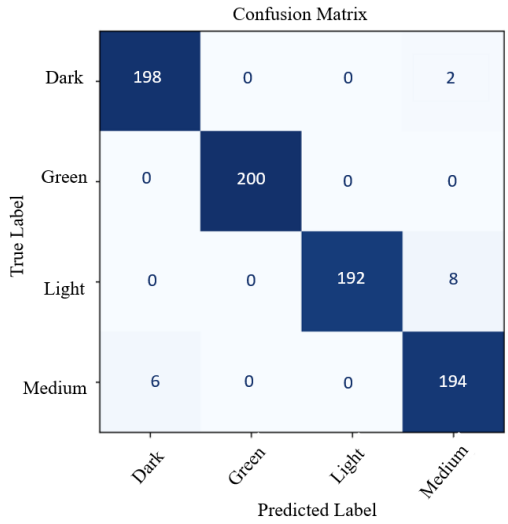

Fig. 11. Confusion Matrix Results of Proposed CNN using 32x32 input

The best performance is observed at 64×64 input as shown with Fig 10, where the model reaches 99% accuracy with only a few errors with just 3 dark roast beans misclassified as medium, and 3 light roasts also predicted as medium. At the lowest input size of 32×32 as shown with Fig 11, the model still performs strongly but shows a slight increase in confusion between visually similar classes such as light and medium, with 8 misclassified samples, and 6 medium roasts mislabeled as dark. These results collectively highlight that the 64×64 input offers the most balanced performance, with high accuracy and minimal

misclassification, making it an ideal resolution for efficient and reliable coffee bean classification.

TABLE II. PRECISION, RECALL, F1-SCORE, SUPPORT RESULTS OF 64X64 INPUT

Label	*Precicion*	*Recall*	*F1-score*	*Support*
Dark	0.99	0.98	0.99	200
Green	1.00	1.00	1.00	200
Light	1.00	0.98	0.99	200
Medium	0.97	0.99	0.98	200

Table II presents the precision, recall, F1-score, and support results for the CNN model using a 64×64 input image size. Precision, recall, and F1-scores range from 0.97 to 1.00, indicating consistently high performance across all coffee roast levels. The model can reliably and consistently identify unroasted beans without misclassification, as shown by the Green class's accurate outcomes (precision, recall, and F1-score = 1.00). With F1-scores of 0.99, the Light and Dark roast levels also performed almost flawlessly, demonstrating the model's excellent capacity to discern minute variations in roast color and texture. The F1-score (0.98) and precision (0.97) of the Medium class were marginally lower but still very high, indicating slight feature overlaps between the medium and adjacent roast levels.

V. CONCLUSION

The proposed CNN model demonstrates its best performance at an input size of 64×64 pixels, achieving the highest accuracy of 99%. At this resolution, the confusion matrix indicates minimal misclassifications across all coffee roasting levels, suggesting the model's strong ability to distinguish between different categories even with relatively low image quality. This result highlights the model's efficiency, as it maintains excellent classification performance without the need for high-resolution inputs.

Compared to larger input sizes like 224×224, where accuracy slightly decreases and misclassifications increase especially between similar roast levels the 64×64 input provides an optimal balance between accuracy and computational efficiency, making it highly suitable for practical applications in coffee bean classification.

The paper makes a significant contribution in comparison to previous studies, in addition to these numerical results. Many earlier works on coffee bean classification used complicated designs like ResNet50 or VGG16, which demand greater processing power and longer training times, as well as high-resolution photos. Alternatively, the suggested CNN model achieves similar or even better accuracy using a simpler architecture and inputs with much lower resolution. The key markers of roast intensity, color and texture, can be effectively extracted using feature extraction without the need for deep or computationally costly networks. In just 10 epochs, the model achieves the required accuracy, demonstrating its quick convergence and effectiveness during training. Additionally, it is evident that the model does not display overfitting because the training and validation accuracy curves closely overlap.

Beyond technical performance, both coffee farmers and consumers can benefit from these results in the real world. The use of a CNN-based classification system by manufacturers can drastically cut down on the need for manual sorting, lowering labor expenses and human error while ensuring constant product quality throughout large-scale manufacturing. In addition to enabling faster turnaround times and more impartial grading standards, automated classification can help speed up the quality control procedure. As roast levels have a direct impact on flavor, aroma, and the overall coffee experience, this translates into increased consumer confidence in product consistency. The suggested approach promotes a more effective and transparent coffee supply chain, which is advantageous to all parties involved, from growers to consumers.

The study does, however, have a number of shortcomings that may be resolved in subsequent research. The model performs well under controlled imaging conditions, which include constant background, camera distance, and lighting. Such variances could impact the model's accuracy in actual industrial settings. It's also probable that not all potential coffee bean varietals, flaws, or environmental factors were covered by the dataset. Future research should broaden the dataset to encompass a variety of coffee varieties and take pictures in various settings to increase the model's resilience. Future studies could also look into deploying the model on embedded or mobile systems for real-time, on-site coffee quality assessment and using explainable AI (XAI) tools to interpret classification results.

ACKNOWLEDGEMENT

The authors would like to express their sincere gratitude to LPPM Universitas Tarumanegara for the support provided through the completion of this paper.

REFERENCES

[1] D. Buonocore, M. Carratu, and M. Lamberti, "Classification of coffee bean varieties based on a deep learning approach," in *18th IMEKO TC10 Conference "Measurement for Diagnostics, Optimization and Control to Support Sustainability and Resilience" Warsaw, Poland*, 2022.

[2] P. Bahrumi, R. Ratna, and R. Fadhil, "Levelisasi penyangraian kopi: suatu kajian," *Jurnal Ilmiah Mahasiswa Pertanian*, vol. 7, no. 1, pp. 522–525, 2022.

[3] N. O. Adiwijaya, H. I. Romadhon, J. A. Putra, and D. P. Kuswanto, "The quality of coffee bean classification system based on color by using k-nearest neighbor method," in *Journal of Physics: Conference Series*, IOP Publishing, 2022, p. 012034.

[4] D. S. Leme, S. A. da Silva, B. H. G. Barbosa, F. M. Borém, and R. G. F. A. Pereira, "Recognition of coffee roasting degree using a computer vision system," *Comput Electron Agric*, vol. 156, pp. 312–317, 2019.

[5] F. Yu *et al.*, "Progress in the application of cnn-based image classification and recognition in whole crop growth cycles," *Remote Sens (Basel)*, vol. 15, no. 12, p. 2988, 2023.
[6] E. Hassan, "Enhancing coffee bean classification: a comparative analysis of pre-trained deep learning models," *Neural Comput Appl*, vol. 36, no. 16, pp. 9023–9052, 2024.
[7] D. H. Suryana and W. K. Raharja, "Applying artificial intelligence to classify the maturity level of coffee beans during roasting," *Int J Eng Sci Inf Technol*, vol. 3, no. 2, pp. 97–105, 2023.
[8] C. C. Enriquez, J. Marcelo, D. R. Verula, and N. J. Casildo, "Leveraging deep learning for coffee bean grading: A comparative analysis of convolutional neural network models," *2024. Transactions on Science and Technology*, vol. 11, no. 1, pp. 1–6, 2024.
[9] J. N. C. Sarino, M. M. Bayas, E. R. Arboleda, E. C. Guevarra, and R. M. Dellosa, "Classification of coffee bean degree of roast using image processing and neural network," *Int. J. Sci. Technol. Res*, vol. 8, no. 10, pp. 3231–3233, 2019.
[10] W. Manosroi, A. Phromfaiy, and W. Janthong, "Classification of Coffee Beans Color Level during Roasting by Feed Forward Back Propagation Neural Network," *The Journal of King Mongkut's University of Technology North Bangkok*, vol. 34, Sep. 2022, doi: 10.14416/j.kmutnb.2022.09.006.
[11] S. Ontoum, T. Khemanantakul, P. Sroison, T. Triyason, and B. Watanapa, "Coffee roast intelligence," *arXiv preprint arXiv:2206.01841*, 2022.
[12] A. Michael and M. Garonga, "Classification model of 'Toraja'arabica coffee fruit ripeness levels using convolution neural network approach," *ILKOM J. Ilm*, vol. 13, pp. 226–234, 2021.
[13] P. F. I. R. H. Zer and R. Rosnelly, "Classification of Shape Bean Coffee Using Convolutional Neural Network," in *Proceeding International Conference on Information Science and Technology Innovation*, 2023, pp. 6–10.
[14] Y. Hendrawan *et al.*, "AlexNet convolutional neural network to classify the types of Indonesian coffee beans," in *IOP Conference Series: Earth and Environmental Science*, IOP Publishing, 2021, p. 012059.
[15] P. Purwono, A. Ma'arif, W. Rahmaniar, H. I. K. Fathurrahman, A. Z. K. Frisky, and Q. M. ul Haq, "Understanding of convolutional neural network (cnn): A review," *International Journal of Robotics and Control Systems*, vol. 2, no. 4, pp. 739–748, 2022.
[16] Z. Haimeed, M. Amir, and M. J. Applied Sciences, "Comprehensive Image Classification using Hybrid CNN-LSTM Model with Advanced Feature Extraction on Coco Dataset," Oct. 2024.
[17] J. Görtler *et al.*, "Neo: Generalizing Confusion Matrix Visualization to Hierarchical and Multi-Output Labels," in *Conference on Human Factors in Computing Systems - Proceedings*, Association for Computing Machinery, Apr. 2022. doi: 10.1145/3491102.3501823.
[18] B. Koonce, "ResNet 50," 2021, pp. 63–72. doi: 10.1007/978-1-4842-6168-2_6.

ISSN 2355-3286

Implementation of Trajectory Tracking on Mobile Robot Differential Drive

Imam Taufiqurrahman[1], Eko Sujarwanto[2], Andri Ulus Rahayu[3],
Mira Riski Aldiani[4], Sayyid Qhutub Abdul Hakim[5]
[1,3,4,5] Faculty of Engineering, Siliwangi University, Tasikmalaya, Indonesia
[2] Physics Education, Universitas Siliwangi, Tasikmalaya, Indonesia.
[1]imamtaufiqurrahman@unsil.ac.id

Accepted on October 02, 2025
Approved on December 28, 2025

***Abstract*—This study discusses the implementation of trajectory tracking on a differential drive mobile robot using the odometry method. The system was designed by utilizing rotary encoders to estimate the robot's position and a proportional controller to regulate movement toward the target point. The research employs an Arduino microcontroller as the processing unit, integrated with L298N motor drivers and DC motors to achieve autonomous navigation capabilities. Experiments were carried out on multi-point trajectories, namely three-way and four-way paths, under two different surface conditions: flat and textured fields. Each trajectory was analyzed through systematic measurement of Mean Absolute Trajectory Error (MATE) to quantify the accuracy of the tracking system. The proportional control constant (Kp) was determined through iterative testing, with Kp=4 identified as the optimal value that enables the robot to reach target coordinates while maintaining velocity stability. The results showed that the robot was able to follow the predetermined path with a relatively high level of accuracy, especially on flat surfaces, achieving a MATE of 0.0661 for three-point trajectories and 0.0561 for four-point trajectories. However, on textured paths, the accuracy decreased significantly, with MATE values increasing to 0.2065 and 0.2778 respectively, due to wheel slip and disturbances in encoder readings. PWM analysis revealed that textured surfaces required 15-23% higher power consumption and resulted in substantial signal fluctuations (±25-35 PWM units) compared to flat surfaces (±10-15 PWM units). The comparison between both conditions emphasizes that surface characteristics have a significant influence on the performance of odometry-based trajectory tracking. This research contributes to the understanding of environmental factors affecting autonomous mobile robot navigation and provides practical insights for implementing trajectory tracking systems in real-world applications where surface conditions may vary.**

Index Terms — Mobile robot, differential drive, odometry, trajectory tracking, proportional control

I. INTRODUCTION

Mobile robots are a type of autonomous system designed to move independently across floors or specific pathways through the use of wheel actuators and motion control algorithms [1]. Among various types of wheeled robots, the differential drive mobile robot is one of the most widely adopted configurations due to its simple mechanical structure, high maneuverability, and ease of control. This robot operates using two independently driven wheels located on the right and left sides, allowing it to move forward, backward, turn, and even rotate in place through variations in the rotational speed of each wheel. Such flexibility makes differential drive robots suitable for numerous applications in industry, logistics, exploration, and service robotics, where precise movement and adaptability are crucial requirements [2][3][4].

The capability of a mobile robot to follow a predetermined path with high precision is a fundamental aspect of autonomous navigation systems [5]. This ability, known as trajectory tracking, involves guiding the robot's movement along a defined route or toward a sequence of target coordinates while continuously minimizing position and orientation errors. Trajectory tracking plays a key role in many robotic applications, including automated material transport, warehouse management, and mapping or surveillance tasks, where accuracy and reliability of motion strongly influence overall performance [6][7].

To achieve accurate trajectory tracking, one essential element is the robot's position estimation method. A widely used technique for this purpose is odometry, which estimates the robot's relative position by calculating the displacement of its wheels using rotary encoder data [8]. Odometry provides a simple yet effective way to track motion in real time without relying on external sensors. The distance traveled by each wheel is calculated based on encoder pulses, which are then converted into translational and rotational movements of the robot through differential kinematic equations [9]. However, despite its practicality, odometry is sensitive to cumulative errors, particularly when wheel slip, surface irregularities, or mechanical misalignments occur during motion.

In order to compensate for these errors and maintain accurate motion toward the target trajectory, a suitable control strategy must be implemented. One of the most fundamental and widely used approaches is the Proportional (P) control method, which adjusts the robot's motor speed proportionally to the detected error

between the desired trajectory and the actual position [10]. Although relatively simple, proportional control can produce a stable and responsive movement when properly tuned, especially for low-speed navigation tasks and short-range path following [11][12]. The tuning of the proportional gain directly affects the system's responsiveness and stability—values that are too small cause sluggish motion, while excessively high values can induce oscillations and instability [13].

Environmental and surface conditions also play a critical role in determining the performance of odometry-based trajectory tracking [14]. When operating on flat, untextured surfaces, wheel movement tends to be uniform, resulting in precise encoder readings and accurate position estimation. Conversely, on rough or textured surfaces, wheel slip and vibration introduce disturbances that cause deviations in encoder feedback, leading to cumulative position and orientation errors [15][16]. These factors highlight the importance of evaluating robot performance under different physical conditions to understand how terrain characteristics influence tracking accuracy and control response.

Based on these considerations, this study aims to implement and evaluate an odometry-based trajectory tracking system on a differential drive mobile robot using proportional control. The research focuses on comparing the robot's movement accuracy across two surface conditions—flat (untextured) and rough (textured)—to analyze how terrain characteristics affect odometry readings and trajectory stability. Experiments were conducted using multi-point paths, specifically three-point and four-point trajectories, to observe variations in tracking accuracy and system response. Through these analyses, this study seeks to provide insights into the practical limitations of odometry in real-world environments and offer references for improving trajectory tracking performance in future mobile robot applications.

II. METHODOLOGY

In this study, a differential drive mobile robot was designed using an Arduino microcontroller as the main processing unit to implement an odometry-based trajectory tracking system. Figure 1 illustrates the overall research flowchart, presenting the systematic workflow starting from literature review, system design, component integration, and experimental testing. This flowchart provides a clear visualization of how the trajectory tracking system is developed, implemented, and validated throughout the study.

To evaluate the influence of environmental conditions on tracking performance, the experiments were conducted under two different surface conditions, namely untextured and textured surfaces. The untextured surface consists of a flat and smoothly sanded wooden board, providing uniform wheel–ground contact and minimal friction disturbance. In contrast, the textured surface is constructed from textured concrete wall material with irregular roughness, resulting in non-uniform friction and increased wheel–ground interaction variability. This textured condition introduces intermittent wheel slip and mechanical vibrations during robot motion, which directly affect encoder readings and odometry accuracy. The selection of these two surface types enables a controlled comparison of trajectory tracking performance under ideal and non-ideal traction conditions.

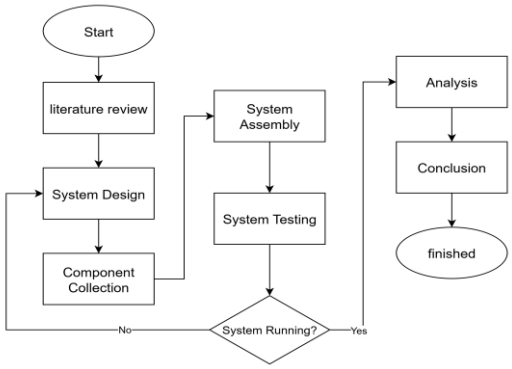

Fig. 1. System workflow

A. Literature Review

The research began with a literature study, system design, component collection, system assembly, and system testing. If the system testing met the desired targets, it proceeded to analysis, conclusion, and completion. However, if the system testing did not meet the expected targets, the process returned to system planning and retesting. This process was repeated until the target objectives were achieved, and then it was completed.

B. System Design

The wiring diagram in this study shows the integration of the main components of an Arduino-based mobile robot system. The hardware integration of the differential-drive mobile robot is shown in Figure 2, which presents the complete circuit diagram of the system. The diagram illustrates the connection between the Arduino microcontroller, motor driver, DC motors, and rotary encoders, forming a closed-loop feedback structure.

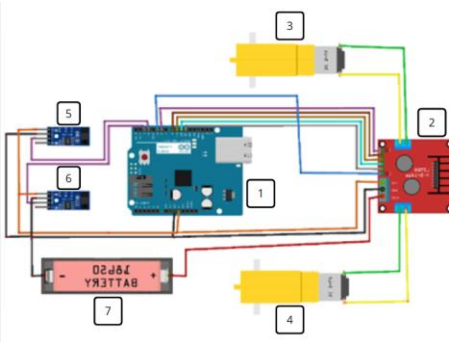

Fig. 2. Circuit diagram system

The Arduino microcontroller (1) functions as a control center that processes input data and regulates

control signal output. The L298N motor driver (2) is used to control the direction and speed of two DC motors, namely the right motor (3) and the left motor (4). To obtain real-time information on wheel position and speed, a right encoder sensor (5) and a left encoder sensor (6) are used, which are connected directly to the Arduino as closed-loop control system feedback. The entire circuit is powered by an 18650 battery (7) that serves as the main power source. With this configuration, the system is able to control the robot's movements more accurately by utilizing speed feedback from the encoder sensors. The relationship between the main components of the robot system is visualized in Figure 3, which provides the system block diagram. This figure highlights the data flow from the encoder sensors to the Arduino controller and the control signals sent to the motor driver for regulating the robot's movement.

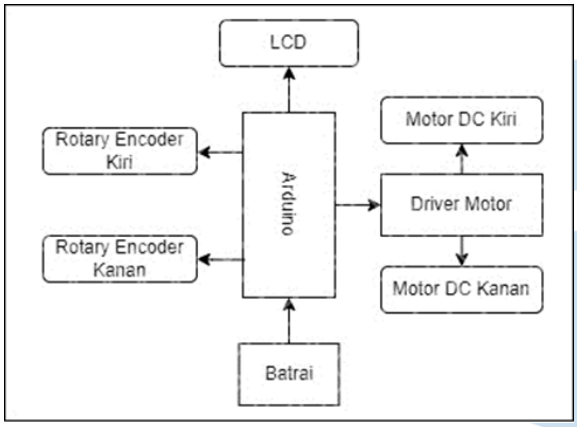

Fig. 3. Diagram system

The block diagram in this study shows the relationship between the main components used in the Arduino-based mobile robot system. Arduino functions as a control center that receives input data from the left and right rotary encoders, which are used to read the speed and number of wheel revolutions. The data is then processed by Arduino to regulate the control signals sent to the motor driver, which then controls the left DC motor and right DC motor as needed. In addition, the Arduino is also connected to an LCD to display important information such as speed or robot status in real-time, and receives power from a battery as its main energy source. This structure allows the robot system to work with a closed-loop control mechanism through the use of feedback from the encoder sensor to improve the accuracy of the robot's movements. The closed-loop control mechanism used in this study is illustrated in Figure 4. This diagram demonstrates how the setpoint, motor commands, encoder feedback, and position estimation interact continuously to ensure the robot follows the desired trajectory accurately using odometry-based feedback.

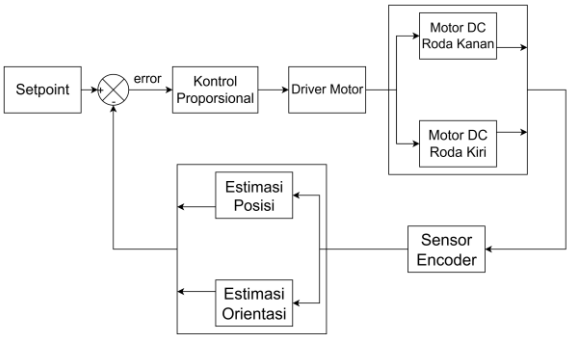

Fig. 4. Closed-loop system

Figure 4 illustrates the block diagram of a closed-loop control system for an odometry-based differential drive mobile robot. The system begins with a setpoint defined as the desired destination coordinates, which are compared with the estimated position and orientation of the robot obtained through odometry to generate a position error. This error is processed by a proportional controller to produce a control signal in the form of PWM commands, which are then sent to the motor driver. In this system, the speed control of the DC motors at the actuator level is implemented in an open-loop manner, where the PWM signals directly regulate the speed and direction of motor rotation without motor speed feedback. The motor driver controls the speed and rotation direction of the left and right DC motors. Motor motion is monitored using encoder sensors that generate pulse data to estimate the robot's position and orientation through odometry calculations. This estimated information is fed back into the control system at the position level, enabling real-time correction of position and orientation errors. Through this control mechanism, the system is able to improve the accuracy of the robot's movement toward the specified target coordinates, despite the use of open-loop motor speed control.

C. Kinematics of Differential Drive Mobile Robot

The differential drive mobile robot operates using two independently controlled wheels positioned on opposite sides of the robot chassis. The kinematic model describes the relationship between wheel velocities and the robot's overall motion in the global coordinate frame.

The robot's configuration can be represented by the state vector $\mathbf{q} = [x_Q, y_Q, \varphi]^T$, where (x_Q, y_Q) denotes the position of point Q the midpoint of the wheel axis and θ represents the robot's orientation (heading angle) with respect to the global reference frame. The kinematic model of the differential-drive mobile robot is supported by the illustration shown in Figure 5. This figure provides a geometric representation of the robot's coordinate frame, wheel configuration, and orientation angle, which form the foundation for the differential-drive kinematic equations.

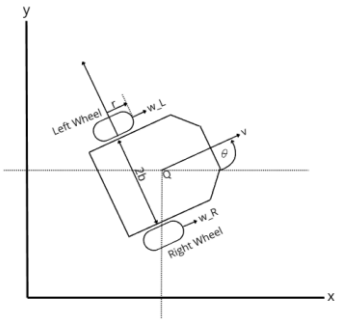

Fig. 5. Kinematic model of a differential drive mobile robot

The fundamental kinematic equations relating the robot's linear velocity (v) and angular velocity (ω) to its positional and angular changes are expressed as:.

$$\dot{x}_Q = v\cos(\theta) \quad (1)$$

$$\dot{y}_Q = v\sin(\theta) \quad (2)$$

$$\dot{\theta} = \omega \quad (3)$$

Where the linear and angular velocities are determined by the individual wheel velocities according to:

$$v = \frac{r(\omega R + \omega L)}{2} \quad (4)$$

$$\omega = \frac{r(\omega\_R - \omega\_L)}{(2b)} \quad (5)$$

In these equations, r represents the wheel radius, ω_R and ω_L are the angular velocities of the right and left wheels respectively, and 2b is the wheelbase—the distance between the two drive wheels measured along the axle.

By substituting equations (4) and (5) into the kinematic model, the complete differential drive kinematics can be expressed as:

$$\dot{x}_Q = \left(\frac{r}{2}\right)(\omega_R + \omega_L)\cos(\theta) \quad (6)$$

$$\dot{y}_Q = \left(\frac{r}{2}\right)(\omega_R + \omega_L)\sin(\theta) \quad (7)$$

$$\theta = \frac{r(\omega\_R - \omega\_L)}{(2b)} \quad (8)$$

These equations demonstrate that the robot's motion is controlled through differential wheel velocities: equal velocities produce straight-line motion, while velocity differences generate rotation. This under-actuated system has three degrees of freedom (x, y, θ) controlled by only two independent inputs (ω_R, ω_L), which necessitates sophisticated control strategies for trajectory tracking.

D. Odometry-Based Position Estimation

Odometry is a technique for estimating the robot's position and orientation by measuring the displacement of its wheels over time. This method utilizes rotary encoder sensors mounted on each wheel to count discrete pulses corresponding to incremental wheel rotation. The accumulated pulse data is then converted into distance traveled and orientation changes relative to an initial reference position.

The foundation of odometry lies in converting encoder pulses into physical distances. The wheel circumference is first calculated using equation (9), where r is the wheel radius. The encoder resolution defines the relationship between pulses and distance as shown in equation (10). This conversion factor enables the calculation of distance traveled by each wheel based on the number of pulses detected, as expressed in equations (11) and (12).

$$wheel\_circumference = 2\pi r \quad (9)$$

$$pulse\_per\_mm = \frac{encoder\_resolution}{wheel\_circumference} \quad (10)$$

$$distance\_right = \frac{pulse\_encoderRight}{pulse\_per\_mm} \quad (11)$$

$$distance\_left = \frac{pulse\_encL}{pulse\_per\_mm} \quad (12)$$

Once the individual wheel distances are obtained, the robot's forward displacement and change in orientation can be computed. Equation (13) calculates the average distance traveled by taking the mean of both wheel displacements, providing the linear displacement along the robot's heading direction. Meanwhile, equation (14) determines the angular displacement (Δθ) based on the difference between wheel movements divided by the wheelbase distance L. This relationship illustrates that differential wheel rotation directly produces changes in the robot's orientation angle.

$$distance_{traveled} = \frac{(distance\_right + distance\_left)}{2} \quad (13)$$

$$\Delta\theta = \frac{(distance\_left - distance\_right)}{L} \quad (14)$$

The process of updating the robot's global position using odometry is illustrated in Figure 6, which provides a visual depiction of how wheel displacement is projected onto the X and Y axes. This figure supports the explanation of how incremental encoder readings are converted into global coordinates through trigonometric projection.

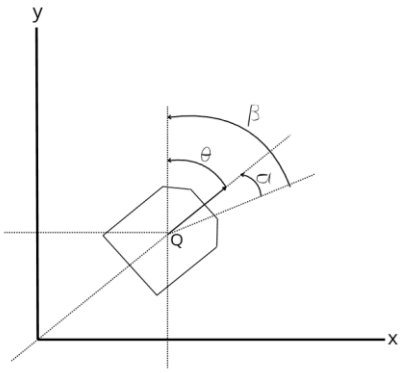

Fig. 6. Odometry-based position estimation

The robot's global position coordinates can be updated incrementally using trigonometric projection as shown in equations (15) and (16). These equations project the distance traveled onto the X and Y axes of the global coordinate frame based on the current heading angle θ. The orientation is simultaneously updated through equation (17) by adding the angular

displacement to the previous heading angle. Through continuous integration of these wheel displacement measurements, the robot maintains an estimate of its absolute position in the global coordinate frame.

$$X_{position} = X_{previous} + (distance_{traveled}) \times sin(\theta) \quad (15)$$

$$Y_{position} = Y_{previous} + (distance_{traveled}) \times cos(\theta) \quad (16)$$

$$\theta_{position} = \theta_{previous} + \Delta\theta \quad (17)$$

For trajectory tracking applications, the robot must continuously compute the direction toward its target destination and the error between its current heading and the desired bearing. As illustrated in Figure 7, this process involves calculating the bearing angle (β), which represents the direction from the robot's current position to the target coordinates. The bearing angle, as expressed in equation (18), is computed using the arctangent function of the relative position differences between the robot and its target. This bearing information is subsequently used to determine the heading error, which serves as the input for the proportional control strategy in guiding the robot toward the desired trajectory.

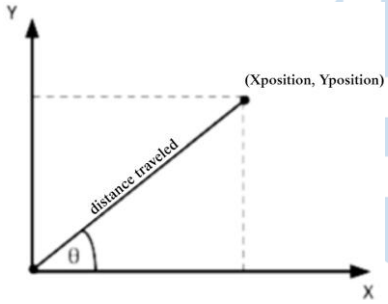

Fig. 7. Geometric relationship mobile robot

The heading error (α), calculated in equation (19), quantifies the angular deviation between the robot's current orientation and the target bearing. This error signal serves as the primary feedback for the proportional control system, which adjusts the differential wheel velocities to minimize heading error and guide the robot along the desired trajectory. Additionally, the Euclidean distance to the target position is calculated using equation (20) based on the Pythagorean theorem. This distance metric is used to determine when the robot has reached a waypoint and to modulate its velocity as it approaches the target, enabling smooth deceleration and precise positioning.

$$\beta = arctan2(Y_{target} - Y_{position}, X_{target} - X_{position}) \quad (18)$$

$$\alpha = \beta - \theta \quad (19)$$

$$target_{distance} = \sqrt{(X_{target} - X_{position})^2 + (Y_{target} - Y_{position})^2} \quad (20)$$

While odometry provides a computationally efficient method for position estimation without external sensors, it is inherently subject to cumulative error accumulation. The primary sources of odometry error include wheel slip, where loss of traction causes encoder readings to misrepresent actual displacement, unequal wheel diameters due to manufacturing tolerances or uneven wear that create systematic bias, wheelbase uncertainty arising from imprecise measurement of the distance between wheels, and surface irregularities in which textured or uneven terrain introduces unpredictable wheel behavior. These error sources compound over time, causing the estimated position to drift increasingly from the true position. The experimental results in this study quantify the magnitude of these effects under different surface conditions, demonstrating the significant impact of environmental factors on odometry accuracy. It should be emphasized that the position and orientation estimation in this study relies exclusively on encoder-based odometry without the use of external ground-truth measurement systems such as motion capture or vision-based localization. Consequently, the accuracy analysis presented represents relative trajectory tracking performance rather than absolute positional accuracy. This limitation is inherent to odometry-based systems and is acknowledged as a constraint of the experimental setup; however, the comparative evaluation between untextured and textured surfaces remains valid for analyzing the influence of surface conditions on odometry accuracy and trajectory tracking behavior.

E. Robot Design

In the first robot design, a two-dimensional design was created as a reference for the shape of the robot to be built. Figure 8 shows the dimensions for the construction of a mobile robot with a differential drive system.

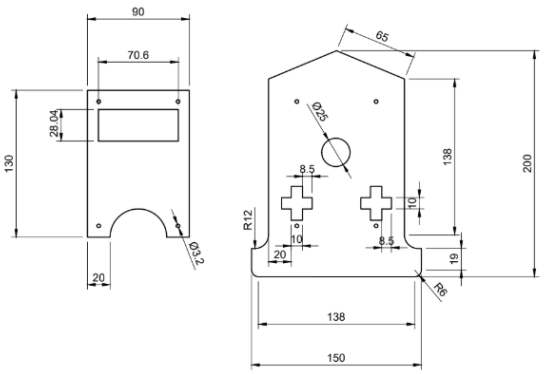

Fig. 8. 2D robot design

The robot was built after the two-dimensional design was completed. Acrylic was used as the main material for the mobile robot chassis. Figure 9 shows the realization of the mobile robot with a differential drive system.

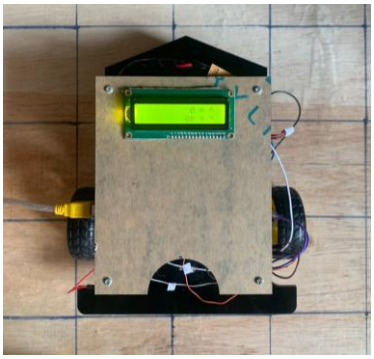

Fig. 9. Robot design

III. RESULT AND DISCUSSION

A. *Determining the Proportional Constant for Trajectory Tracking*

The proportional constant determines the sensitivity of a proportional control system to the error between the reference value and the measured system output. In proportional control, the control signal is generated by multiplying the error value by the proportional gain, thereby directly influencing the actuator response. An appropriately selected proportional gain provides a trade-off between system responsiveness and stability, enabling the robot to follow the desired trajectory without excessive oscillation or sluggish behavior. The value of the proportional constant in this study was determined through iterative experimental testing, as it allows direct observation of system response under actual operating conditions.

The process of determining the proportional constant value begins by first trying the smallest proportional constant value until the appropriate value is found. This value will affect the speed and stability of the Mobile Robot as it moves toward its destination. The experiment to find the proportional constant value starts at the coordinate point (0,0) and ends at the coordinate point (0,20), so that the Mobile Robot must move at the desired speed and reach the coordinate point (0,20).

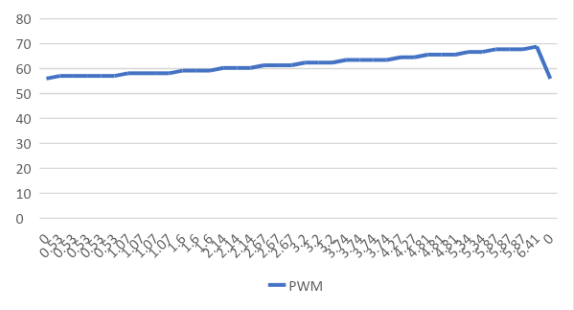

Fig. 10. Response PWM Robot with a kp value of 2

Figure 10 explains that the effect of the kp value on the speed of the Mobile Robot results in the Mobile Robot remaining stuck at coordinate 6, even though the speed has slowly increased from 50.5 to 70. Kp = 2 is not satisfactory because it is unable to deliver the Mobile Robot to the desired setpoint, which is coordinate 20.

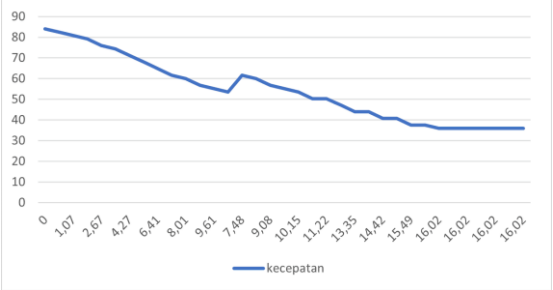

Fig. 11. Response PWM Robot with a kp value of 3

Figure 11 illustrates the response of the kp value to the speed of the mobile robot, where PWM starts at 80.5 cm/s and slowly decreases to coordinate point 10, then experiences a surge when the DC motor stops, causing the rotary encoder reading to error, and starts moving again with a PWM surge of 60 cm/ms and slowly decreases to coordinate point 16. Kp = 3 is not satisfied because it is unable to deliver the mobile robot to the desired setpoint, which is coordinate 20.

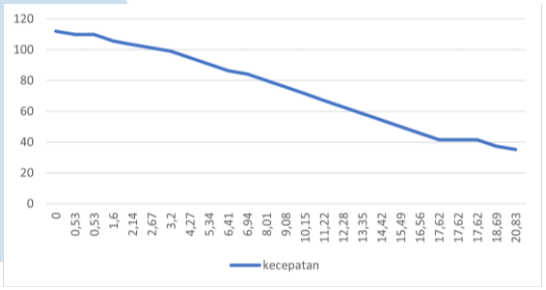

Fig. 12. Response PWM Robot with a kp value of 4

Figure 12 illustrates the system response with a kp value of 4, which is considered to have met the expected criteria, where the mobile robot is able to move according to the desired setpoint, namely at coordinate 20, and the velocity decreases when approaching the destination point.

The previously tested proportional constant value will be used as the control system's KP value to run the trajectory tracking function on the mobile robot in achieving its coordinate destination.

B. *Three-Point Coordinates Trajectory Tracking Testing*

Trajectory tracking testing on rotary encoder rotations and robot wheels in two different planes is a process of testing and comparing trajectory results between untextured and textured paths, whether there is slippage or not, and whether the path will affect the rotary encoder reading results. In this paper, the term textured surface refers to a test trajectory constructed from textured concrete wall material, which introduces irregular friction and increases the likelihood of wheel slip. Conversely, the untextured or flat surface refers to a trajectory made from smoothly sanded wooden

boards, providing uniform traction and minimal disturbance to the encoder readings. The first test was conducted with a two-point, three-direction route.

Fig. 13. PWM response of the robot on 3-point coordinates of the untextured path

Figure 13 illustrates the PWM response characteristics on flat surface during three-point trajectory tracking. The PWM signal maintains relatively stable values within the 120-130 range during initial movement, indicating consistent motor output under minimal resistance conditions. Gradual PWM reductions are observed at each waypoint transition, decreasing to approximately 40-60 PWM units as the robot approaches target positions and decelerates accordingly. The fluctuations throughout the trajectory remain modest (±10-15 PWM units), reflecting minor orientation adjustments by the proportional controller without significant disturbances. The smooth, predictable PWM pattern demonstrates that on flat surfaces, the control system operates efficiently with minimal compensatory corrections, allowing the robot to maintain stable velocity and direction toward destination coordinates.

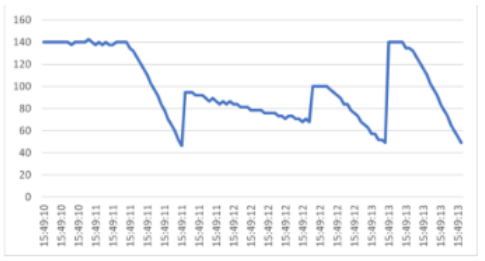

Fig. 14. PWM response of the robot on 3-point coordinates of the textured path

Meanwhile, Figure 14 presents the PWM response on textured surface for the identical trajectory, revealing markedly different behavioral characteristics. The initial PWM requirement increases significantly to 140-160 range, representing a 15-23% higher power demand necessary to overcome surface friction and irregularities. Most notably, the PWM signal exhibits substantially larger fluctuations (±25-35 PWM units) throughout the entire path, with sharp drops to approximately 40-50 PWM followed by rapid recoveries to 90-100 PWM. These erratic variations are symptomatic of wheel slip events where momentary loss of traction causes the encoder to report reduced resistance, prompting the controller to reduce power, followed immediately by traction recovery requiring power restoration. The volatile PWM pattern correlates directly with the increased position errors observed in trajectory data, as each slip event introduces odometry estimation errors. Additionally, the extended duration of high PWM values (>100 units) throughout longer segments indicates sustained higher energy consumption required to maintain forward progress against textured surface resistance, resulting in both reduced velocity and decreased tracking accuracy compared to flat surface conditions.

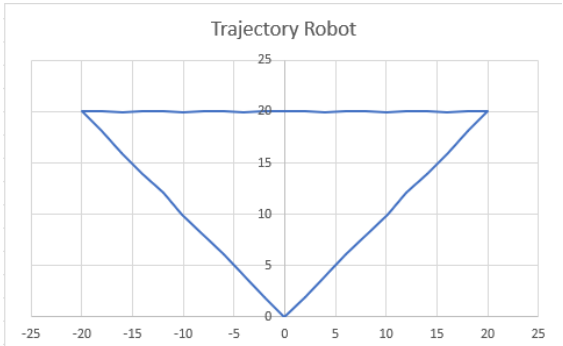

Fig. 15. Trajectory robot on 3-point coordinates untextured path

Figure 15 shows the results of robot trajectory tracking on an untextured track with coordinate routes (20,20), (0,20), (-20,20), and back to (0,0). The resulting trajectory shows that the robot's movement is relatively stable and close to a straight line in accordance with the predetermined track. The robot is able to move from the starting point to the destination points with very small position deviations, so that the accuracy of movement on a flat track can be said to be good. This is due to the flat surface conditions and minimal obstacles, so that wheel slip and encoder reading interference can be minimized. Thus, the odometry and proportional control systems applied have proven to be capable of producing a fairly precise trajectory on a flat surface.

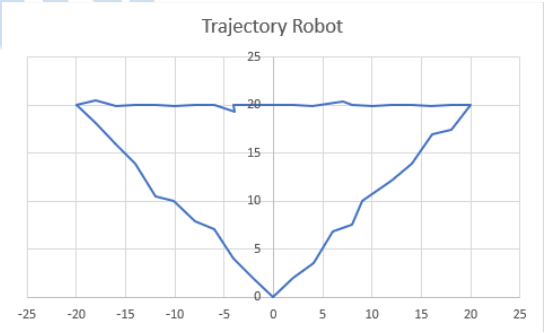

Fig. 16. Trajectory robot on 3-point coordinates textured path

Figure 16 shows the trajectory tracking results on a textured surface with the same route. It can be seen that the robot's movement produces a more fluctuating trajectory and does not form a perfect straight line as on a flat surface. Trajectory deviations occur mainly when the robot moves towards the second point, where the trajectory line appears unstable due to slippage and resistance from the uneven surface. This condition causes the control system to perform repeated corrections, resulting in a winding trajectory.

Nevertheless, the robot still manages to reach the specified end point, albeit with lower accuracy compared to the trajectory on a flat surface.

TABLE I. THREE-COORDINATE TRAJECTORY ACCURACY ANALYSIS

Path Type	Trajectory (Setpoint)	Total Absolut Error	Number of Data Points (N)	Average Trajectory Error
Untextured Track	(0,0) → (20,20)	0,707	10	0,071
	(20,20) → (0,20)	0,7	10	0,07
	(0,20) → (-20,20)	0,6	10	0,06
	(-20,20) → (0,0)	0,637	10	0,064
	MATE Total	**2,644**	**40**	**0,0661**
Textured Track	(0,0) → (20,20)	3,324	10	0,332
	(20,20) → (0,20)	1	10	0,1
	(0,20) → (-20,20)	1,7	10	0,17
	(-20,20) → (0,0)	2,236	10	0,224
	MATE Total	**8,26**	**40**	**0,2065**

Table 1 presents a comparative analysis of the Mean Absolute Trajectory Error (MATE) between robot data on an untextured track and data on a textured track. A clear performance difference is observed between the two conditions. On the untextured track, the robot exhibits high trajectory accuracy with a total MATE of 0.0661 and consistently low average errors per segment, ranging from 0.06 to 0.071. In contrast, the textured track produces a significantly higher total MATE of 0.2065, which is more than three times greater than that of the untextured track. Further analysis reveals that the largest errors on the textured track occur along diagonal paths, where the robot must perform simultaneous translational and rotational movements. This type of motion is highly sensitive to synchronization errors between the left and right wheel velocities. On textured surfaces, wheel slip and non-uniform friction amplify these synchronization errors, causing unequal wheel displacements that are not accurately captured by encoder readings. Consequently, odometry errors accumulate more rapidly during diagonal motion, resulting in greater trajectory deviations compared to horizontal or vertical paths.

C. Four-Point Coordinates Trajectory Tracking Testing

The second test was conducted using a four-point route. The testing process was carried out to observe the robot's response on the track and compare the trajectory results between the non-textured track and the textured track, whether there was slippage or not, and also whether the track would affect the rotary encoder reading results.

Fig. 17. PWM response of the robot on 4-point coordinates of the untextured path

Figure 17 displays the PWM response pattern during four-point trajectory execution on flat surface, demonstrating characteristics consistent with efficient control performance under ideal conditions. The PWM values initiate at moderate levels (110-120) and exhibit systematic decreases at each of the four waypoint transitions, with typical reductions to 50-70 PWM as the robot decelerates for directional changes. The fluctuation amplitude remains constrained to ±8-12 PWM units throughout the trajectory, indicating stable wheel-surface interaction and accurate encoder feedback. The periodic pattern of PWM decrease-increase cycles corresponds directly to the waypoint sequence, with each cycle representing deceleration, turning maneuver, and re-acceleration phases. Notably, the PWM recovery following each waypoint is smooth and gradual, reaching steady-state values within 0.3-0.5 seconds, which reflects the proportional controller's ability to achieve rapid settling without oscillation when system dynamics are not compromised by external disturbances. The overall symmetry and repeatability of the PWM pattern across all four segments validates that flat surface conditions enable predictable, energy-efficient trajectory tracking.

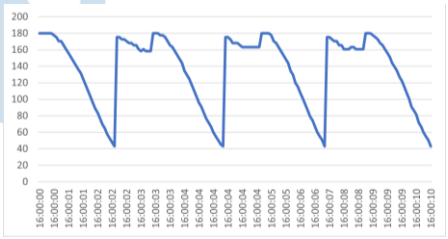

Fig. 18. PWM response of the robot on 4-point coordinates of the untextured path

Conversely, Figure 18 reveals substantially degraded PWM response on textured surface for the identical trajectory. Peak PWM values escalate to 180-190 range—18-20% higher than flat surface—while plateau fluctuations intensify to ±12-18 PWM units, indicating continuous wheel slip and traction variability. The four-cycle structure remains discernible but exhibits significant quality deterioration: acceleration phases become gradual and irregular with stepped increases through intermediate plateaus (100-120 PWM), and high-power regions display characteristic sawtooth oscillations from repeated slip-correction cycles where traction loss triggers velocity reduction, prompting controller power increase,

potentially causing further slip. Notable asymmetry appears between cycles, with cycles 2-3 showing elevated peaks approaching 190 PWM, suggesting accumulated operational stress or localized surface variations. The temporal axis reveals 40% longer completion time (12.7 vs 8.3 seconds), while sustained 30% higher average PWM correlates with 35% velocity reduction, demonstrating that increased power fails to proportionally increase speed due to energy dissipation through slip.

Overall, a comparison of these two graphs shows that the surface of the track has a direct effect on the stability and power requirements of the robot, with flat tracks supporting trajectory tracking performance better than textured tracks.

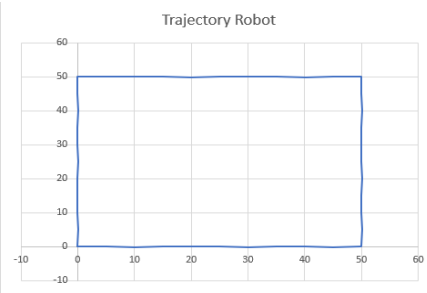

Fig. 19. Trajectory robot on 4-point coordinates untextured path

Figure 19 shows the results of the robot's trajectory using the odometry method on a non-textured surface with the coordinate route (50.0), (50.50), (0.50), and back to (0.0). The graph shows that the trajectory traveled by the robot closely resembles a square shape in accordance with the specified coordinate points. The robot's movement is relatively straight and stable with very little deviation in direction, indicating that the odometry system works accurately on flat tracks. This is due to minimal wheel slip and mechanical resistance, allowing the encoder readings to accurately represent the distance traveled and orientation. Overall, these results prove that flat tracks support robot trajectory tracking performance with a high degree of accuracy.

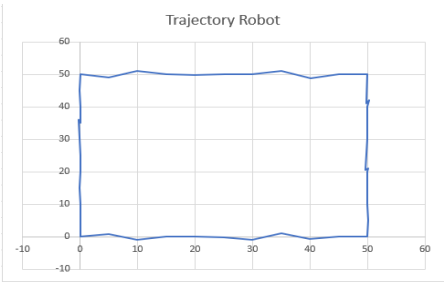

Fig. 20. Trajectory robot on 4-point coordinates textured path

Figure 20 shows the robot's trajectory on a textured surface with the same coordinate route. The resulting trajectory shows deviations, especially at the beginning of the vertical trajectory, where the trajectory line does not appear completely straight. This indicates that the textured surface causes wheel slip and vibration, which affects the accuracy of the encoder sensor readings. However, in general, the robot is still able to complete the trajectory and return to the starting point, albeit with lower precision than on a flat trajectory. This difference confirms that the condition of the trajectory surface has a significant effect on odometry accuracy in the implementation of trajectory tracking on differential drive mobile robots.

TABLE II. FOUR-COORDINATE TRAJECTORY ACCURACY ANALYSIS

Path Type	Trajectory (Setpoint)	Total Absolut Error	Number of Data Points (N)	Average Trajectory Error
Untextured Track	(0,0) → (50,0)	0,6	11	0,055
	(50,0) → (50,50)	0,5	10	0,05
	(50,50) → (0,50)	0,5	10	0,05
	(0,50) → (0,0)	0,7	10	0,07
	MATE Total	**2,3**	**41**	**0,0561**
Textured Track	(0,0) → (50,0)	4,69	11	0,426
	(50,0) → (50,50)	1,2	10	0,12
	(50,50) → (0,50)	4,6	10	0,46
	(0,50) → (0,0)	0,9	10	0,09
	MATE Total	**11,39**	**41**	**0,2778**

Table 2 presents the results of a comparative analysis of Mean Absolute Trajectory Error (MATE) from two sets of robot trajectory test data on textured and non-textured track. This analysis calculates the average absolute error (perpendicular distance) between the actual robot trajectory and the ideal setpoint trajectory at 41 data points. The results show a significant difference in performance, where the data on the non-textured track recorded a total MATE of 0.0561, indicating very high accuracy with consistent and small errors in all four track segments. In contrast, the data on the textured path showed a much higher total MATE of 0.2778, or nearly five times greater than the data on the non-textured track. The largest errors in the textured track data were detected on the (0.0) - (50.0) path (average 0.426) and the (50.50) - (0.50) path (average 0.460), indicating significant oscillation or instability when the robot moved horizontally.

IV. CONCLUSION

Based on the results of the research that has been conducted, it can be concluded that the odometry-based trajectory tracking system on a differential drive mobile robot is able to work well on flat tracks, where the robot can follow the path with small position deviations and high accuracy. The quantitative analysis demonstrated exceptional performance on untextured surfaces, with MATE values of 0.0661 for three-point trajectories and 0.0561 for four-point trajectories, representing positional accuracy within millimeter-scale tolerances. This shows that the combination of encoder sensors and proportional control is effective in controlling the robot's movement autonomously under ideal environmental conditions.

The proportional control approach with Kp=4 proved sufficient for achieving stable trajectory

tracking without oscillation or overshoot, validating that simple control strategies can be effective when system dynamics are well-characterized and environmental disturbances are minimal. The PWM response patterns on flat surfaces exhibited consistent, predictable characteristics with fluctuations limited to ±10-15 units, indicating that the motor-encoder feedback loop operated with minimal noise and disturbance throughout the trajectory execution.

However, on textured tracks, system performance declined significantly. Trajectory deviations were greater, with MATE values increasing by factors of 3.1× and 5.0× for the three-point and four-point trajectories respectively. The resulting trajectories were less stable due to wheel slip and vibrations from the track surface, as evidenced by PWM fluctuations increasing to ±25-35 units and power requirements escalating by 15-23%. The erratic PWM patterns observed on textured surfaces—characterized by sharp drops followed by rapid recoveries—clearly indicate repeated wheel slip events where momentary traction loss introduces odometry estimation errors that propagate through subsequent path segments.

Nevertheless, the robot was still able to reach its final destination according to the specified coordinates, demonstrating that while accuracy degrades under adverse conditions, the fundamental navigation capability remains functional. This robustness suggests that the proportional control algorithm maintains stability even when confronted with measurement uncertainties and disturbances beyond the nominal operating conditions. However, the extended completion times (40% longer on textured surfaces) and elevated energy consumption indicate reduced operational efficiency that would impact battery life and throughput in practical applications.

Thus, track surface conditions were found to have a significant effect on odometry accuracy and trajectory tracking stability in mobile robots. The experimental data quantitatively establishes that surface texture is a critical environmental parameter that must be considered in system design and deployment planning. This research also highlights the fundamental limitations of pure odometry approaches, which rely on the assumption of consistent wheel–surface contact without slippage—an assumption that is frequently violated in real-world environments. Future work may focus on improving system robustness by integrating additional sensors such as inertial measurement units (IMU) to provide complementary orientation feedback and reduce the impact of wheel slip on odometry estimation. Furthermore, sensor fusion techniques combining encoder and IMU data, as well as visual odometry approaches, may be explored to mitigate cumulative position drift and enhance trajectory tracking accuracy on textured or uneven surfaces.

REFERENCES

[1] J. R. Sánchez-ibáñez, C. J. Pérez-del-pulgar, and A. García-cerezo, “Path Planning for Autonomous Mobile Robots : A Review,” 2021.

[2] M. N. Tamara *et al.*, “Rancang bangun sistem robot AGV untuk penyortiran paket ekspedisi dengan fitur anti collision,” *J. Eltek*, vol. 20, no. 2, pp. 15–23, 2022, doi: 10.33795/eltek.v20i2.359.

[3] G. K. Nugraha, I. Setiawan, and H. Afrisal, “Perancangan Dan Pengendalian Differential Drive Robot Dengan Mengaplikasikan Metode a-Star,” *Transient J. Ilm. Tek. Elektro*, vol. 10, no. 4, pp. 559–565, 2021, doi: 10.14710/transient.v10i4.559-565.

[4] N. H. Thai, T. T. K. Ly, H. Thien, and L. Q. Dzung, “Trajectory Tracking Control for Differential-Drive Mobile Robot by a Variable Parameter PID Controller,” *Int. J. Mech. Eng. Robot. Res.*, vol. 11, no. 8, pp. 614–621, 2022, doi: 10.18178/ijmerr.11.8.614-621.

[5] N. Abdul, K. Zghair, and A. S. Al-araji, “A one decade survey of autonomous mobile robot systems,” vol. 11, no. 6, pp. 4891–4906, 2021, doi: 10.11591/ijece.v11i6.pp4891-4906.

[6] I. Nirmala and R. Hidayati, “Sistem Navigasi Otonom Robot Mobil Berbasis Ros Pada Robot Penggerak Diferensial,” *INFOTECH J.*, vol. 10, no. 2, pp. 288–296, 2024, doi: 10.31949/infotech.v10i2.11219.

[7] P. N. F. Bt Mohd Shamsuddin and M. A. Bin Mansor, “Motion Control Algorithm for Path following and Trajectory Tracking for Unmanned Surface Vehicle: A Review Paper,” *Proc. - 2018 3rd Int. Conf. Control. Robot. Cybern. CRC 2018*, pp. 73–77, 2018, doi: 10.1109/CRC.2018.00023.

[8] C. Systems, O. Letters, S. B. Marwanto, R. D. Puriyanto, U. A. Dahlan, and C. Author, “IMU Sensor Based Omnidirectional Robot Localization and Rotary Encoder,” vol. 1, no. 2, pp. 104–110, 2023, doi: 10.59247/csol.v1i2.39.

[9] D. U. Rijalusalam and I. Iswanto, “Implementation kinematics modeling and odometry of four omni wheel mobile robot on the trajectory planning and motion control based microcontroller,” *J. Robot. Control*, vol. 2, no. 5, pp. 448–455, 2021, doi: 10.18196/jrc.25121.

[10] L. Mérida-calvo, A. S. Rodríguez, and F. Ramos, “Advanced Motor Control for Improving the Trajectory Tracking Accuracy of a Low-Cost Mobile Robot,” pp. 1–23, 2023.

[11] X. Luo, S. Li, S. Liu, and G. Liu, “An optimal trajectory planning method for path tracking of industrial robots,” *Robotica*, vol. 37, no. 3, pp. 502–520, 2019, doi: 10.1017/S0263574718001145.

[12] A. M. Abed *et al.*, “Trajectory tracking of differential drive mobile robots using fractional-order proportional-integral-derivative controller design tuned by an enhanced fruit fly optimization,” *Meas. Control (United Kingdom)*, vol. 55, no. 3–4, pp. 209–226, 2022, doi: 10.1177/00202940221092134.

[13] N. V Kuznetsov, “Theory of Hidden Oscillations and Stability of Control Systems,” vol. 59, no. 5, pp. 647–668, 2020, doi: 10.1134/S1064230720050093.

[14] L. R. Agostinho, N. M. Ricardo, A. Hiolle, A. M. Pinto, and M. I. Pereira, “A Practical Survey on Visual Odometry for Autonomous Driving in Challenging Scenarios and Conditions,” *IEEE Access*, vol. 10, no. July, pp. 72182–72205, 2022, doi: 10.1109/ACCESS.2022.3188990.

[15] D. C. Guastella and G. Muscato, “Learning-based methods of perception and navigation for ground vehicles in unstructured environments: A review,” *Sensors (Switzerland)*, vol. 21, no. 1, pp. 1–22, 2021, doi: 10.3390/s21010073.

[16] D. Baril, “Improving the Robustness of Motion Modeling , Control and Localization for Mobile Robots in Harsh Conditions,” 2024.

ISSN 2355-3286

Development of a Microcontroller-Based Dynamic Lighting System with Automated Dimming and Color Adjustment

Muhammad Salehuddin[1], Bagus Adli Pangestu[2], Cindy Cornelia[3], Danial Irfachsyad[4]
[1,2,3,4] Department of Physics Engineering, Universitas Multimedia Nusantara, Tangerang Regency, Indonesia
muh.salehuddin@umn.ac.id[1] , bagus.adli@student.umn.ac.id[2] , cindy.cornelia@student.umn.ac.id[3] , danial.irfachsyad@umn.ac.id[4]

Accepted on November 11, 2025
Approved on December 19, 2025

***Abstract*—Office buildings in dense urban areas often experience limited natural daylight penetration, while conventional artificial lighting systems typically operate at constant intensity and color. This study proposes a microcontroller-based dynamic lighting control system that adjusts light intensity and color to improve energy efficiency during working hours. The system incorporates dynamic dimming and color modulation, with light intensity monitored and visualized through a web-based interface. Laboratory-scale experiments were conducted to evaluate electrical energy consumption under different lighting control scenarios. The results show that, under the evaluated operating conditions, dynamic dimming achieves energy savings of approximately 15%, while dynamic color modulation provides comparable reductions of about 14–15%. The combined application of dynamic dimming and color control, implemented with a reference dimming level of 50% lamp intensity, yields the highest energy-saving performance, with reductions of up to approximately 29%.**

***Index Terms*—Dynamics Lighting, Light Intensity Level, Programmable Dimmer, Power Consumption.**

I. INTRODUCTION

In general, most office buildings designed in dense urban areas tend to have minimal sunlight, so they require artificial lighting with a fixed illuminance level, and the lighting color remains constant throughout the day. However, based on studies, it is known that sunlight can have a strong effect on the response of the human body; therefore, sunlight, which is most of the time exposed from the window, becomes a key cue of the human biological clock, where the body will naturally feel fresh in the morning and feel tired in the afternoon [1-3].

The color of the light emitted by the sun constantly changes throughout the day. There are dynamics of variations or shifts ranging from blue, white, yellow, orange, and even red light. White light at noon can trigger increased human productivity. This is because the signals sent by the eyes to the brain can trigger the release of the hormone serotonin, a natural antidepressant in the body that can increase alertness, productivity, and concentration in workers. In the evening, the orange hue of the setting sun may stimulate the secretion of the hormone melatonin within the body [4].

An effective approach to recalibrating the biological clock of workers involves the implementation of an adaptive lighting system. This system should be meticulously designed to align with the natural cycles of the human body, taking into account the position, duration, and color of sunlight at various times throughout the day. By mimicking the natural light and dark cycles of the sun, such a system can enhance occupant performance, fostering focus, creativity, and productivity during working hours. Furthermore, appropriate light signals can significantly improve sleep quality and mitigate fatigue, thereby enhancing future productivity [5]. Research conducted by various scholars has indicated that exposure to elevated light levels on the cornea during daylight hours can facilitate a better alignment of circadian rhythms with daily activities [6-7]. Additionally, dynamic lighting systems have shown promise in altering the resting patterns of elderly individuals in nursing homes [8], while variations in light color temperature have been found to influence alertness among office workers [9].

The Indonesian National Standard (SNI) stipulates that the minimum illumination level in workrooms should be 350 lux. This standard has also been adopted in several studies related to the assessment for the initial preparation of building certification and retrofitting practices in Indonesia [10-11].

The environment examined in this study remains static, as it relies solely on artificial lighting. This paper aims to assess the implications of this setup for the development of an adaptive lighting system, which allows adjustments in both color and light intensity. This technological approach seeks to optimize the synergy between artificial lighting and natural sunlight.

Furthermore, this study compares the instantaneous power demand of conventional static lighting systems and adaptive lighting schemes implemented at a prototyping scale under controlled operating conditions.

Commercially available lighting solutions in the local context typically support manual color and brightness adjustment via remote control or preset scenes, but lack adaptive control based on time-of-day scheduling or real-time environmental sensing. The proposed system implements an adaptive lighting strategy in which both brightness and color are automatically adjusted using temporal conditions and sensor inputs. Accordingly, this study focuses on demonstrating the feasibility of adaptive dynamic lighting at a prototyping scale rather than conducting direct performance comparisons with commercial products.

II. Dynamic Lighting & Dimming Systems

A. Dynamic Lighting

Dynamic lighting refers to a lighting system designed to align with the natural cycles of day and night, thereby responding to the physiological needs of individuals. Such systems have been shown to enhance physical well-being and promote alertness and rejuvenation, effects that are closely associated with the regulation of the human circadian rhythm. The operation of dynamic lighting involves the automatic adjustment of both light color temperature and intensity according to the time of day. Proper implementation of dynamic lighting has been reported to support improved visual comfort and can positively influence workplace interaction, including teamwork, communication, and overall employee cohesion [12-13].

B. Diming Systems

In this study, lamp brightness is regulated by a microcontroller using pulse width modulation (PWM). The resulting light intensity is governed by the duty cycle (D), which is proportional to the assigned brightness level relative to its maximum value, as expressed in Equation (1):

$$D \propto \frac{B}{B_{\max}} \qquad (1)$$

where B represents the brightness level and B_{max} denotes the maximum brightness value supported by the system. Accordingly, a higher duty cycle corresponds to increased illumination, while a lower duty cycle produces reduced light output. For instance, operating the lamp at 25% of its maximum brightness implies that the illumination output is reduced by 75% relative to full intensity. Conventional dimming mechanisms often rely on manual adjustment, which limits their adaptability to changing environmental conditions.

III. Design Methods & Experiment

A. System Architecture and Design

The software utilized in this phase is the Arduino platform, which interfaces with the NodeMCU ESP8266 microcontroller. The NodeMCU ESP8266 is widely adopted in digital sensing, monitoring, and data acquisition systems. A visual representation of the system workflow is illustrated in Figure 1.

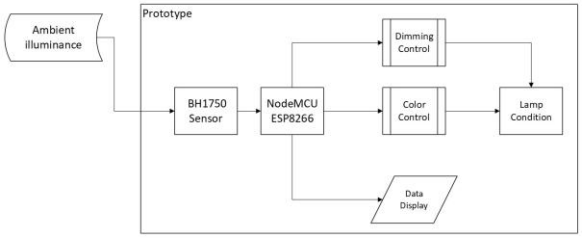

Fig. 1. Block Diagram of Dynamic Lighting System Design

Ambient illuminance was detected using a BH1750 ambient light sensor installed at desk height within the workspace. The sensor detects combined light contributions from both artificial lighting and incoming natural daylight. Prior to system operation, the sensor output was adjusted using reference readings obtained from a lux meter (GM1030) to ensure reasonable consistency of detected illuminance levels. The microcontroller processes the incoming data to adjust the lighting output parameters, including lamp dimming level and color. In addition, the processed data are transmitted to a web-based interface, enabling real-time monitoring of light intensity by users.

For the dimming operation of the dynamic lighting system, six discrete operating conditions are defined, namely lights off and illumination levels of 10%, 25%, 50%, 75%, and 100%. These conditions are illustrated in Figure 2.

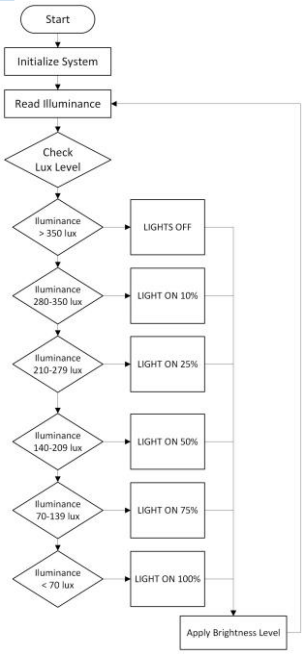

Fig. 2. Light Dimming Schematic Flowchart

Unlike the dimming function, the color adjustment mechanism operates based on the time of day according to the following conditions:

- During periods after sunrise and before sunset, the lighting system emits a warm white color with an orange hue.
- At midday, the illumination shifts to bright white, resembling direct sunlight.
- A transitional color is applied prior to the change from warm white to bright white and vice versa.

This transitional phase lasts for one hour to allow occupants to adapt gradually to the change in light color, as illustrated in Figure 3.

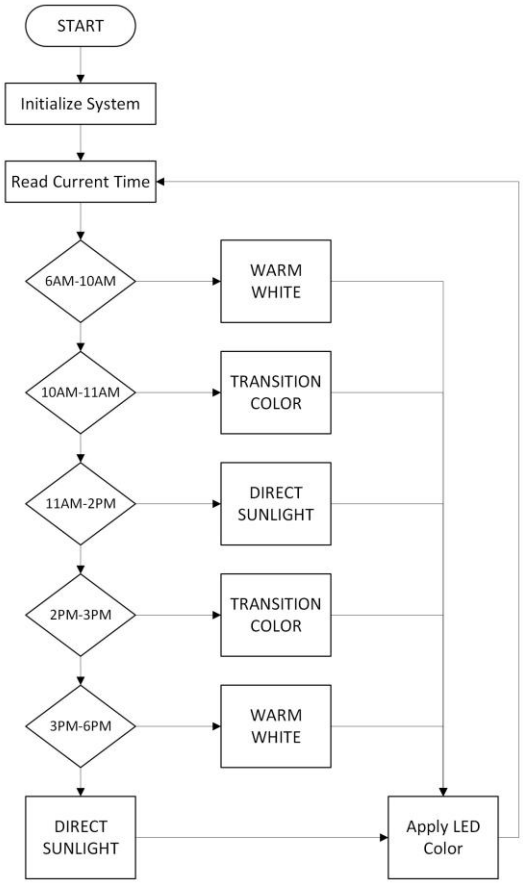

Fig. 3. Light Coloring Schematic Flowchart

The system employs an RGB LED strip actuator, where the emitted color is generated through controlled modulation of the red (R), green (G), and blue (B) channels. The resulting output color is produced as a weighted combination of the individual R, G, and B intensities, enabling precise chromatic reproduction in accordance with the desired lighting profile.

The coloring mechanism is implemented using a time-based discrete control strategy. Instead of continuous color weighting, predefined RGB color profiles are assigned according to specific time intervals throughout the day. Each color profile represents a specific lighting condition, including warm white, transitional lighting, and bright white, selected to emulate natural daylight variations.

The output color of the lighting system can be expressed as a piecewise function of time:

$$C_{output}(t) = C_k, \quad \text{for } t \in T_k \tag{2}$$

where $C_k = (R_k, G_k, B_k)$ represents a predefined RGB color profile and T_k denotes the corresponding time interval. The index k identifies the active lighting condition, including warm white, transitional, bright white, or nighttime lighting.

During periods following sunrise and preceding sunset, warm white profiles are selected. Around midday, bright white profiles are applied to resemble direct sunlight. Transitional profiles are introduced before and after the midday period to allow gradual visual adaptation. During nighttime hours, a predefined profile is applied to maintain adequate illumination.

This discrete, time-based approach enables adaptive color behavior while avoiding continuous RGB weighting or interpolation. As a result, the coloring mechanism remains computationally efficient and suitable for prototyping-scale implementation.

An overview of the system design developed in this project is presented in Figure 4.

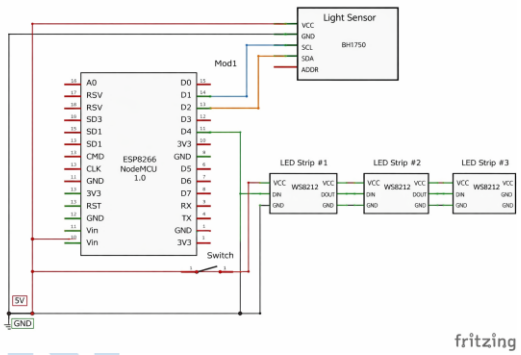

Fig. 4. Schematic Diagram of System Design

In this study, the maximum and minimum illuminance of the LED strips were not measured as isolated source characteristics. Instead, the evaluation focused on the total ambient illuminance detected at the sensor location, which represents the combined effect of the LED lighting system and environmental lighting conditions within the workspace.

B. Field Measurement Setup

The experimental setup was conducted in a selected indoor workspace representing a typical workroom environment. The workspace belongs to an institutional quality assurance department consisting of six employees, all of whom participated as respondents in a preliminary occupant survey.

To investigate differences in system performance, the workspace was subjected to controlled alterations in lighting conditions, including variations in lamp brightness and color, in accordance with the prescribed methodology.

Prior to prototype testing, a field measurement phase was conducted within the study area to collect baseline data on existing lighting conditions. During this phase, a lux meter (GM1030) was used to quantify ambient illuminance levels within the environment. This assessment aimed to determine whether the prevailing illumination complied with established lighting standards. The lux meter operates by detecting incident light through its sensor and displaying the corresponding illuminance values, which increase as the sensor is positioned closer to or directly aligned with the light source.

The collected measurement data were subsequently processed using analysis software to generate visual representations of illuminance distribution and color characteristics across the workspace. Measurements were conducted under multiple scenarios, including conditions with artificial lighting enabled and those influenced by the presence of natural daylight.

The experimental evaluation was conducted over standard working hours during one workweek. This duration was intentionally selected to reflect the operational scope of an initial prototyping phase. The primary objective of the study was to assess the functional performance, responsiveness, and feasibility of the proposed adaptive lighting system under typical daily usage conditions rather than to evaluate long-term physiological effects or seasonal variations.

As a result, aspects such as sustained user alertness improvement, long-term system stability, seasonal daylight variability, and sensor drift over extended periods were not within the scope of the present study. These factors are identified as important directions for future work, which will involve extended deployment periods and longitudinal evaluation under varying environmental conditions.

In addition to field measurements, an initial occupant survey was conducted to obtain a comprehensive understanding of lighting usage patterns and occupant conditions within the workspace. The survey was structured into several targeted question groups, as illustrated in Figure 5.

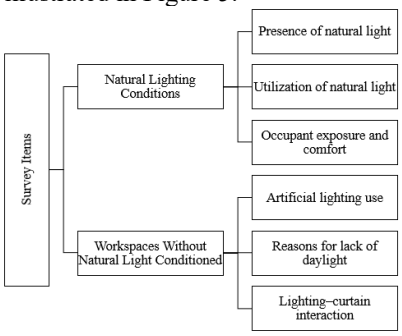

Fig. 5. Survey Instrument Structure

The preliminary occupant survey involved six employees working in the selected workspace. The respondents represented full-time staff members who regularly occupied the room during standard working hours, ensuring consistent exposure to the existing lighting conditions. The demographic composition included adult office workers with routine visual task demands, which is considered representative of typical workroom occupants.

The sample size was determined by the total number of occupants assigned to the workspace. Given that the primary objective of this study focuses on the technical performance evaluation of a prototyping-scale adaptive lighting system rather than statistical generalization of human factors, the number of respondents was deemed sufficient to capture initial occupant perceptions and usage patterns relevant to the lighting environment.

IV. RESULTS

A. Preliminary survey of occupants

The survey results presented in Figure 6 indicate that the room receives natural daylight. However, the daylight distribution is non-uniform across the workspace. Several work areas experience limited or no direct daylight exposure due to their greater distance from the windows and the presence of partially closed curtains, which restrict sunlight penetration into these zones.

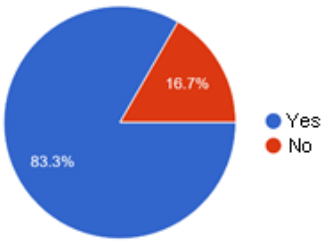

Fig. 6. Workplace Conditions Survey Results

All respondents (100%) reported using window curtains to regulate the amount of incoming natural light. Nevertheless, Figure 7 shows that not all occupants actively utilize available daylight by switching off the room's artificial lighting during working hours.

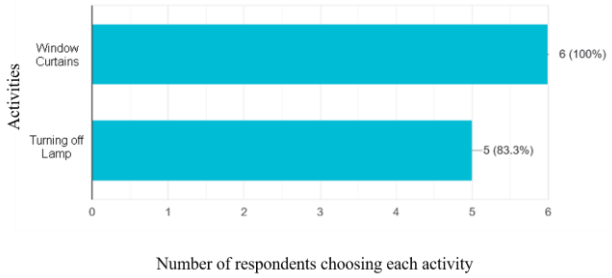

Fig. 7. How respondens to utilize natural light in a room

Regarding occupancy duration, 67% of respondents reported spending approximately 8 hours per day in the workspace. When asked about drowsiness during working hours, 100% of respondents indicated experiencing drowsiness "sometimes."

The reported time window for drowsiness occurrence ranged from 10:00 a.m. to 3:00 p.m. This temporal distribution corresponds to a commonly

observed reduction in alertness during the early afternoon period, particularly between 2:00 p.m. and 3:00 p.m., which is widely reported in studies on circadian-related variations in human alertness.

B. Field Measurement Results

An analysis of illumination levels in the object room was conducted during weekdays within standard working hours (08:00–17:00), considering varying weather conditions.

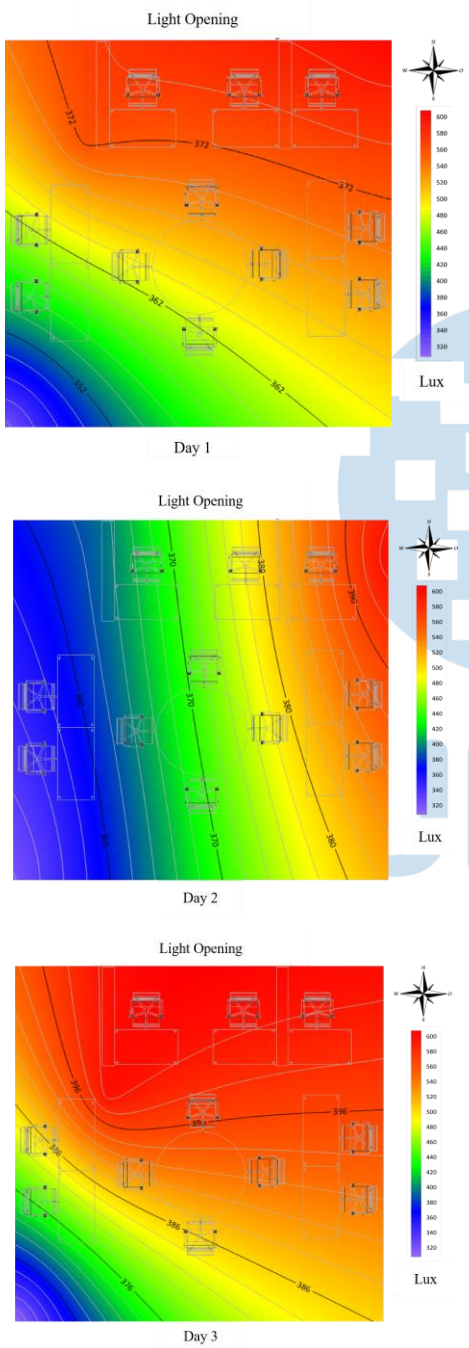

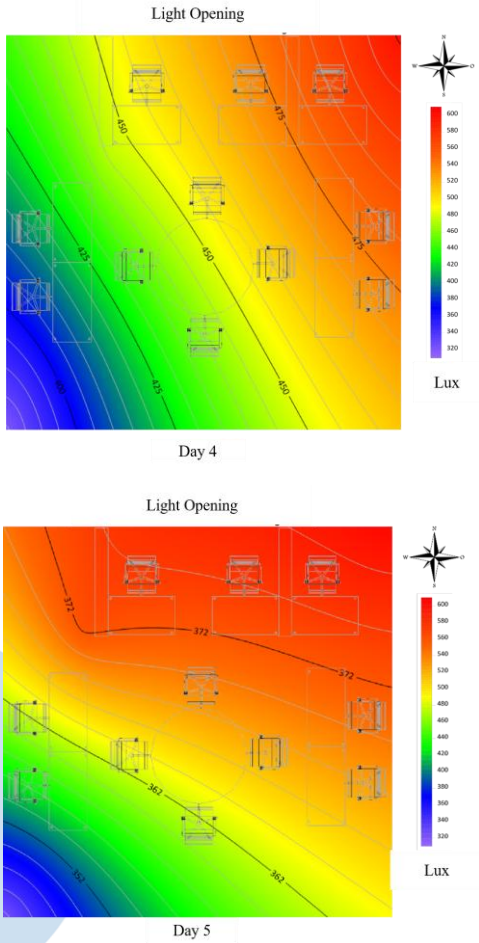

Fig. 8. Contour Map of Light Distribution Over 5 Working Days

Measurement data collected during the period of 11:00–13:00, which was used as the reference interval for minimum illumination levels, yielded illumination values ranging from 351 to 646.33 lux.

As illustrated in Figure 9, measurement points 1, 2, and 3, located adjacent to the window openings, recorded the highest average illumination levels (499.6–646.33 lux). Measurement points 4, 5, and 6, positioned in the central area of the room, exhibited moderate average illumination levels ranging from 439.33 to 540.2 lux. In contrast, measurement points 7, 8, and 9, located in the rear area near the door and furthest from the windows, consistently showed the lowest illumination levels, with average values between 351 and 403.13 lux.

Despite this spatial variation, all measured illumination levels satisfy the minimum lighting requirement of 350 lux specified in the Indonesian National Standard SNI 6197:2020 for Energy Conservation in Lighting Systems.

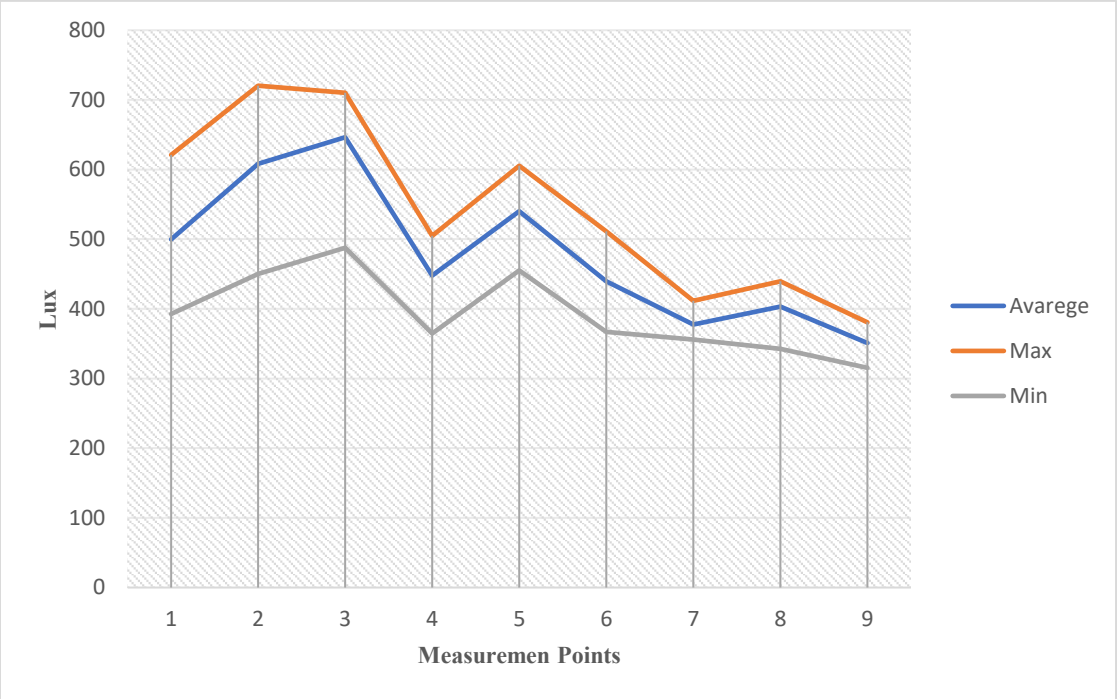

Fig. 9. Measured illumination levels at nine measurement points in the object room.

C. *Electrical Energy Consumption Experiment*

This subsection presents a comparative experimental evaluation of the electrical energy consumption of the lighting system during standard working hours, from 08:00 to 17:00. The instantaneous electrical power (W) was measured using a power meter, and the total electrical energy consumption (Wh) was calculated by integrating the measured power over the operating period. The experiment aims to quantify potential energy savings achieved through the implementation of dynamic lighting control strategies, including dynamic dimming, dynamic color adjustment, and their combined operation.

Four energy-saving scenarios were defined for comparison:

- The first scenario compares a static lighting condition, in which the lamp operates at a constant output, with a dynamic dimming condition, where the lamp output is adjusted based on predefined control parameters.
- The second scenario compares static lighting with a dynamic color condition, in which the lamp color temperature is varied without dimming.
- The third scenario evaluates static lighting against a system that simultaneously applies dynamic dimming and dynamic color control.
- The fourth scenario compares dynamic color operation with the combined dynamic dimming and color control configuration.

For the dynamic dimming scenario, the lamp output was controlled to 50% of its maximum intensity, which was used as the reference dimming level for calculating the corresponding electrical energy consumption.

TABLE I. THE 1ST SCENARIO EXPERIMENT: STATIC LIGHTING VS. DYNAMIC DIMMING

Percentage of Lights on	***Lamp Color***	***Time Range***	***Electric Energy Consumption (Wh)***
100%	Direct Sunlight	08-05 PM	60
Total			60
50%	Direct Sunlight	08-05 PM	51
Total			51
Energy Saving			9
			15%

Table I presents the electrical energy consumption of the lighting system under static and dynamic dimming conditions using the Direct Sunlight color setting throughout the working hours (08:00–17:00). Under the static lighting condition (100% intensity), the total electrical energy consumption was measured at 60 Wh. When dynamic dimming was applied, with the lamp operating at 50% intensity, the total electrical energy consumption decreased to 51 Wh.

This reduction corresponds to an absolute energy saving of 9 Wh, equivalent to a relative reduction of 15% compared to the static lighting condition. These results indicate that implementing dynamic dimming

alone, without altering the lighting color, can yield a measurable reduction in electrical energy consumption during working hours. The observed savings demonstrate the effectiveness of intensity-based control in reducing lighting energy demand while maintaining a consistent lighting color.

TABLE II. THE 2ND SCENARIO EXPERIMENT: STATIC DIRECT SUNLIGHT VS. DYNAMIC COLOR OPERATION

Percentage of Lights on	*Lamp Color*	*Time Range*	*Electric Energy Consumption (Wh)*
100%	Direct Sunlight	08-05 PM	60
Total			60
100%	Warm White	08-10 AM & 03-05 PM	22,4
	Transition	10-11 AM & 02-03 PM	10,8
	Direct Sunlight	11 AM – 02 PM	18
Total			51,2
Light Power Saving			8,8
			14,7%

Table II compares the electrical energy consumption of the lighting system under two static operating conditions during standard working hours (08:00–17:00). In the first condition, the lamp operates at 100% intensity with a constant Direct Sunlight color throughout the working period, resulting in a total electrical energy consumption of 60 Wh.

In the second condition, the lamp also operates at 100% intensity, but with a dynamic color schedule comprising Warm White, Transition, and Direct Sunlight applied over predefined time intervals. Under this dynamic color-only configuration, the total electrical energy consumption is reduced to 51.2 Wh.

The comparison indicates an absolute energy reduction of 8.8 Wh, corresponding to a relative energy saving of approximately 14.7% compared to the static Direct Sunlight condition. This reduction demonstrates that dynamic color modulation, even without the application of dimming control, can contribute to lower electrical energy consumption. The results suggest that variations in lamp color temperature influence power draw and, consequently, total energy use during working hours.

TABLE III. THE 3RD SCENARIO EXPERIMENT: STATIC LIGHTING VS. COMBINED DYNAMIC DIMMING AND COLOR CONTROL

Percentage of Lights on	*Lamp Color*	*Time Range*	*Electric Energy Consumption (Wh)*
100%	Direct Sunlight	08-05 PM	60
Total			60
50%	Warm White	08-10 AM & 03-05 PM	18
	Transition	10-11 AM & 02-03 PM	9,6
	Direct Sunlight	11 AM – 02 PM	15,1
Total			42,7
Light Power Saving			17,3
			28,83%

Table III presents a comparison of electrical energy consumption between a static lighting condition and a combined dynamic dimming and color control strategy during standard working hours (08:00–17:00). Under the static condition, the lamp operates at 100% intensity with a constant Direct Sunlight color throughout the working period, resulting in a total electrical energy consumption of 60 Wh.

In contrast, under the combined dynamic dimming and color control condition, the lamp operates at 50% intensity, with scheduled color variations (Warm White, Transition, and Direct Sunlight) applied across predefined time intervals. Under this configuration, the total electrical energy consumption is reduced to 42.7 Wh.

This represents an absolute energy saving of 17.3 Wh, corresponding to a relative reduction of approximately 28.83% compared to the static Direct Sunlight condition. The results demonstrate that the combined application of intensity-based dimming and dynamic color control yields a substantial reduction in electrical energy consumption.

TABLE IV. THE 4RD SCENARIO EXPERIMENT: DYNAMIC COLOR VS. COMBINED DYNAMIC DIMMING AND COLOR CONTROL

Percentage of Lights on	*Lamp Color*	*Time Range*	*Electric Energy Consumption (Wh)*
100%	Warm White	08-10 AM & 03-05 PM	22,4

Percentage of Lights on	*Lamp Color*	*Time Range*	*Electric Energy Consumption (Wh)*
	Transition	10-11 AM & 02-03 PM	10,8
	Direct Sunlight	11 AM – 02 PM	18
Total			51,2
50%	Warm White	08-10 AM & 03-05 PM	18
	Transition	10-11 AM & 02-03 PM	9,6
	Direct Sunlight	11 AM – 02 PM	15,1
Total			42,7
Light Power Saving			8,5
			16,6%

Table IV summarizes the electrical energy consumption of the lighting system under dynamic color operation and combined dynamic dimming and color control during standard working hours (08:00–17:00). Under the dynamic color condition with full lamp intensity (100%), the total electrical energy consumption was recorded at 51.2 Wh. This value represents the accumulated energy consumption across different color settings, namely Warm White, Transition, and Direct Sunlight, applied over their respective time intervals.

When combined dynamic dimming and color control was implemented, with the lamp operating at 50% intensity, the total electrical energy consumption decreased to 42.7 Wh. This corresponds to an absolute energy reduction of 8.5 Wh, equivalent to a relative energy saving of approximately 17% compared to the dynamic color-only condition.

These results indicate that while dynamic color adjustment contributes to visual and circadian lighting objectives, the addition of intensity-based dimming provides a further reduction in electrical energy consumption. The findings suggest that combining dimming control with color modulation is more effective in reducing overall lighting energy use than applying dynamic color control alone.

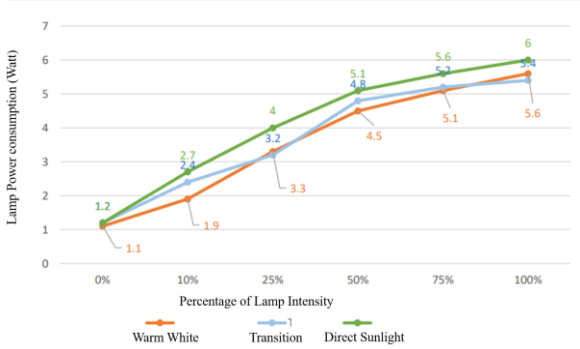

Fig. 10. Lamp Power Consumption Based on Color and Dimming Levels

Figure 10 illustrates the relationship between lamp power consumption and the percentage of lamp intensity for three color settings, namely Warm White, Transition, and Direct Sunlight. The results show that electrical power consumption increases monotonically with increasing lamp intensity for all color modes, indicating a consistent and predictable power–intensity relationship.

At low intensity levels (0–25%), the differences in power consumption among the three color settings are relatively small. At 0% intensity, the measured power ranges from approximately 1.1 W to 1.2 W, suggesting the presence of baseline power consumption associated with the control circuitry. As the intensity increases to 10% and 25%, the Direct Sunlight mode exhibits slightly higher power consumption (2.7 W and 4.0 W, respectively) compared to Transition and Warm White modes.

At medium to high intensity levels (50–100%), the divergence in power consumption among color settings becomes more pronounced. At 50% intensity, the measured power reaches 4.5 W for Warm White, 4.8 W for Transition, and 5.1 W for Direct Sunlight. This trend continues at 75% and 100% intensity, where Direct Sunlight consistently records the highest power consumption, reaching approximately 6.0 W at full intensity, while Warm White exhibits the lowest power consumption at approximately 5.6 W.

V. Conclusion

Survey results show that all respondents in the objected room occupants report experiencing drowsiness between 10:00 and 15:00. This condition is influenced by continuous static artificial lighting and variations in natural daylight, which together contribute to reduced alertness during these hours. Surveys indicated that 100% of occupants occasionally experienced drowsiness between 10 AM–3 PM due to static artificial lighting and dynamic sunlight.

Field observations revealed uneven natural light distribution in the room, despite meeting the recommended illuminance level (351–646.33 lux). Issues included five non-functional lamps and curtains obstructing natural light.

Dynamic dimming alone achieves energy savings of approximately 15%, while dynamic color modulation provides comparable reductions of about 14–15%. The combined application of dynamic dimming and color control yields the highest energy-saving performance, with reductions of up to approximately 29%. These findings indicate that integrating intensity-based dimming with color modulation is more effective than applying either strategy individually for reducing lighting energy consumption during working hours.

Although this work focuses on the development and energy performance evaluation of a dynamic lighting control system, a detailed assessment of the controller's performance characteristics, such as response time, stability, and tracking accuracy, has not yet been conducted. Future work will include a comprehensive evaluation of the control algorithm under varying lighting and occupancy conditions, as well as comparisons with alternative control strategies to further assess system robustness and performance.

ACKNOWLEDGMENT

The authors would like to thank the Institute of Research and Community Services (Research, Innovation & Sustainability Community Engagement), Universitas Multimedia Nusantara for sponsoring this paper in the scheme of Internal Research 2022.

REFERENCES

[1] M. Boubekri, I. N. Cheung, K. J. Reid, C.-H. Wang and P. C. Zee, "Impact of Windows and Daylight Exposure on Overall Health and Sleep Quality of Office Workers: A Case-Control Pilot Study," Journal of Clinical Sleep Medicine, vol. 10, no. 6, pp. 603-611, 2014.

[2] M. B. Aries, J. A. Veitch and G. R. Newsham, "Windows, View, and Office Characteristics Predict Physical and Psychological Discomfort," Journal of Environmental Psychology, vol. 30, pp. 533-541, 2010

[3] X. Chen, X. Zhang and J. Du, "Glazing Type (Colour and Transmittance), Daylighting, and Human Performances at A Workroom: A Full-Scale Experiment in Beijing," Building and Environment, vol. 153, pp. 168-185, 2019

[4] M. F. Culver, *"Sleep Interrupted: How Our Modern Life Affects Our Rhythm," EC Nutrition,* vol. 13, no. 5, pp. 250–259, **2018**.

[5] M. G. Figueiro, B. Steverson, J. Heerwagen, K. Kampschroer, C. M. Hunter, K. Gonzales, B. Plitnick and M. S. Rea, "The Impact of Daytime Light Exposures on Sleep and Mood in Office Workers," Sleep Health, vol. 3, pp. 204-215, 2017.

[6] M. Figueiro, M. Kalsher, B. Steverson, J. Heerwagen, K. Kampschroer and M. Rea, "Circadian-Effective Light and Its Impact on Alertness," The Society of Light and Lighting, vol. 0, pp. 1-13, 2018.

[7] X. Chen, X. Zhang and J. Du, "The Potential of Circadian Lighting in Office Buildings Using a Fibre Optics Daylighting System in Beijing," Building and Environment, vol. 182, p. 107118, 2020.

[8] L. Baandrup and P. J. Jennum , "Effect of A Dynamic Lighting Intervention on Circadian Rest-Activity Disturbances in Cognitively Impaired, Older Adults Living in A Nursing Home: A Proof-of-Concept Study," Neurobiology of Sleep and Circadian Rhythms, vol. 11, p. 100067, 2021.

[9] M. Ye, S. Zheng, M. Wang and M. R. Luo, "The Effect of Dynamic Correlated Colour Temperature Changes on Alertness and Performance," Lighting Research & Technology, vol. 0, pp. 1-12, 2018.

[10] M. H. R. Rahman, S. Sangadji, and S. A. Kristiawan, "Retrofitting thermal and lighting condition of a production warehouse," International Journal of Scientific & Technology Research, vol. 9, no. 4, pp. 867–871, 2020.

[11] C. Indriyati, A. Daud, and R. Prima, Analisis konservasi dan efisiensi energi pada Tower Fakultas Hukum Universitas Sriwijaya berdasarkan sertifikasi Green Building Indonesia, Syntax Literate: Jurnal Ilmiah Indonesia, vol. 6, no. 6, pp. 2662–2678, Juni 2021

[12] Fleischer, S.; Krueger, H. Effect of brightness distribution and light colours on office staff. Eur. Light. 2001.

[13] Rüger, M.; Gordijn, M.C.M.; Beersma, D.G.M.; de Vries, B.; Daan, S. Time-of-day-dependent effects of bright light exposure on human psychophysiology: Comparison of daytime and nighttime exposure. Am. J. Physiol. Regul. Integr. Comp. Physiol. 2006, 290, R1413–R1420.

ISSN 2355-3286

Predictive Control of Speed, Steering, and Braking for An Autonomous Car on Uphill and Downhill Road

Ryan Aditya[1], Ari Santoso[2]
[1,2] Department of Electrical Engineering, Institut Teknologi Sepuluh Nopember, Surabaya, Indonesia
[1]ryn.adty19@gmail.com

Accepted on November 13, 2025
Approved on December 30, 2025

***Abstract*— Countries around the world have roads that go through mountains and hills. These roads can have features such as winding and change of elevation. When passing through such roads, the car's dynamics are influenced by the unknown elevations and curvatures, which can threaten stability if not properly controlled. The purpose of this research is to control the cars longitudinal speed through acceleration, braking through regenerative braking and maintain lateral control through steering inputs. The proposed hierarchical control scheme consists of a high-level predictive controller which predicts the car's dynamics under varying road condition and a low-level Fuzzy-PID controller for the actuators, which is motor driver and electric power steering (EPS). Additionally, the energy recovery from the regenerative braking system is monitored to evaluate its impact on battery state of charge, especially when the car is slowing down or going through downhill roads. The control system proposed aims to maintain speed and steering stability under varying road conditions and improve energy efficiency. The simulation will be done using MATLAB and the car will go through a spiral down track and a U-turn ramp track. The proposed controller manages to track both the cars speed and acceleration under the present of roads curvature and downhill disturbance. The Fuzzy-PID also manage to track the reference generated by the NMPC with a slightly damped response. For the battery state of charge (SOC) there is a rise of 0.0025% or equivalent to 40 Wh generated from regenerative braking.**

***Index Terms*—Autonomous Car; Fuzzy-PID; Predictive Control; Regenerative Braking**

I. INTRODUCTION

An autonomous car is a vehicle that can operate on its own without human intervention. The purpose of autonomous car control research is mainly based on speed, which focuses on longitudinal dynamics and steering control for lateral dynamics. With the growing shift to electric motors and battery-powered systems for cars, more methods are developed for utilizing the motor's excessive mechanical energy by converting it back into electrical energy. This method is called regenerative braking and helps recharge the car's battery during deceleration[1], [2], [3].

The research on autonomous car control has been ongoing for quite a while now. In [4], an adaptive cruise control (ACC) combined with regenerative braking which uses two-layer control is developed. The first control layer consists of an adaptive fuzzy sliding mode control (AFSMC) and a low-level control brake system distribution control, mainly to manage force distribution between mechanical and regenerative brake. The proposed method is capable of accurately tracking the vehicle speed under various road conditions, including wet and dry surfaces.

In [5], the research aims to maintain stability with a combination of both mechanical and regenerative brakes. The proposed controller is a PI controller which output controls determine the ratio between mechanical and regenerative brake used when slowing down. Though this research only focuses on junction type roads. In [6], a sliding mode control (SMC) combined with performance guarantee (PG) was proposed to control the vehicles speed and steering. The PG method aims to keep the vehicle's state errors to converge to zero while constraining it within the determined limit. However, these studies have yet integrated all three elements of speed, steering and braking. Therefore, this study aims to fill that gap by combining these three elements.

Model predictive control (MPC) and its nonlinear variants (NMPC) have been applied extensively to vehicle steering, longitudinal control and integrated braking problems; [7] developed a robust predictive control of an autonomous car steering system for path-tracking using LMI optimization with independent constraints enforcement. Applications of NMPC for collision avoidance path planning and tracking control for autonomous vehicles have been demonstrated in [8]. Regenerative and mechanical brake integration have also been approached with predictive control for performance and energy recovery[9]. Fuzzy–PID and adaptive fuzzy controllers are widely used at actuator level to handle nonlinearities and reduce transient overshoot[10]. Finally, open-source toolchains (CasADi, IPOPT) and commercial environments (MATLAB/Simulink) are commonly used to

implement and test NMPC and the lower-level controllers used here[11], [12], [13].

In this work, we propose a hierarchical control scheme that consist of a high-level predictive control focusing on steering and speed control combined with a low-level Fuzzy-PID for the actuators control. The predictive control aims to achieve stability especially when moving through uphill, downhill, and winding roads while the Fuzzy-PID ensures smooth and precise actuation. When the car is slowing down, energy recovery generated from the regenerative braking and its impact on battery state of charge will also be monitored.

This paper is organized as follows: Section I outlines the background and other research related to autonomous car control. Section II describes the car mathematical model and the proposed controller design. Section III discusses the simulation result, focusing on the car's acceleration and steering control inputs, key state parameters and energy recovery via regenerative braking. Section IV contains the summary and conclusion of our research, while also providing direction for future work.

II. METHODOLOGY

A. Car Dynamic and Kinematic Model

The model provided by [14] captures both the longitudinal and the lateral dynamics, in addition a lateral and yaw angle error will be added to the model. The states will be formulated as follows:

$$x = [\dot{v}_x, v_x, v_y, \dot{\theta}, e_1, e_2, x_{od}]^T, u = [a, \delta]^T \quad (1)$$

$$y = [v_x, e_1, e_2 + x_{od}]^T \quad (2)$$

where $x_1 = \dot{v}_x$ is the longitudinal acceleration; $x_2 = v_x$ is the longitudinal speed; $x_3 = v_y$ is the lateral speed; $x_4 = \dot{\theta}$ is the car yaw angle speed; $x_5 = e_1$ is the lateral deviation; $x_6 = e_2$ is the relative yaw angle; and $x_7 = x_{od}$ is the longitudinal deviation. For the control input $u_1 = a$ and $u_2 = \delta$ are the car acceleration and steering respectively.

The car's longitudinal dynamic is simplified as a first order model, while the lateral dynamic model will contain some nonlinearities affected by the longitudinal speed. The model is described as follows:

$$\dot{x}_1 = \frac{1}{\tau}(-x_1 + u_1 + d_1) \quad (3)$$

$$\dot{x}_2 = x_1 + x_3 x_4 \quad (4)$$

$$\dot{x}_3 = \frac{1}{m}(F_{y12} + F_{y34}) - x_2 x_4 \quad (5)$$

$$\dot{x}_4 = \frac{1}{I_z}\left(l_f F_{y12} - l_r F_{y34}\right) \quad (6)$$

The cars mass and inertia are respectively m and I_z. The cars time constant is denoted as τ. The lateral tire forces are denoted as F_y, where subscripts 1,2 refer to the front tire and 3,4 the rear tire. The tire forces for the front side will be considered equal on both side, this also apply to the rear side. The car wheels distance from the center gravity are l_f for the front wheels and l_r for the rear wheels.

$$F_{y12} = u_2 - C_{af}\frac{x_3 + l_f x_4}{x_1} \quad (7)$$

$$F_{y34} = -C_{ar}\frac{x_3 - l_r x_4}{x_1} \quad (8)$$

The wheels cornering stiffness are denoted as C_a, where the subscripts f, r refer to the front and rear tires. The error model for both lateral and yaw angle deviation are defined accordingly:

$$\dot{x}_5 = x_3 + x_2 x_6 \quad (9)$$

$$\dot{x}_6 = x_4 - x_2 \rho \quad (10)$$

the disturbance term d_1 represents the roads gradient on the longitudinal axis, while ρ denotes the road's curvature value. Finally, the car kinematics will be captured with the bicycle model as follows:

$$\begin{bmatrix}\dot{x}\\ \dot{y}\\ \dot{\theta}\end{bmatrix} = \begin{bmatrix}v\cos\theta\\ v\sin\theta\\ \frac{v}{L}\tan\delta\end{bmatrix} \quad (11)$$

Where θ is the car yaw angle, δ is the steering angle, v is the car speed and L is the distance between the front and back wheel.

B. Nonlinear Model Predictive Control

Model Predictive Control is a feedback digital feedback control method with the ability to predict the system's output within the desired horizon. This prediction is calculated virtually inside the controller based on the system mathematical model and the control output then produced through cost function calculations[15]. Refer to [16], [17] for general MPC references for theory and design.

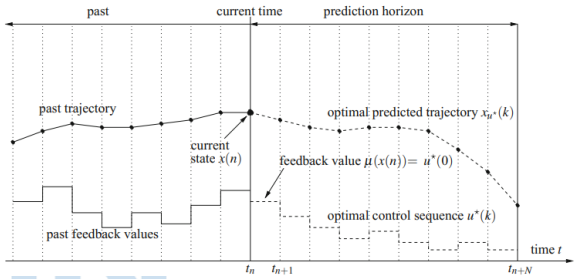

Fig. 1 Nonlinear predictive control scheme

For Nonlinear Model Predictive Control (NMPC), the system model is formulated as:

$$x^+ = f(x, u) \quad (12)$$

where f is the nonlinear function of the model with state x and input u while x^+ indicates the future state value. The predicted state x_u can be obtained by iterating equation (14) between the horizon N.

$$x_u(0) = x(n) \quad (13)$$

$$x_u(k+1) = f\big(x_u(k), u(k)\big), k = 0, \dots, N-1 \quad (14)$$

The control value obtained from the state x_u is then calculated through a cost function formulated as follows:

$$J\big(x(n), u(n)\big) = \sum_{k=0}^{N-1}\|x_u(k)\|^2 + \lambda\|u(k)\|^2 \quad (15)$$

where λ is a weighing value for smooth control command. Constraints can also be used to describe practical hardware limitations. This ensures the optimal control generated by the NMPC is feasible for physical realization. Lastly, the NMPC produce the control sequences necessary based on the prediction N for

every time interval[18]. The NMPC will act as a high-level controller and generate a reference for the actuators to track on.

C. *Fuzzy-PID*

Nonlinearities on practical dynamic systems limit the peformance of a regular PID controllers. Therefore, a PID control can be combined with a fuzzy control scheme to overcome this nonliearities. The gains K_p, K_i, K_d combined with fuzzy logic can now vary depending on the error and error rate of the system[10].

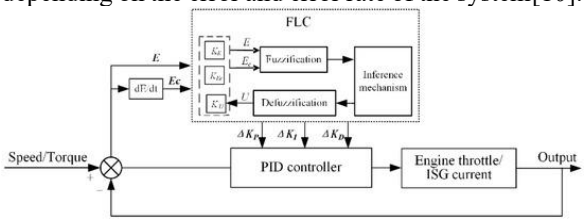

Fig. 2 Example of Fuzzy-PID control scheme

The three main stages of Fuzzy-PID implemantation are; fuzzification, where the error data (typically error and error rate) are mapped into fuzzy sets through the use of membership functions; fuzzy inference, where a rule base system combines the inputs to calculate the fuzzy control values; defuzzification, which converts the fuzzy control back to a crisp tuning of PID gains for final control calculation[19]. The Fuzzy-PID will be in charge of controlling the low-level actuators which are the motor drive for the car speed control and the electric power steering (EPS) for the car steering control.

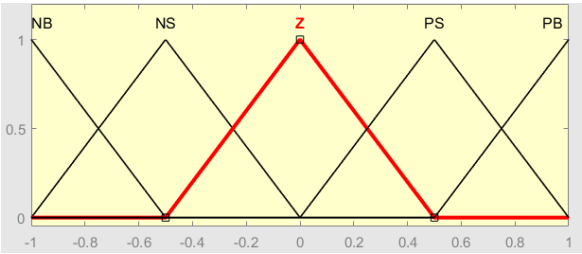

Fig. 3 Input Membership Function Structure Example

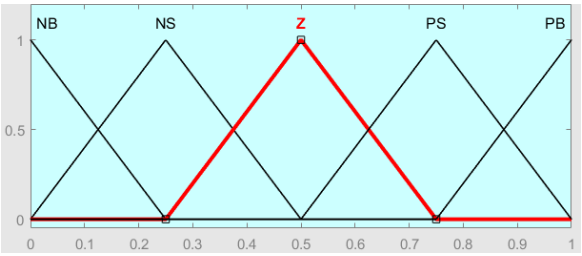

Fig. 4 Output Membership Function Structure Example

For this Fuzzy-PID controller, identical fuzzy membership functions is applied for all PID gain components. Specifically, the membership functions associated with the proportional, integral, and derivative gains are defined with the same number of linguistic terms, uniform widths, and symmetric distributions. This design choice is adopted to maintain consistency of the actuator control and reduce tuning complexity. An example of the input membership functions can be seen in Figure 3. which contains five overlapping fuzzy sets, namely Negative Big (NB), Negative small (NS), Zero (Z), Positive Small (PS), and Positive Big (PB). The same is also applied to the output membership functions shown in Figure 4. Even though the membership functions show similarity, there is a key difference which is the variable range. The input variables (actuators error and error rate) are normalized over the range of $[-1,1]$, this allows the Fuzzy-PID to process both positive and negative error values. In contrast the fuzzy outputs represent scaling factors for the PID gains and constrained to the interval of $[0,1]$, this allows a simpler tuning for each gain since the main proportional, integral and derivatives gain are outside the fuzzy membership functions. The rule sets for each gain are shown on Table 1-3.

TABLE I. PROPORTIONAL GAIN (KP) RULE SET

de/e	NB	NS	Z	PS	PB
NB	PB	PS	Z	NS	NB
NS	PS	PS	Z	NS	NS
Z	Z	Z	Z	Z	Z
PS	NS	NS	Z	PS	PS
PB	NB	NS	Z	PS	PB

TABLE II. INTEGRAL GAIN (KI) RULE SET

de/e	NB	NS	Z	PS	PB
NB	NB	NB	NB	Z	Z
NS	NB	NS	Z	PS	Z
Z	NS	Z	Z	Z	PS
PS	Z	PS	Z	PS	PB
PB	Z	Z	PS	PB	PB

TABLE III. DERIVATIVE GAIN (KD) RULE SET

de/e	NB	NS	Z	PS	PB
NB	NS	Z	PS	PB	PB
NS	Z	PS	PS	PB	PB
Z	PS	PB	Z	PS	PB
PS	PB	PB	NS	Z	PS
PB	PB	PB	NS	Z	NS

TABLE IV. ACTUATOR FUZZ-PID GAINS

Gain	Motor Drive	EPS
Kp	5	15
Ki	1	5
Kd	1	4

D. Energy Recovery

Regenerative braking will be used as the main source of the battery energy recovery. During the regenerative braking the motor will act as a generator, excess kinetic energy will be converted back into electrical energy through electromagnetic torque. The motor in this research will be used for both propulsion and regenerative braking. Therefore, a condition is needed to distinguish propulsion mode and regenerative braking mode. For propulsion mode the conditions are:

$$T_m < T_e \; and \; I_m > 0 \quad (16)$$

and for generator mode:

$$T_m > T_e \; and \; I_m < 0 \quad (17)$$

The electrical and mechanical torque of the motor are denoted as T_m and T_e, while I_m is the motor current. When these conditions are met the battery will be allowed to charge. The battery will only be monitored on charging mode, so the system will be modelled as follows:

$$P_b = \eta_m \eta_p T_m \omega_m \quad (18)$$

and the state of charge (SOC) is modelled as follows:

$$\frac{d}{dt}(SOC) = -\eta_{bchg} \frac{I}{Q_b} \quad (19)$$

$$I = \frac{V_{oc} - \sqrt{V_{oc}^2 - 4R_{int}P_b}}{2R_{int}} \quad (20)$$

Where η_m,η_p,η_{bchg} are respectively the efficiency of the motor, electrical circuit and battery charging. The motor torque and speed are denoted as T_m and ω_m, the battery voltage is V_{oc}, the battery internal resistance is R_{int} and Q_b is the battery capacity[4, 20].

III. Results and Discussion

The simulations are carried out in MATLAB, where the main focus will be steering and speed control. Energy regeneration will also be monitored due to the car slowing down on the downhill road. The track used for simulation will be a downward circle track and U-turn ramp, which will capture both the steering and the disturbance produced by the change of gradient and curving roads. The car system and hierarchical control scheme for the simulation will be constructed as in Figure 5, where the NMPC will act as high-level planner and the Fuzzy-PID will control both the motor and steering actuator. Afterward the output generated by both actuators will be fed into the car model.

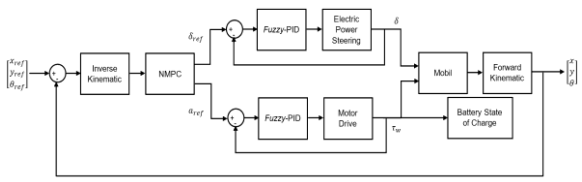

Fig. 5. System block diagram

The sampling time for the NMPC will be 0.1 seconds. The prediction horizon of the NMPC is set to 10 steps ahead and the control horizon 2 steps ahead. There are also some constraints given for the speed (21) and steering control (22) reference that will be given to the actuators as follows:

$$-3 < a < 3 \text{ (m/s)} \quad (21)$$

$$-0.5 < \delta < 0.5 \text{ (rad)} \quad (22)$$

The acceleration constraints represent typical passenger-vehicle acceleration and deacceleration capability without requiring extreme actuator effort. This range also allows normal and reasonably aggressive speed changes. The steering angle constraint refers to the front-wheel steering angle, which is a typical front wheel turning angle. The battery internal circuit will also be considered ideal so the heat generated from it won't affect the battery charging. This assumption helps simplify modelling and reduce computational complexity. Conditions (17) will be used as a basic ON-OFF trigger for charging the battery. Some of the parameters used on the simulation are mentioned in Table 5 and Table 6.

TABLE V. CAR PARAMETERS

Parameter	Value
Mass (m)	1575 (kg)
Moment of inertia (I_z)	2875 ($kg.m^2$)
Front wheels distance (L_f)	1.2 (m)
Rear wheels distance (L_r)	1.6 (m)
Front wheels cornering stiffness (C_{af})	19000 (N/rad)
Rear wheels cornering stiffness (C_{ar})	33000 (N/rad)
Time constant (τ)	0.2 (s)

TABLE VI. BATTERY PARAMETERS

Parameter	Value
Motor efficiency	0.85
Circuit efficiency	0.96
Battery efficiency	0.9
Battery voltage	60%
Battery Capacity	18 kWh
Internal resistance	0.025 (Ω)

A. *Spiral Down Track*

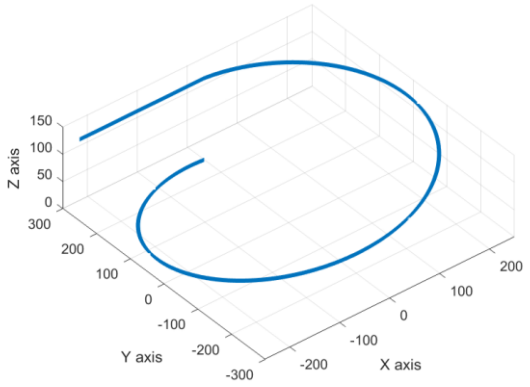

Fig. 6. Spiral down track preview

The track starts with a 250 m straight road as shown in Figure 6. then circling down on a track with 250 m radius. The starting height will be 150 m therefore the car will be going downhill with a slope of 2.7°. The car will try to maintain a constant speed of 8.33 m/s or equivalent to 30 km/h from start until going downhill while doing a turn. The simulation ends after going through a full circular track.

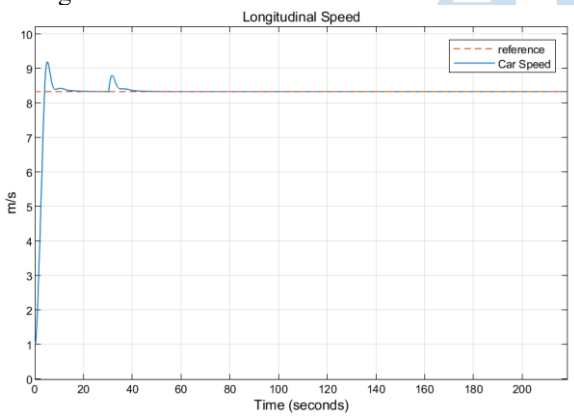

Fig. 7. Spiral down track longitudinal speed

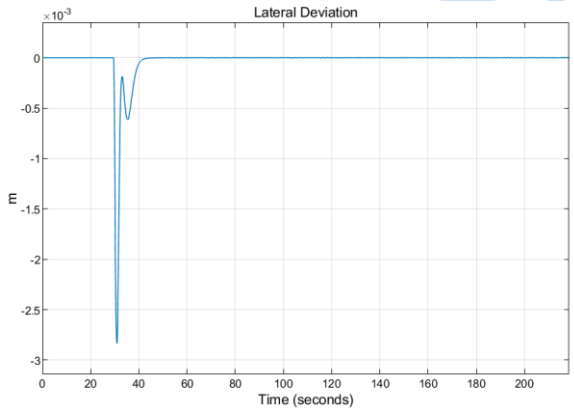

Fig. 8. Spiral down track lateral deviations

Figure 7. presents the car longitudinal speed, where the speed reach around 8.33 m/s on steady-state which is equivalent to 30 km/h. There are two overshoots observed from the simulation result. First is during the initial acceleration with a peak value of around 9% before settling. This can be caused by a small lag between the actuator's responses and the NMPC reference. Integrating the actuator dynamic directly might solved this problem, but the low-level control contains a Fuzzy-PID. Therefore, a new problem arises to integrate the low-level control loop into the NMPC.

The second overshoot occurs when the car starts to turn after going straight for 250 m with a peak value of around 5% before settling again. This overshoot might be caused by the combination of both the road turning and going downward happening at the same time. The lack of smoothness generated from the track waypoints also affects the transient response of the system, causing some minor overshoot along the way.

Figure 8. presents both the lateral deviation throughout the motion. At the start of the turn, the lateral deviation shows a brief negative spike, which indicates that the vehicle initially drifts slightly toward the inside of the curve. This spike is short-lived and is corrected rapidly, the controller brings the deviation back toward zero within around 10 seconds. Such behaviour typically arises from curvature changes. The swift return to near-zero value suggest that the controller maintains stability even under the presents of disturbance.

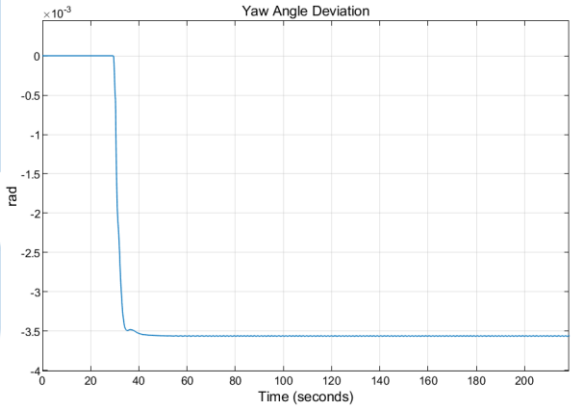

Fig. 9. Spiral down track yaw angle deviations

The yaw angle deviation plot from Figure 9. shows a small but consistent offset between the vehicle's heading and the tangent direction of the track. This indicates that the vehicle follows a slightly different curvature than the reference arc. Even so, the deviation remains very small around the order of 10^{-3} rad, meaning the vehicle's trajectory is effectively parallel to the desired path with only a negligible angular error.

Together, the lateral and yaw angle responses demonstrate that while the vehicle temporarily experiences a small disturbance at the start of the turn, the controller quickly stabilizes the motion and preserves accurate path following. The magnitude of both deviations is extremely small, showing that the proposed controller is capable of maintaining smooth

and stable lateral behaviour even in the present of curvature changes and under the influence of other external factors such as roadway slope.

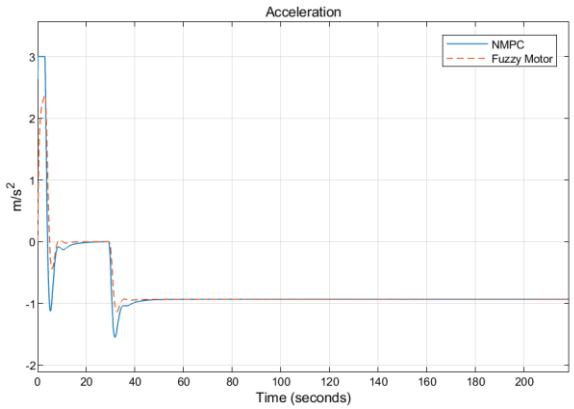

Fig. 10. Spiral down track motor acceleration tracking control

Figure 10. compares the acceleration reference generated from the NMPC (blue line) with the actual acceleration generated by the motor controlled with the Fuzzy-PID (orange-dashed line). The results show that the proposed inner-loop controller is able to track the NMPC reference acceleration with good fidelity, particularly once the acceleration reaches steady-state. During the transient phase, small differences between the reference signal and the actuator response are noticeable. These deviations occur primarily during two key periods: the initial acceleration to the desired speed and when the car start going through a downhill.

At the beginning of the motion, the NMPC demands a relatively high positive acceleration to rapidly bring the vehicle up to the target reference speed. This aggressive command is expected, as the NMPC optimizes speed tracking while respecting the system's constraints. In contrast, the Fuzzy-PID controller damps out excessive acceleration, which result in slightly slower rise in acceleration. Despite this small difference, the vehicle still reaches the desired velocity with minimal overshoot, as confirmed earlier in Figure 5. A similar behaviour occurs when the vehicle goes through a downhill. The NMPC lowers the reference by providing negative acceleration to maintain the desired speed under the effect of the road gradient. The Fuzzy-PID controller once again produce a slightly damped output. Even so, the difference remains small and the actuator consistently converges toward the NMPC output reference once it reaches steady-state.

The close alignment between the two responses in the steady-state region demonstrates effective coordination between the high-level NMPC and the low-level Fuzzy-PID control. The small transient difference does not translate into notable speed tracking errors, indicating that the combined control structure is able to overcome minor delays. In practice, this behaviour is desirable because it prevents excessive torque application, reduces mechanical stress on drivetrain components, and enhances ride comfort.

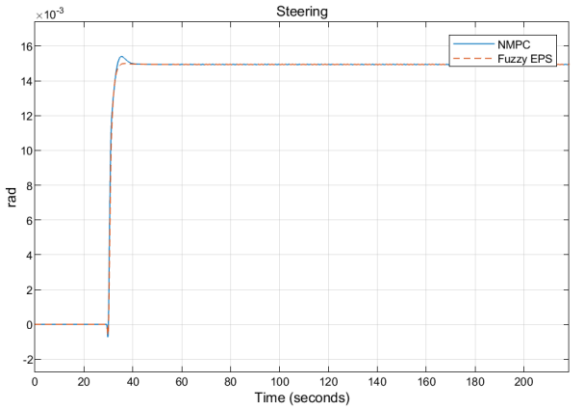

Fig. 11. Spiral down track electric power steering tracking control

The comparison between the NMPC reference (blue line) and the Fuzzy-PID controlled EPS is shown in Figure 11. Both signals converge to a steady-state value of approximately 0.015 rad, which is consistent with the curvature required to follow the reference turn. Although the final values match closely, several important transient characteristics can be observed during the motion. As the vehicle approaches the start of the turn, the steering reference generated by the NMPC contains another brief overshoot, similar to the phenomenon can be seen in the motor acceleration response in Figure 10.

On the actuator side, the Fuzzy-PID controller once again outputs a smoother and more damped steering response. While the NMPC produces another aggressive reference, the Fuzzy-PID for the EPS response slightly slower resulting less overshoot with similar output results. The smoothing effect is beneficial from a practical standpoint, as it reduces mechanical stress on the steering actuator. Once again, despite the small difference between the reference and the EPS steering angle, the EPS output still remains within the NMPC's imposed steering constraint and doesn't produce significant tracking errors. This is also confirmed by the previous lateral and yaw angle deviations shown in Figure 8. and Figure 9. Respectively. Overall, the steering results demonstrate another effective coordination between the NMPC and the Fuzzy-PID controller. The combination leads to stable and accurate path tracking, with the NMPC providing predictive steering command reference and the Fuzzy-PID controller ensures smooth, physically realizable actuation behaviour even when encountering non-smooth waypoints transitions.

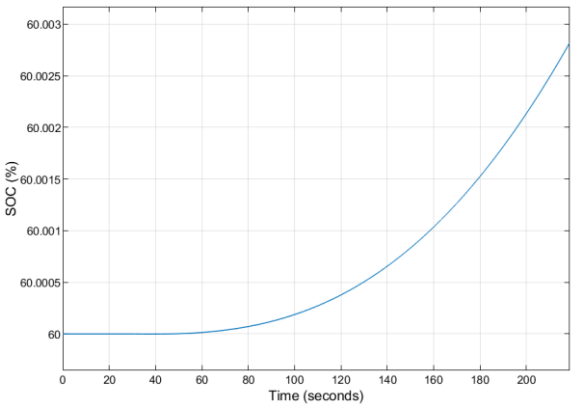

Fig. 12. Spiral down track battery state of charge

Figure 12. illustrates the battery SOC throughout the downhill track of the simulation. Although the absolute change in the battery's SOC is relatively small, the curve indicates a gradual increase in stored energy due to the activation of regenerative braking during the descent. Over 220 seconds of downhill, the SOC rises by approximately 0.0025% relative to its initial state. Based on the battery's nominal capacity and voltage parameters, this amount is equivalent to around 40 Wh of energy. While the value may appear small, it is physically consistent with the limited length of the simulation and the gradient of the slope used on the track in the scenario.

It is important to note that in this research, the model only monitor the charging aspect of the battery and ignore any discharge activity. This assumption allows the SOC curve to represent only the recovered energy, without the cofounding effect of other devices energy draw. As such, the SOC profile shown on Figure 10. should be interpreted as the maximum possible recovery within the defined scenario. Another important note is the integration of mechanical brake has not yet been done in this research. Overall, the soc behaviour confirms that the system responds appropriately to downhill disturbance by converting excess mechanical energy from the motor into stored electrical energy.

B. U-Turn Ramp Track

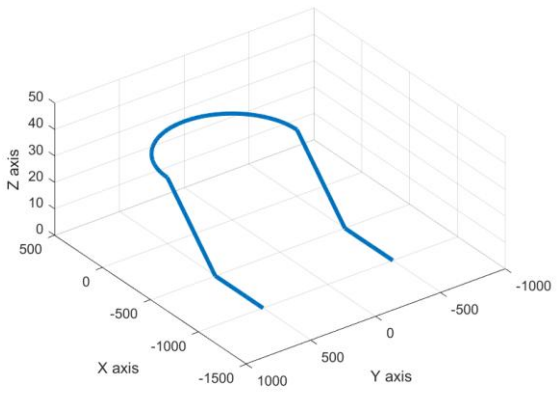

Fig. 13. U-turn ramp track preview

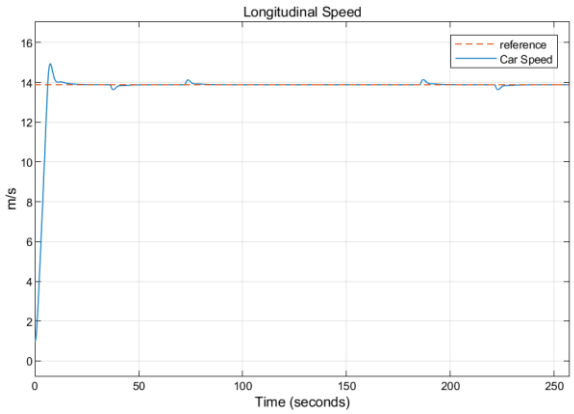

Fig. 14. U-turn ramp track longitudinal speed

For the second experiment, a U-turn combined with a ramp will be used. The track starts and ends with a 500 m straight road as shown in Figure 10. while the turn is half a circle with a radius of 500 m. Both of the ramps will have a length of 500 m and a slope of 2.86°. The car will try to maintain a constant speed of 13.88 m/s or equivalent to 50 km/h from start until finish. This will highlight both the dynamic of going uphill and downhill while also doing a turn. Figure 14. shows the longitudinal speed for the U-turn ramp track, where the speed reach around 13.88 m/s on steady-state which is equivalent to 50 km/h. There are one overshoot and 4 small bumps observed from the simulation result. First is the same during the initial acceleration with a peak value of around 9% before settling. The four overshoots occurs when the car starts and finish going through both downhill and uphill before settling again. This overshoot might be caused by the sudden change of road gradients. The negative small bumps indicate the car slows down, the first small bump is when the car is going uphill and the second one is when the car trying to slow down after going downhill. In the contrast, the positive bumps indicate the cars speeds up due to the change of road gradient, first is after finishing the uphill and later after entering downhill motion. This shows the controller able to counter the effect of road gradients with small errors.

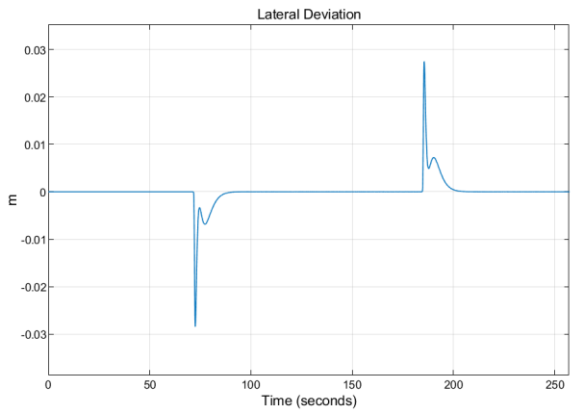

Fig. 15. U-turn ramp track lateral deviation

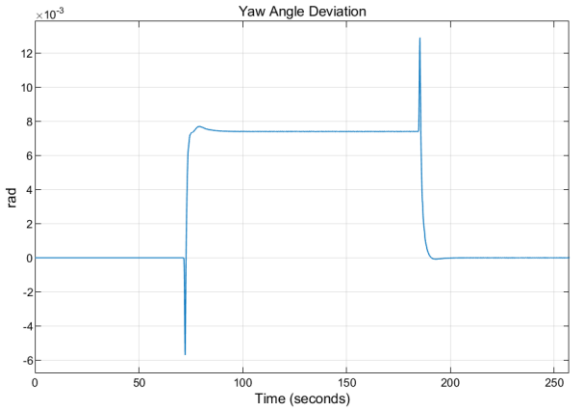

Fig. 16 U-turn ramp track yaw angle deviation

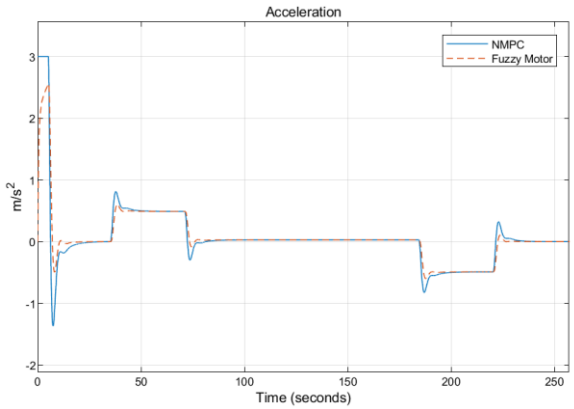

Fig. 17. U-turn ramp track acceleration tracking control

The deviations from Figure 15. and Figure 16. shows the car going through the U-turn segment. Similar spikes show at the start and the end of the turn which can be seen on Figure 8. And Figure 9. before. This is the effect of the non-smooth trajectory generated for the turning motion. Though the deviations are short lived and quickly corrected by the controller. The acceleration tracking for this track is shown in Figure 17. The cars acceleration shows the same profile as the longitudinal speed on Figure 14. There are four bumps each when starting and finishing both downhill and uphill motion. The control scheme still manages to track the acceleration even on the present of the uphill motion. Lastly, the controller also manages to track the cars steering before and after going through an uphill and downhill motion as shown in Figure 18.

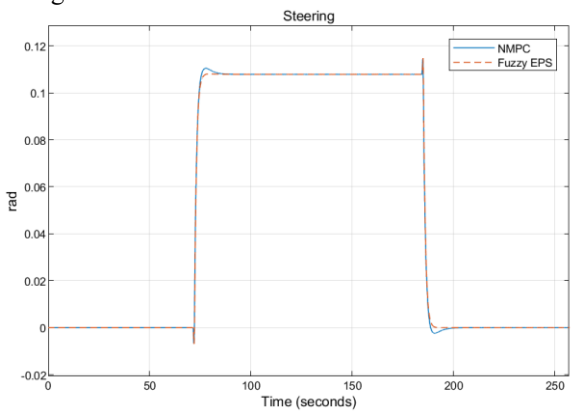

Fig. 18. U-turn ramp track steering tracking control

IV. Conclusion

The hierarchical control scheme—comprising an NMPC high-level planner and Fuzzy-PID low-level actuator controller—successfully maintained vehicle stability through both speed and steering control even under the presence of disturbance such as curving road, uphill road and downhill road. The Fuzzy-PID manages to damp the overshoot generated from NMPC setpoint reference which is likely caused by non-smooth waypoint generation and the absence of actuator dynamics on the NMPC model. The motor is also able to generate a small amount of charge which is 0.0025% or equivalent to 40 Wh. Overall, the results show effective coordination between the NMPC and the Fuzzy-PID. Future work should focus on optimizing waypoint generation for low-jerk trajectories and incorporating actuator dynamics into the NMPC model.

References

[1] P. Saiteja, B. Ashok, A. S. Wagh, and M. E. Farrag, “Critical review on optimal regenerative braking control system architecture, calibration parameters and development challenges for EVs,” Int J Energy Res, vol. 46, no. 14, pp. 20146–20179, Nov. 2022, doi: 10.1002/er.8306.

[2] A. T. Hamada and M. F. Orhan, “An overview of regenerative braking systems,” J Energy Storage, vol. 52, p. 105033, Aug. 2022, doi: 10.1016/J.EST.2022.105033.

[3] Q. Chengqun et al., “A novel regenerative braking energy recuperation system for electric vehicles based on driving style,” Energy, vol. 283, p. 129055, Nov. 2023, doi: 10.1016/J.ENERGY.2023.129055.

[4] J. Guo, W. Li, J. Wang, Y. Luo, and K. Li, “Safe and Energy-Efficient Car-Following Control Strategy for Intelligent Electric Vehicles Considering Regenerative Braking,” IEEE Transactions on Intelligent Transportation Systems, vol. 23, no. 7, pp. 7070–7081, Jul. 2022, doi: 10.1109/TITS.2021.3066611.

[5] C. S. Nanda Kumar and S. C. Subramanian, “Brake force sharing to improve lateral stability while regenerative braking in a turn,” Proceedings of the Institution of Mechanical Engineers, Part D: Journal of Automobile Engineering, vol. 233, no. 3, pp. 531–547, Feb. 2019, doi: 10.1177/0954407017747373.

[6] H. Xia, J. Chen, F. Lan, and Z. Liu, “Motion Control of Autonomous Vehicles with Guaranteed Prescribed Performance,” Int J Control Autom Syst, vol. 18, no. 6, pp. 1510–1517, Jun. 2020, doi: 10.1007/s12555-019-0442-5.

[7] N. N. Nam and K. Han, "Path-tracking Robust Model Predictive Control of an Autonomous Steering System Using LMI Optimization With Independent Constraints Enforcement," Int J Control Autom Syst, vol. 22, no. 11, pp. 3352–3363, 2024, doi: 10.1007/s12555-023-0772-1.

[8] D. Dong, H. Ye, W. Luo, J. Wen, and D. Huang, "Collision Avoidance Path Planning and Tracking Control for Autonomous Vehicles Based on Model Predictive Control," Sensors, vol. 24, no. 16, Aug. 2024, doi: 10.3390/s24165211.

[9] M. Mei, S. Cheng, H. Mu, Y. Pei, and B. Li, "Switchable MPC-based multi-objective regenerative brake control via flow regulation for electric vehicles," Front Robot AI, vol. 10, Feb. 2023, doi: 10.3389/frobt.2023.1078253.

[10] P. Mohindru, "Review on PID, fuzzy and hybrid fuzzy PID controllers for controlling non-linear dynamic behaviour of chemical plants," Artificial Intelligence Review 2024 57:4, vol. 57, no. 4, pp. 97-, Mar. 2024, doi: 10.1007/S10462-024-10743-0.

[11] M. Bloor et al., "PC-Gym: Benchmark Environments For Process Control Problems," Dec. 2024, [Online]. Available: http://arxiv.org/abs/2410.22093

[12] S. W. Jannah and A. Santoso, "Nonlinear Model Predictive Control for Longitudinal and Lateral Dynamic of Autonomous Car," in Proceedings - 11th Electrical Power, Electronics, Communications, Control, and Informatics Seminar, EECCIS 2022, Institute of Electrical and Electronics Engineers Inc., 2022, pp. 145–148. doi: 10.1109/EECCIS54468.2022.9902927.

[13] R. Verschueren et al., "acados—a modular open-source framework for fast embedded optimal control," Math Program Comput, vol. 14, no. 1, pp. 147–183, 2022, doi: 10.1007/s12532-021-00208-8.

[14] R. Rajamani, Vehicle Dynamics and Control, 2nd ed. Berlin: Springer, 2011. doi: 10.1007/978-1-4614-1433-9.

[15] R. C. Rafaila and G. Livint, "Nonlinear model predictive control of autonomous vehicle steering," in 2015 19th International Conference on System Theory, Control and Computing, ICSTCC 2015 - Joint Conference SINTES 19, SACCS 15, SIMSIS 19, Institute of Electrical and Electronics Engineers Inc., Nov. 2015, pp. 466–471. doi: 10.1109/ICSTCC.2015.7321337.

[16] J. B. Rawlings, D. Q. Mayne, and M. M. Diehl, "Model Predictive Control: Theory, Computation, and Design 2nd Edition." [Online]. Available: http://www.nobhillpublishing.com

[17] D. Q. Mayne, J. B. Rawlings, C. V Rao, and P. O. M. Scokaert, "Survey Paper Constrained model predictive control: Stability and optimality."

[18] L. Grüne and J. Pannek, "Communications and Control Engineering Nonlinear Model Predictive Control Theory and Algorithms Second Edition." [Online]. Available: http://www.springer.com/series/61

[19] H. Qin, L. Wang, S. Wang, W. Ruan, and F. Jiang, "A Fuzzy Adaptive PID Coordination Control Strategy Based on Particle Swarm Optimization for Auxiliary Power Unit," Energies 2024, Vol. 17, Page 5311, vol. 17, no. 21, p. 5311, Oct. 2024, doi: 10.3390/EN17215311.

[20] Q. He, Y. Yang, C. Luo, J. Zhai, R. Luo, and C. Fu, "Energy recovery strategy optimization of dual-motor drive electric vehicle based on braking safety and efficient recovery," Energy, vol. 248, p. 123543, Jun. 2022, doi: 10.1016/J.ENERGY.2022.123543.

AUTHOR GUIDELINES

1. Manuscript criteria

- The article has never been published or in the submission process on other publications.
- Submitted articles could be original research articles or technical notes.
- The similarity score from plagiarism checker software such as Turnitin is 20% maximum.
- For December 2021 publication onwards, Ultima Computing : Jurnal Sistem Komputer will be receiving and publishing manuscripts written in English only.

2. Manuscript format

- Article been type in Microsoft Word version 2007 or later.
- Article been typed with 1 line spacing on an A4 paper size (21 cm x 29,7 cm), top-left margin are 3 cm and bottom-right margin are 2 cm, and Times New Roman's font type.
- Article should be prepared according to the following author guidelines in this template. Article contain of minimum 3500 words.
- References contain of minimum 15 references (primary references) from reputable journals/conferences

3. Organization of submitted article

The organization of the submitted article consists of Title, Abstract, Index Terms, Introduction, Method, Result and Discussion, Conclusion, Appendix (if any), Acknowledgment (if any), and References.

- Title
  The maximum words count on the title is 12 words (including the subtitle if available)
- Abstract
  Abstract consists of 150-250 words. The abstract should contain logical argumentation of the research taken, problem-solving methodology, research results, and a brief conclusion.
- Index terms
  A list in alphabetical order in between 4 to 6 words or short phrases separated by a semicolon (;), excluding words used in the title and chosen carefully to reflect the precise content of the paper.
- Introduction
  Introduction commonly contains the background, purpose of the research, problem identification, research methodology, and state of the art conducted by the authors which describe implicitly.
- Method
  Include sufficient details for the work to be repeated. Where specific equipment and materials are named, the manufacturer's details (name, city and country) should be given so that readers can trace specifications by contacting the manufacturer. Where commercially available software has been used, details of the supplier should be given in brackets or the reference given in full in the reference list.
- Results and Discussion
  State the results of experimental or modeling work, drawing attention to important details in tables and figures, and discuss them intensively by comparing and/or citing other references.
- Conclusion
  Explicitly describes the research's results been taken. Future works or suggestion could be explained after it
- Appendix and acknowledgment, if available, could be placed after Conclusion.
- All citations in the article should be written on References consecutively based on its' appearance order in the article using Mendeley (recommendation). The typing format will be in the same format as the IEEE journals and transaction format.

4. Reviewing of Manuscripts

Every submitted paper is independently and blindly reviewed by at least two peer-reviewers. The decision for publication, amendment, or rejection is based upon their reports/recommendations. If two or more reviewers consider a manuscript unsuitable for publication in this journal, a statement explaining the basis for the decision will be sent to the authors within six months of the submission date.

5. Revision of Manuscripts

Manuscripts sent back to the authors for revision should be returned to the editor without delay (maximum of two weeks). Revised manuscripts can be sent to the editorial office through the same online system. Revised manuscripts returned later than one month will be considered as new submissions.

6. Editing References

- **Periodicals**
  J.K. Author, “Name of paper,” Abbrev. Title of Periodical, vol. x, no. x, pp. xxx-xxx, Sept. 2013.

- **Book**
  J.K. Author, “Title of chapter in the book,” in Title of His Published Book, xth ed. City of Publisher, Country or Nation: Abbrev. Of Publisher, year, ch. x, sec. x, pp xxx-xxx.

- **Report**
  J.K. Author, “Title of report,” Abbrev. Name of Co., City of Co., Abbrev. State, Rep. xxx, year.

- **Handbook**
  Name of Manual/ Handbook, x ed., Abbrev. Name of Co., City of Co., Abbrev. State, year, pp. xxx-xxx.

- **Published Conference Proceedings**
  J.K. Author, “Title of paper,” in Unabbreviated Name of Conf., City of Conf., Abbrev. State (if given), year, pp. xxx-xxx.

- **Papers Presented at Conferences**
  J.K. Author, “Title of paper,” presented at the Unabbrev. Name of Conf., City of Conf., Abbrev. State, year.

- **Patents**
  J.K. Author, “Title of patent,” US. Patent xxxxxxx, Abbrev. 01 January 2014.

- **Theses and Dissertations**
  J.K. Author, “Title of thesis,” M.Sc. thesis, Abbrev. Dept., Abbrev. Univ., City of Univ., Abbrev. State, year. J.K. Author, “Title of dissertation,” Ph.D. dissertation, Abbrev. Dept., Abbrev. Univ., City of Univ., Abbrev. State, year.

- **Unpublished**
  J.K. Author, “Title of paper,” unpublished. J.K. Author, “Title of paper,” Abbrev. Title of Journal, in press.

- **On-line Sources**
  J.K. Author. (year, month day). Title (edition) [Type of medium]. Available: http:// www.(URL) J.K. Author. (year, month). Title. Journal [Type of medium]. volume(issue), pp. if given. Available: http://www.(URL) Note: type of medium could be online media, CD-ROM, USB, etc.

7. Editorial Adress

Jl. Scientia Boulevard, Gading Serpong
Tangerang, Banten, 15811
Email: **ultimacomputing@umn.ac.id**

Paper Title

Subtitle (if needed)

Author 1 Name[1], Author 2 Name[2], Author 3 Name[2]
[1] Line 1 (of affiliation): dept. name of organization, organization name, City, Country
Line 2: e-mail address if desired
[2] Line 1 (of affiliation): dept. name of organization, organization name, City, Country
Line 2: e-mail address if desired

Accepted on mmmmm dd, yyyy
Approved on mmmmm dd, yyyy

***Abstract*—This electronic document is a "live" template which you can use on preparing your Ultima Computing paper. Use this document as a template if you are using Microsoft Word 2007 or later. Otherwise, use this document as an instruction set. Do not use symbol, special characters, or Math in Paper Title and Abstract. Do not cite references in the abstract.**

***Index Terms*—enter key words or phrases in alphabetical order, separated by semicolon (;)**

I. INTRODUCTION

This template, modified in MS Word 2007 and saved as a Word 97-2003 document, provides authors with most of the formatting specifications needed for preparing electronic versions of their papers. Margins, column widths, line spacing, and type styles are built-in here. The authors must make sure that their paper has fulfilled all the formatting stated here.

Introduction commonly contains the background, purpose of the research, problem identification, and research methodology conducted by the authors which been describe implicitly. Except for Introduction and Conclusion, other chapter's title must be explicitly represent the content of the chapter.

II. EASE OF USE

A. Selecting a Template

First, confirm that you have the correct template for your paper size. This template is for Ultima Computing. It has been tailored for output on the A4 paper size.

B. Maintaining the Integrity of the Specifications

The template is used to format your paper and style the text. All margins, column widths, line spaces, and text fonts are prescribed; please do not alter them.

III. PREPARE YOUR PAPER BEFORE STYLING

Before you begin to format your paper, first write and save the content as a separate text file. Keep your text and graphic files separate until after the text has been formatted and styled. Do not add any kind of pagination anywhere in the paper. Please take note of the following items when proofreading spelling and grammar.

A. Abbreviations and Acronyms

Define abbreviations and acronyms the first time they are used in the text, even after they have been defined in the abstract. Abbreviations such as IEEE, SI, MKS, CGS, sc, dc, and rms do not have to be defined. Abbreviations that incorporate periods should not have spaces: write "C.N.R.S.," not "C. N. R. S." Do not use abbreviations in the title or heads unless they are unavoidable.

B. Units

- Use either SI (MKS) or CGS as primary units (SI units are encouraged).
- Do not mix complete spellings and abbreviations of units: "Wb/m2" or "webers per square meter," not "webers/m2." Spell units when they appear in text: "...a few henries," not "...a few H."
- Use a zero before decimal points: "0.25," not ".25."

C. Equations

The equations are an exception to the prescribed specifications of this template. You will need to determine whether or not your equation should be typed using either the Times New Roman or the Symbol font (please no other font). To create multileveled equations, it may be necessary to treat the equation as a graphic and insert it into the text after your paper is styled.

Number the equations consecutively. Equation numbers, within parentheses, are to position flush right, as in (1), using a right tab stop.

$$\int_0^{r_2} F(r,\phi)\, dr\, d\phi = [\sigma r_2 / (2\mu_0)] \qquad (1)$$

Note that the equation is centered using a center tab stop. Be sure that the symbols in your equation have been defined before or immediately following the

equation. Use "(1)," not "Eq. (1)" or "equation (1)," except at the beginning of a sentence: "Equation (1) is ..."

D. Some Common Mistakes

- The word "data" is plural, not singular.
- The subscript for the permeability of vacuum μ_0, and other common scientific constants, is zero with subscript formatting, not a lowercase letter "o."
- In American English, commas, semi-/colons, periods, question and exclamation marks are located within quotation marks only when a complete thought or name is cited, such as a title or full quotation. When quotation marks are used, instead of a bold or italic typeface, to highlight a word or phrase, punctuation should appear outside of the quotation marks. A parenthetical phrase or statement at the end of a sentence is punctuated outside of the closing parenthesis (like this). (A parenthetical sentence is punctuated within the parentheses.)
- A graph within a graph is an "inset," not an "insert." The word alternatively is preferred to the word "alternately" (unless you really mean something that alternates).
- Do not use the word "essentially" to mean "approximately" or "effectively."
- In your paper title, if the words "that uses" can accurately replace the word using, capitalize the "u"; if not, keep using lower-cased.
- Be aware of the different meanings of the homophones "affect" and "effect," "complement" and "compliment," "discreet" and "discrete," "principal" and "principle."
- Do not confuse "imply" and "infer."
- The prefix "non" is not a word; it should be joined to the word it modifies, usually without a hyphen.
- There is no period after the "et" in the Latin abbreviation "et al."
- The abbreviation "i.e." means "that is," and the abbreviation "e.g." means "for example."

IV. Using the Template

After the text edit has been completed, the paper is ready for the template. Duplicate the template file by using the Save As command, and use the naming convention as below

ULTIMATICS_firstAuthorName_paperTitle.

In this newly created file, highlight all of the contents and import your prepared text file. You are now ready to style your paper. Please take note on the following items.

A. Authors and Affiliations

The template is designed so that author affiliations are not repeated each time for multiple authors of the same affiliation. Please keep your affiliations as succinct as possible (for example, do not differentiate among departments of the same organization).

B. Identify the Headings

Headings, or heads, are organizational devices that guide the reader through your paper. There are two types: component heads and text heads.

Component heads identify the different components of your paper and are not topically subordinate to each other. Examples include ACKNOWLEDGMENTS and REFERENCES, and for these, the correct style to use is "Heading 5."

Text heads organize the topics on a relational, hierarchical basis. For example, the paper title is the primary text head because all subsequent material relates and elaborates on this one topic. If there are two or more sub-topics, the next level head (uppercase Roman numerals) should be used and, conversely, if there are not at least two sub-topics, then no subheads should be introduced. Styles, named "Heading 1," "Heading 2," "Heading 3," and "Heading 4", are prescribed.

C. Figures and Tables

Place figures and tables at the top and bottom of columns. Avoid placing them in the middle of columns. Large figures and tables may span across both columns. Figure captions should be below the figures; table heads should appear above the tables. Insert figures and tables after they are cited in the text. Use the abbreviation "Fig. 1," even at the beginning of a sentence.

TABLE I. TABLE STYLES

Table Head	**Table Column Head**		
	Table column subhead	***Subhead***	***Subhead***
copy	More table copy		

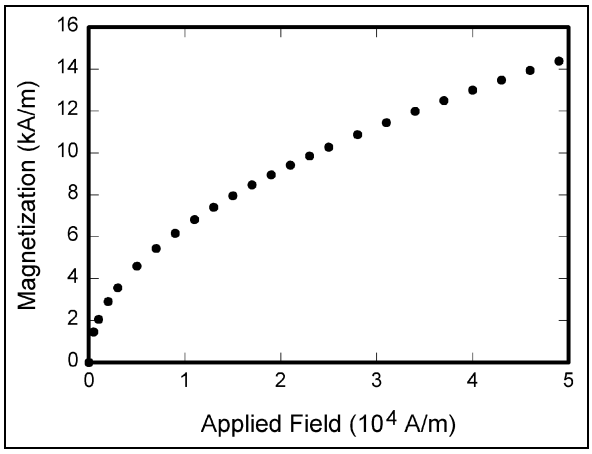

Fig. 1. Example of a figure caption

V. Conclusion

A conclusion section is not required. Although a conclusion may review the main points of the paper, do not replicate the abstract as the conclusion. A conclusion might elaborate on the importance of the work or suggest applications and extensions.

Appendix

Appendixes, if needed, appear before the acknowledgment.

ACKNOWLEDGMENT

The preferred spelling of the word "acknowledgment" in American English is without an "e" after the "g." Use the singular heading even if you have many acknowledgments. Avoid expressions such as "One of us (S.B.A.) would like to thank ... ." Instead, write "F. A. Author thanks ... ." You could also state the sponsor and financial support acknowledgments here.

References

The template will number citations consecutively within brackets [1]. The sentence punctuation follows the bracket [2]. Refer simply to the reference number, as in [3]—do not use "Ref. [3]" or "reference [3]" except at the beginning of a sentence: "Reference [3] was the first ..."

Number footnotes separately in superscripts. Place the actual footnote at the bottom of the column in which it was cited. Do not put footnotes in the reference list. Use letters for table footnotes.

Unless there are six authors or more give all authors' names; do not use "et al.". Papers that have not been published, even if they have been submitted for publication, should be cited as "unpublished" [4]. Papers that have been accepted for publication should be cited as "in press" [5]. Capitalize only the first word in a paper title, except for proper nouns and element symbols.

For papers published in translation journals, please give the English citation first, followed by the original foreign-language citation [6].

[1] G. Eason, B. Noble, and I.N. Sneddon, "On certain integrals of Lipschitz-Hankel type involving products of Bessel functions," Phil. Trans. Roy. Soc. London, vol. A247, pp. 529-551, April 1955. (*references*)

[2] J. Clerk Maxwell, A Treatise on Electricity and Magnetism, 3rd ed., vol. 2. Oxford: Clarendon, 1892, pp.68-73.

[3] I.S. Jacobs and C.P. Bean, "Fine particles, thin films and exchange anisotropy," in Magnetism, vol. III, G.T. Rado and H. Suhl, Eds. New York: Academic, 1963, pp. 271-350.

[4] K. Elissa, "Title of paper if known," unpublished.

[5] R. Nicole, "Title of paper with only first word capitalized," J. Name Stand. Abbrev., in press.

[6] Y. Yorozu, M. Hirano, K. Oka, and Y. Tagawa, "Electron spectroscopy studies on magneto-optical media and plastic substrate interface," IEEE Transl. J. Magn. Japan, vol. 2, pp. 740-741, August 1987 [Digests 9th Annual Conf. Magnetics Japan, p. 301, 1982].

[7] M. Young, The Technical Writer's Handbook. Mill Valley, CA: University Science, 1989.

UMN

UNIVERSITAS
MULTIMEDIA
NUSANTARA

ISSN 2355-3286

Universitas Multimedia Nusantara
Scientia Garden Jl. Boulevard Gading Serpong, Tangerang
Telp. (021) 5422 0808 | Fax. (021) 5422 0800